Collaborative Control of Wave Glider Platforms

Local Communication and Sea State Estimation

Presented by:

Kossivi Agbessi Fangbemi

Under the Supervision of:

Professor Edward Boje
and:
RA Verrinder

Department of Electrical Engineering
University of Cape Town

Submitted to the Department of Electrical Engineering at the University of Cape Town in fulfilment of the academic requirements for a Masters of Science Degree in Electrical Engineering.

October, 2019

Declaration

1. I know that plagiarism is wrong. Plagiarism is to use another's work and pretend that it is one's own.

2. I have used the IEEE convention for citation and referencing. Each contribution to, and quotation in, this report from the work(s) of other people has been attributed, and has been cited and referenced.

3. This report is my own work.

4. I have not allowed, and will not allow, anyone to copy my work with the intention of passing it off as their own work or part thereof.

5. This thesis/dissertation has been submitted to the Turnitin and I confirm that my supervisor has seen my report and any concerns revealed by such have been resolved with my supervisor.

Name: **Kossivi A. Fangbemi**

Signature:

Signed by candidate

Date: **21st October, 2019**.

Acknowledgement

This work is dedicated to my parents and my family. Although I may be far away from your sight, I know I am always in your hearts and in your minds as you are in mine. Your love, blessings and prayers have kept me motivated through difficult times. Thank you for everything.

I owe a debt of gratitude to my supervisor Prof Edward Boje and my co-supervisor Robyn Verrinder for their continuous support and guidance during the course of the research. I discovered a lot under your supervision, and I appreciate profoundly the opportunities you gave me and flexibilities that you allowed.

I want to present my appreciation to my colleagues in the Mechatronics Lab and my friends on campus and at home. You kept me well balanced and rational with your encouragements and "positive" distractions.

Abstract

Climate change is the focus of many oceanography and marine engineering researchers, with possible links between climate change and the carbon cycle in the Southern Ocean being considered. This type of investigation requires modern and cost-effective tools to conduct surveys and collect data from the ocean. The self-propelled unmanned surface vessel, the Liquid Robotics Wave Glider, was designed primarily as a marine research tool and offers several advantages over existing research vessels and other tools employed for data acquisition in the ocean. The main advantages are its robustness at sea, i.e. its ability to withstand extreme weather conditions, its propulsion energy source, which is the wave energy, and its customisable electronics payload.

The inter-platform communication strategy of the Wave Glider inspired a few engineering questions, one of which is the focal point of this research: whether Low Power Wide Area Network (LPWAN) technology can be used to set up a local communication system enabling the collaboration of two or more Wave Gliders and reduce the cost, in terms of power and communication channels, involved in the communication with the Wave Glider platforms during missions.

This research considers various LPWAN technologies available on the market and proposes LoRaWAN technology for the local communication system. LoRaWAN was selected as it presented a robust radio modulation and had growing support in the industry. In this research, a LoRa-based network of two nodes was developed, implemented and tested over the surface of the ocean. It was found that the system performs well over a distance of 1 km with both antennas having one end at the mean surface level of the sea. With the intention to increase the range of the platform and achieve a reliable and robust system, the research continued with the study of the influence of the surface waves on the proposed local communication system by exploring, firstly, the impact of seawater and, secondly, the wave height on signal transmission.

The first study investigated the influence that the electromagnetic properties of seawater may have on the transmission of signals from one node to the second through simulations using the computational electromagnetic package FEKO. It revealed that, at the frequency of operation, which was 868 MHz, seawater reacted as a lossy conductor and reflected the signal upward, with negligible power penetrating the surface of the ocean. The subsequent study reviewed the statistical properties of the ocean surface waves in a sea of deep waters and proposed a relationship between the wind speed (or surface wave elevation), the antenna height, the distance separation between the two nodes and the probability of the presence of a line of sight (LoS) between the two nodes. This relationship quantifies the expected result that

the probability of the LoS diminishes as the wind speed or the distance between the two nodes increases, whereas it improves with an increase in the antenna height.

The last part of the research focused on initial works on sea state estimation using the lossless wave equation and Kalman Filter to provide 3D sea surface elevations that would be used to change to the probability of the LoS calculated previously in the research. Indeed, using the local communication to share the point-wise sea state data can be exploited to estimate the sea state over a rectangular region delimited to include these points. Sea state estimation is expected to enhance the joint navigation and coordination of the platforms and consequently, boost the probability of the LoS through the transmission at the crest of the waves. During the development of the Kalman Filter model, it was discovered that the sample time and the sample space significantly affect the performance and the stability of the discretised models. However, a carefully selected sampling time and sample space exhibited a stable system model. The results of the Kalman filtering were a realistic sea state estimate with a minimum error at the locations in the surrounding of the measurements.

Contents

List of Figures

List of Tables

List of Abbreviations

ALOHA   Additive Links On-line Hawaii Area

BW   Bandwidth

CEM   Computational Electromagnetic

CFL   Courant-Friedrichs Lewy

CR   Code Rate

CSIR   Council for Scientific and Industrial Research

DH   Denavit-Hartenberg

EM   Electromagnetic

FDTD   Finite Difference Time Domain

FEM   Finite Element Method

IoT   Internet of Things

IP   Internet Protocol

JONSWAP   Joint North Sea Wave Project

LE-PO   Element Physical Optics

LoS   Line of Sight

LPWAN   Low Power Wide Area Network

M2M   Machine-to-Machine

MCU   Microcontroller Unit controller

MLFMM   Multilevel Fast Multipole Method

MoM   Method of Moments

NED   North East Down

NLLS   Nonlinear Least Square

pdf   Probability density function

PO   Physical Optics

RAOs   Response Amplitude Operators

RL-GO   Ray Launching Geometrical Optics

RMS   Root Mean-Square

RSSI   Received Signal Strength Indicator

SBD   Short Burst Data

SF   Spreading Factor

SPI   Serial Peripheral Interface

SSE   Sea State Estimation

UTD   Uniform Theory of Diffraction

WAFO   Wave Analysis for Fatigue and Oceanography

Chapter 1

Introduction

1.1 Background to the Research

Understanding climate change and the precise relationship between climate and the carbon cycle in the Southern Ocean have been one of the focuses of oceanographic researchers [17, 18] as well as the CSIR in South Africa [19] over the last few decades. Equally important is marine ecosystem and weather pattern monitoring, which require sophisticated instrumentation. Traditional marine research vessels are costly for the accomplishment of the above mentioned scientific and challenging tasks, and this has compelled marine researchers to migrate towards remote sensing using instrumented buoys. However, this option is lacking when it comes to spatial resolution, i.e. a large number of sensors are required to cover a moderately sized ocean region to get reliable research data.

The Wave Glider platform, shown in Figure 1.1, (Liquid Robotic Inc., the Boeing Company), offers a cost-effective solution for mobile marine observation. The Wave Glider platform is a hybrid, uncrewed marine vehicle consisting of a surface float connected to an underwater glider by an umbilical and flexible tether.
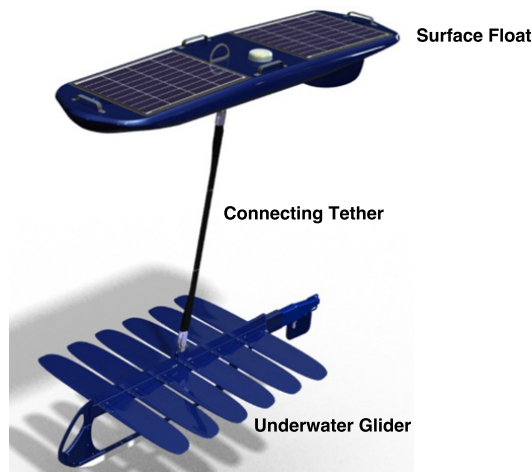
Figure 1.1: Illustration of the SV2 version of the Wave Glider platform showing the surface float and the underwater glider linked by the umbilical tether. Adapted from [1].

The Wave Glider platform provides better energy and operational capabilities as a new tool compared to the traditional human-crewed vessels [20] for investigating and understanding

the marine world. Additionally, this platform has inspired engineering questions concerning remote navigation at sea, wireless communication (technologies and strategies) with the shore, besides the use of the satellite communication, sea state estimation and ocean mapping from the platform. Alternative wireless communication and the sea state estimation are the focus of this research.

1.2 Problem Statement

The Wave Glider platform is used for data collection in the ocean. The data that are collected depends on the aims of the mission and the payloads (sensors) onboard the platform. Two crucial aspects of the platform's operation present an opportunity for further refinement. These are communication with the platform during the mission; the navigation of the platform to the target area where the data must be collected; as well as the coordination of two or more platforms operating in the same area close to each other.

At present, communication with the platform is done via the Iridium Satellite Constellation and the internet for long-range communication and via WiFi and a cellular network for short-range communication [21]. On the one hand, satellite communication is costly per bit transmitted, but its utilisation is often necessary for remote area communications. On the other hand, the WiFi is only used when a base ship is in the proximity of the Wave Glider platform (which does not often happen for a variety of ocean missions); and the cellular communication can only be used when the Wave Glider platform is near the coastline. Furthermore, the current communication protocols of the platform do not allow two Wave Glider platforms to talk directly to each other and collaborate while on the same mission.

Each Wave Glider platform can follow a programmable mission course (or waypoint) and keep the station in the target area individually. However, two or more platforms are inept to navigate collaboratively, i.e. they cannot account for each other's relative position, wave field and heading direction. Having the platforms collaborating would have multiple advantages. It would shorten the duration of the marine mission, thus reduce the cost of the missions and also permit researchers to widen the area of operation for the missions.

All these communication issues, as well as the collaborative navigation (control) of the Wave Glider platform, must be investigated. Using the Wave Glider as a case study, this research will examine these issues, alternative communication technologies and protocols, and make recommendations on ways to mitigate them for the family of human-crewed or uncrewed surface marine vehicles.

1.3 Research Questions

Granted that the end goal of the research is the joint navigation and coordination of two or more platforms, this research examines, in more depth, the engineering and scientific problem

stated above, specifically the issue of communication and the estimation of the sea state. Hence, this research is guided by the following questions:

(1) Is the LPWAN technology, LoRa, suitable for the communication between two collaborative Wave Glider platforms in a marine environment and between these Wave Glider platforms and shore or ship-based control centres?

(2) How would the ocean surface and the platform's motion influence the performance of a LoRa based communication system?

(3) In what way can sea state estimation be exploited to optimise the transmission power, range and data (packets) trade-off in the local communication between and with the collaborative Wave Glider platforms?

1.4 Scope and Limitation

As aforementioned, this dissertation is a part of a larger research research whose principal purpose is to control and navigate multiple collaborative Wave Glider platforms on a mission in the Southern Ocean. This research considers the available wireless communication solutions to establish an intelligent communication system between two collaborative platforms in the aim to contribute toward the overall objective.

The research research focuses on the following:

- Design, implementation and testing of the LoRa wireless communication solution with a focus on the physical layer.

- Evaluation of the performance of LoRa wireless communication in the marine environment and the range of the LoRa transceivers over the seawater through simulations and practical experiences.

- Investigation of the probability of the LoS of the local communication between two platforms on the surface of the sea.

- Propose and evaluate a sea state estimation method based on a Kalman Filter routine that may be used in a later research to improve the local communication though coordinated navigation to the crest of the larger waves.

The availability of the Wave Glider platforms constitutes a significant time and resource limitation of the research in teRMS of integrating and testing the different designs of the research. To indulge this limitation, the practical experiments to be carried out in this research will be done without the Wave Glider platforms. Regarding the local communication, the range will be limited to 10 km or less.

The research makes use of the computing and design resources available in the laboratory. In the case of the sea state estimation that requires computing resources beyond the capacity

of the laboratory, the problem is scaled down to accommodate for this deficiency. As a result, only a proof of concept of the method is demonstrated for the sea state estimation. The method will focus on the sea state estimation looking forward into the future from the next few seconds to a maximum of 60 seconds. Only the sea state estimation method and its results are within the scope of this research, i.e. this research does not deal with the appropriation of the results of sea state estimation for the improvement of the local communication.

1.5 Expected Output

At the completion of this research research, the expected outputs are:

- A designed and tested LoRa wireless communication systems for the two Wave Glide platforms working together with a potential land or ship based master base station. The focus of the design is placed on the physical layer of the communication. The protocol and the message layer are not considered, although the LoRa protocol itself partly achieves them.

- The finding of the investigation into the influence of the ocean surface of the performance and recommendations to minimise this influence, to improve the range and minimise the power requirements of the wireless communication system;

- A proof of concept for a sea state estimation method for the region where two collaborative Wave Glider platforms operate.

1.6 Plan of Development

The rest of the dissertation is structured as follows:

Chapter 2: This chapter describes the background to the research and presents related work.

Chapter 3: It presents the different Low Power Wide Area Network (LPWAN) technologies and the reason for the selection of LoRa technology. The chapter continues with the design, implementation and the testing of the local communication systems.

Chapter 4 deals with the investigation of the influence of the seawater on the local communication through simulations and practical experiments.

In **Chapter 5**, the investigation and evaluation of the probability of the LoS are discussed.

Chapter 6: This chapter elaborates on the sea state estimation method and outlines the results achieved.

Chapter 7 concludes the research and make recommendations for future continuation of the research.

Chapter 2

Background and Related Works

This chapter is subdivided into three main sections. The first section details physical attributes of the Wave Glider platform for readers that are not familiar with the platform. That being the case, the reader who is familiar with the platform can skip this section. The second section introduces sea state estimation and two of the methods that are employed in the literature. The last section completes the chapter with a brief foreword on the methods of modelling the dynamics of the Wave Glider platform.

2.1 Wave Glider Platforms

The Wave Glider platform is a hybrid autonomous marine vehicle. It was conceived by Liquid Robotics Inc. (which is now part of the Boeing Company) for commercial, scientific and military applications. These applications include, but are not limited to, marine environmental monitoring and mapping, weather forecast, communication relay, distance early-warning, marine biology observation and surveying [20]. The platform is made up of two main parts: the surface float and the underwater glider. These two main parts are connected by an umbilical tether as can be seen in Figure 1.1. An elaborate illustration of the platform is provided in Figure 2.1 detailing its dimensions.

Figure 2.1 also highlights the dimensions (length and height) of the different parts of the Wave Glider platform in its current version (SV3). The length, height and width of the surface float are respectively 3.05 m, 0.23 m and 0.81 m. The length, height and width of the submerged glider are 2.13 m, 0.21 m and 1.42 m whereas the umbilical tether shown here to be 8 m long [2] is adjustable. The overall mass of the platform is 150 kg. In the following section, aspects regarding the operation and the power sources; the navigation and the station keeping; as well as the communication and the control of the Wave Glider platform are presented.

2.1.1 Operation and Power Sources of the Wave Glider Platform

The Wave Glider platform is a new type of wave-powered, self-running marine vehicle [3]. This platform presents a meaningful advantage over other ocean powered vessels as it obtains its forward propulsion thrust from the wave energy through a purely mechanical conversion. No electrical energy is required for standard propulsion of the platform, giving the platform
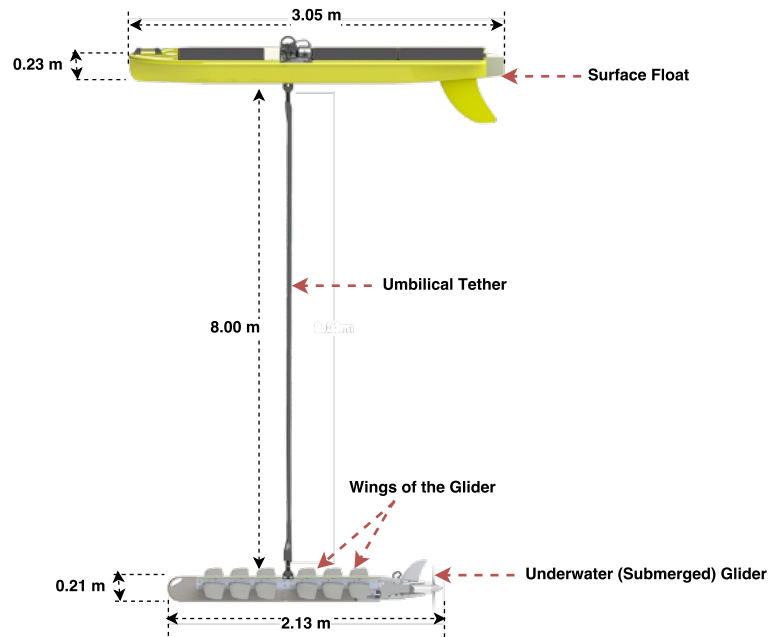
Figure 2.1: The current version (SV3) of the Wave Glider Platform with the dimensions of its different parts. Adapted from [2].

the capacity to have virtually an inexhaustible source of propulsion energy. However, to attain high speed and accurate heading, the glider's thruster uses electrical power when necessary.

The Wave Glider platform converts the mechanical movements of its parts, i.e. the surface float and the submerged glider into its forward propulsion force. This mechanical energy conversion is illustrated in Figure 2.2.

The vertical upwards movements of the surface float, due to the ocean waves, are translated to the submerged glider by the connecting tether. At the depth where the glider is positioned, the water is relatively still, and the wings of the gliders rotate to a specific angular position, allowing them to transform a fraction of the upward movement of the underwater glider into forward propulsion. Similarly, the drop of the underwater glider, due to its weight, is also transformed by its wings into forwarding propulsion. In this case, the wings of the glider are at 90 degrees out of phase compared to their angular position when the glider is moving upwards. In both cases, the underwater glider is propelled forwards, and it drags the surface float along. The direction of the forward displacement of the whole platform is predefined and set by the rudder of the underwater glider. This direction does not depend on the direction of the propagation of the ocean waves, i.e. the wave direction does not affect the direction in which the Wave Glider platform moves in the ocean [22].

The forward propulsion thrust of the platform is generated with a wave just big enough to activate the wings (fins) on the underwater glider. It is independent of the direction of the wave. The speed of the platform depends on the amplitude of the waves, the glider's weight, the buoyancy force of the surface float, the aerodynamic forces, and the wind direction. As a result of these strong correlations, the mass and buoyancy of the Wave Glider platform, as well
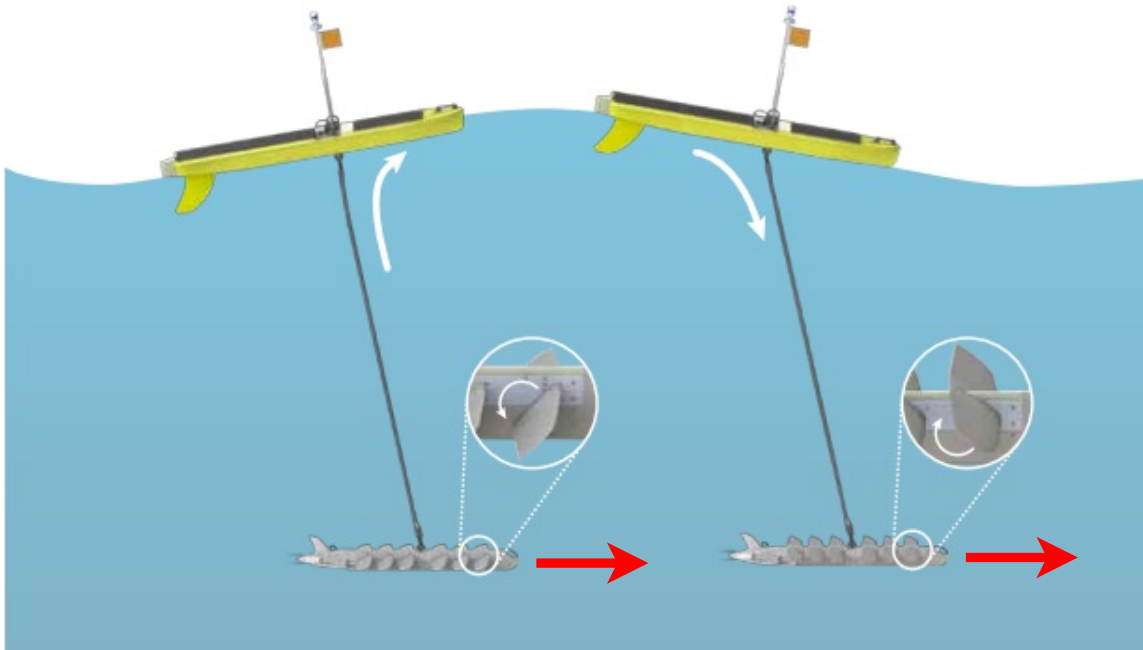
Figure 2.2: Illustration of the purely mechanical conversion of the wave energy into forward propulsion thrust by the Wave Glider platform and the direction of the motion (in Red). Taken from [3].

as the length of the connecting tether, have been optimised to produce a first-rate wave-energy conversion in different categories of sea state. Sea trials have shown the robustness of the Wave Glider and demonstrated the ability of the platform to withstand extreme seas and severe winds [23]. With the considerable power accessible in the ocean, the Wave Glider platform can maintain the course of the predefined waypoints with an average speed of 2.8 km/h. This speed was attained when the platform was tested in a typically calm sea state [24].

Although the forward propulsion of the Wave Glider platform is harvested from wave energy through a mechanical conversion, there are two solar panels and a LiION battery packs onboard serving as the electrical energy source for the platform's payloads. The payloads include the electronics sensor modules, the satellite communication modules and the data storages units. Each of the solar panels is rated at 43 W, but factors such as the mission latitude, the number of the light hours, the angle of incidence of the solar ray, and the cloud coverage in the area, limit the output power of the two solar panels to approximatively 10 W. The LiION batteries packs are rated at 665 Wh [22].

2.1.2 Station Keeping and Navigation of the Wave Glider Platform

The station keeping ability of the Wave Glider platform is utilised for some missions such as using the platform as a communication relay, distant early-warning and weather forecasting. The platform can keep its position in the same area for the duration of the mission at hand (up to a year), usually in a circular holding pattern within the targeted area [24]. The Wave Glider platform achieves station keeping by maintaining the wings of the submerged gliders

Glider's wings at horizontal position
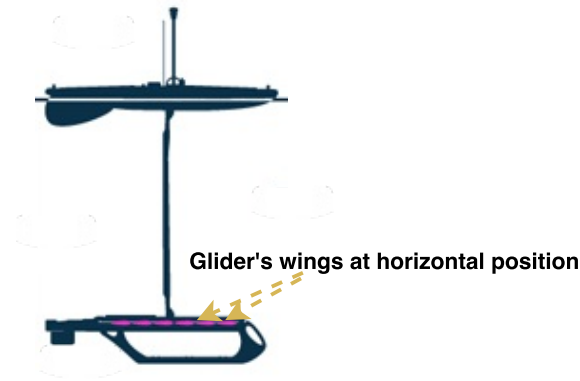
Figure 2.3: Illustration of the wings of the submerged glider (in indigo) at an horizontal position for station keeping. Adapted from [4].

flat (horizontal) provided that there is no strong wind nor a surface current to avert the station keeping. The position of the wings during station keeping is illustrated in Figure 2.3. In this case, where the wings of the submerged glider are maintained horizontal, the vertical movement of the wave and the mass of the Wave Glider platform are not translated into propulsion anymore. The nature of the Ocean induces the rotation of the platform in a circle. The station keeping capability of the Wave Glider platform was evaluated in an experiment in April 2009 by operating the platform as an anchor-less buoy in the surrounding of a conventional science buoy [24]. The Wave Glider kept station within a circle of 50 meters radius whereas the moored buoy as a result of its anchor chain maintained a circle of 1700 meters radius.

For other missions such as surveying, marine environmental monitoring and mapping, the Wave Glider platform is required to move from one area to another, i.e. the platform is required to navigate through the ocean from one area to the next as opposed to keeping station. The limitless propulsion force from the wave energy produces the displacement of the platform from wave energy. However, the waypoints of the mission predetermine the heading angle of the platform and the rudder of the underwater glider sets this heading angle. The Wave Glider platform uses both a 12-channel GPS and a tilt-compensated magnetic compass with a 3-axis accelerometer for its navigation at sea [22]. The 12-channel GPS receiver is the primary navigation sensor of the platform.

Regardless of whether the Wave Glider platform is used in the navigation mode or station-keeping mode, several disturbances are acting on the platform due to the nature of the marine environment. These disturbances could be ocean current, severe winds or other marine vehicles; and cause the Wave Glider platform to deviate from its prearranged heading. The communication, commands and control in place to deal with these disturbance and other factors such as the changes in mission objectives or scope are presented in the following section.
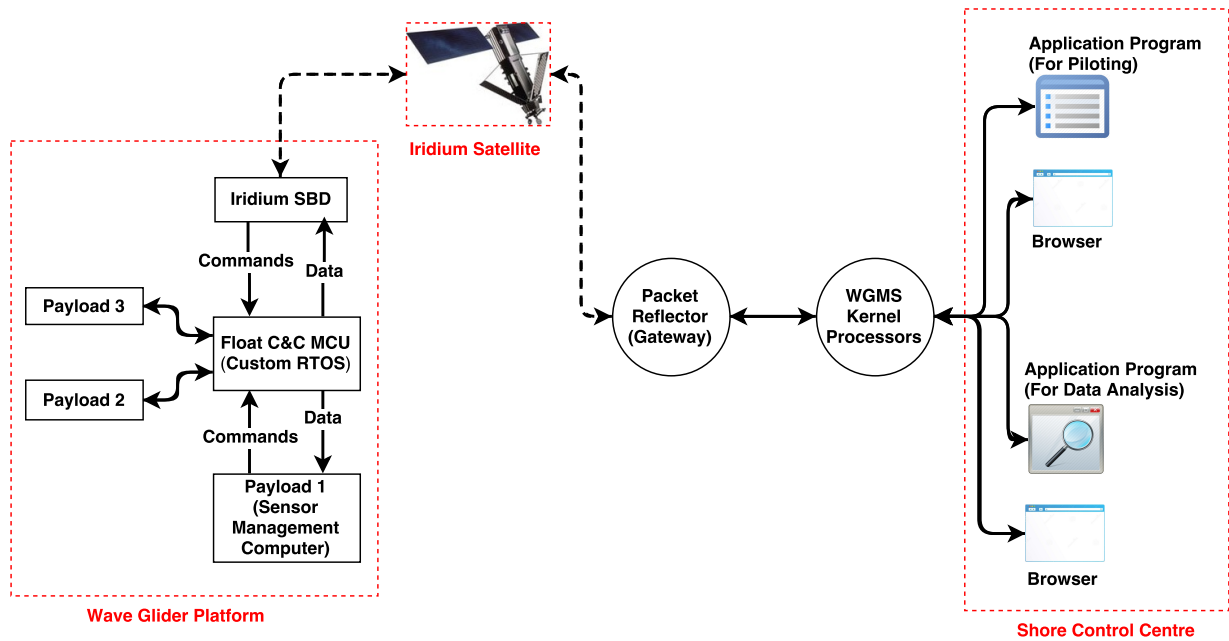
Figure 2.4: Overview of the Iridium Satellite Communication Architecture for the Wave Glider platform. Adapted from [5].

2.1.3 Communication and Control of the Wave Glider Platform

The Wave Glider platform uses a wireless satellite communication link for its long-range communication purposes. The satellite link is the main communication medium and makes use of the Iridium satellite network. An overview of the Iridium satellite communication system of the Wave Glider platform is given in [5]. This generalised Iridium satellite communication architecture presented in [5] is illustrated in Figure 2.4. From this figure, the different subsystems, namely the Wave Glider platform with the Iridium Short Burst Data (SBD), the Iridium satellite and the shore control centre, involved in the overall satellite communication link can be seen. The Shore Control Centre monitors and sends commands to the Wave Glider platform through the satellite link for control and piloting purposes. The satellite link is necessary to keep the platform on the predefined path for a particular mission and to ensure that the platform reaches its target destination since the platform sends its GPS position through to the satellite link. The data collected by the sensors payload on the platform are also sent to the shore control centre, through the satellite link, for analysis.

The heading commands received by the platform is translated, by the Command and Control (C&C) MCU (Master Control Units) on the float, the rudder of the submerged glider which in turn sets the heading angle for the platform. The control systems (hardware and software) implemented by Liquid Robotics Inc. on the Wave Glider platform are proprietary; therefore one cannot comment on its robustness.

Besides satellite communication, the Wave Glider platform has GSM cellular and WiFi communication capabilities [2]. However, the GSM communication is hardly employed except in cases where the platform is in the proximity of the shore for cellular network reception, and the WiFi is utilised for sensor data download exclusively when the offloading vessel is

in the vicinity of the Wave Glider platform. The cellular network is hardly used because the platforms are used in remote sea and the fact that the cellular network is a shore-based system with almost no off-shore footprint. Similarly, the WiFi is not used often there no repeaters to strengthen the WiFi signal for large distances between the two offloading vessel and the platform.

2.2 Sea State Estimation

The performance and efficiency of any marine vehicle, especially wave powered surface marine vehicles, depend on the waves encountered by the vehicle. It is therefore of great importance to know the sea state, i.e. the behaviour of the ocean waves, in the surrounding of the vehicle as this information may affect path planning and the vehicles' resource management. In the case of the Wave Glider platform, the sea state is the main factor affecting the speed of the platform [25, 26]. Knowledge of the sea state surrounding of the platform can be used to set the direction of the platform and as a consequence, have limited control over the speed of the platform. The current research is interested in the estimation of the average behaviour, the spectrum of the local wave field looking half-an-hour into the past and the prediction of the waves in the proximity of the platform for the next sixty (60) seconds. A summary of the techniques proposed in the literature in the context of the sea state estimation is presented.

Sea State Estimation (SSE) is the technique used to evaluate the characteristics of the ocean waves, i.e. the peak period, the amplitude and the phase of the waves surrounding a vessel. Two important approaches attract the interest of marine and oceanographic researchers in the literature. These are the frequency domain approaches and time domain approaches. Each of which is based on the classical wave buoy analogy [27] as illustrated in Figure 2.5.
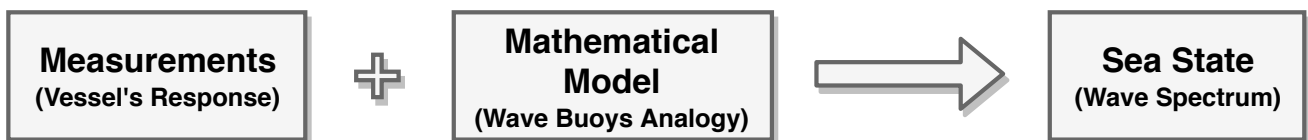
Figure 2.5: Illustration of the classical wave buoy analogy used in the SSE. Adapted from [6].

The classical wave buoy analogy implies that the vessel of interest in sea state estimation can be considered as a floating vessel, simplifying the geometry of the vessel and consequently the mathematical model of the vessel. Furthermore, the wave buoy analogy leads to the assumption that there is a linear relationship between the vessel response (measured) and the amplitude of the regular waves encountered by the vessel; and the irregular waves are given by the summation of the finite number of regular sinusoidal waves with different amplitude, frequency and incident direction [27]. This linearity theory makes it feasible to employ transfer functions and Response Amplitude Operators (RAOs) to formulate the manner in which the incident ocean waves are converted into measured responses [6].
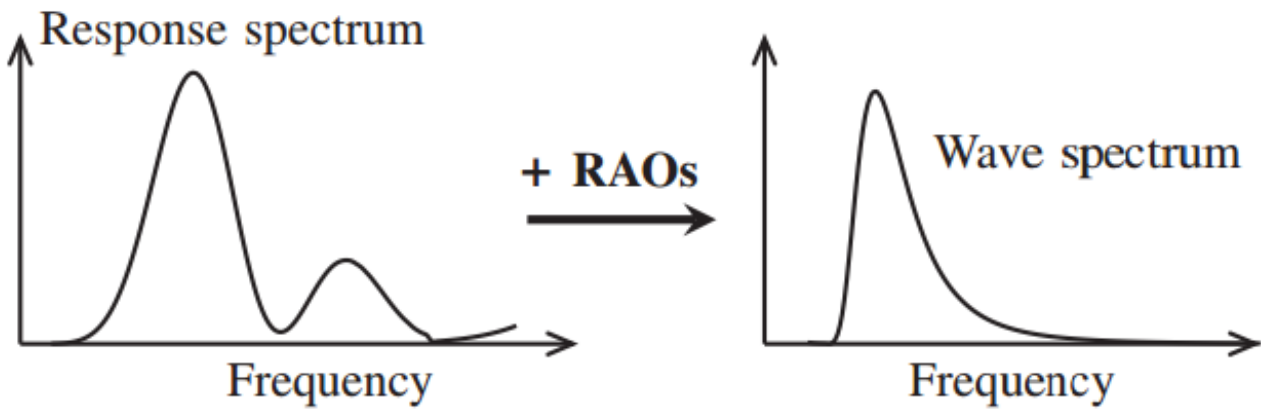
Figure 2.6: Frequency domain approach of the SSE. The plus sign (+) does not represent an addition; here it is used to symbolise the combination of the vessel response spectrum and the RAOs in the method to obtain the wave spectrum. Taken from [6].
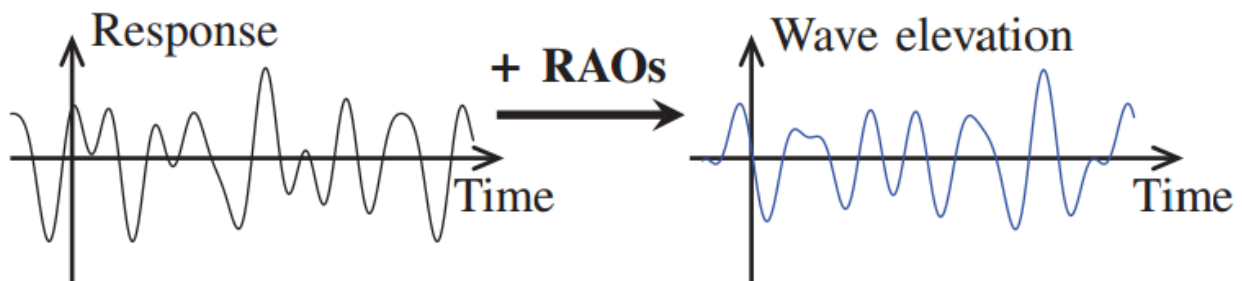
Figure 2.7: Time domain approach of the SSE using the Kalman Filtering concept. This diagram does not describe the technique used; it only gives an overview of the component used in the estimation of the sea state. Taken from [6]

The frequency domain approach combines the spectrum of the measured response of the vessel and the RAOs to provide an estimation of the ocean wave spectrum. An overview of this is illustrated in Figure 2.6. This operation is performed in the frequency domain using two concepts: The first is based on a comparison of the spectral energy distribution of the measured response and the estimated response from the RAOs whereas the second compared the spectral moments of the measured response and estimated response from the RAOs.

Similarly to the frequency domain approach, the time domain approach can use two concepts: Kalman Filtering or a stepwise procedure, to accomplish the Sea State Estimation. A Kalman Filtering approach to sea state estimation was presented in [28]. It is similar to the frequency domain approach as it is fully built on the use of the RAOs to convert the measured response of the vessel into the surface wave elevation (or wave amplitude) as illustrated in Figure 2.7. This technique presents an advantage over the frequency domain approach as its utilisation of the Kalman Filter inherently allows the fusion of measurements from several vessels. The stepwise procedure, on the other hand, is partially built on the RAOs. It employs a frequency estimator in combination with a Nonlinear Least Square (NLLS) fitting to estimate the characteristics of the waves such as the peak frequency and wave amplitude. The stepwise procedure was
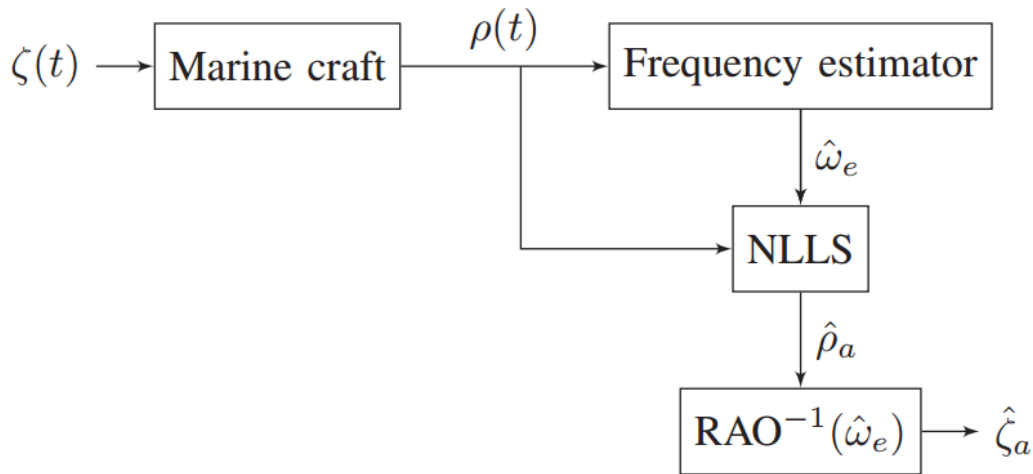
Figure 2.8: Stepwise Procedure concept of the SSE. Taken from [6].

proposed in [6, 29] and it is represented in Figure 2.8.

The frequency estimator takes in the vessel's measured response $\rho(t)$ as its input and works out the characteristic peak frequency $\hat{\omega}_e$ of the wave. The same measured response, $\rho(t)$, together with the estimated frequency, $\hat{\omega}_e$, are the inputs to the NLLS whose output is a fitted value of the response amplitude $\hat{\rho}_\alpha$. Using $\hat{\omega}_e$ with $H^{-1}(\hat{\omega}_e)$, with H^{-1} being the inverse RAOs of the corresponding transfer function, the wave amplitude $\hat{\rho}_\alpha$ and the wave phase $\hat{\epsilon}_\alpha$ can be estimated. In Figure 2.8, $\zeta(t)$ and $\hat{\zeta}_a$ are respectively the real sea state (surface elevations encountered by the vessel) and the sea state estimate.

Both the frequency domain and the time domain approaches have their shortcomings. For instance, they both depend on the RAOs which may not be fully accurate, leading to unrealistic results. Also, an actual vessel response is nonlinear with dependence on the vessel payload, hull fouling, wind load, current, and many other factors. The nonlinearity of the actual response introduces some drawbacks in these methods. Besides the overview of the two Sea State Estimation approaches given here, the reader can find detailed explanation of the two approaches in [6], [27], [28], [30], and [29].

2.3 Dynamic Modelling of the Wave Glider Platform

The dynamic model of a system (platform) is a useful mathematical tool for many applications, notably the control of such a system or the understanding and estimation of the system's behaviour. Many approaches are employed in the literature to model the dynamics of the Wave Glider platform, but the primary methods are the Euler-Newton approach and the Lagrangian approach. Although this research does not deal directly with the modelling of the Wave Glider platform, this section presents these two modelling approaches to set the context for the essential parts for the estimation and control of the platforms.

2.3.1 Dynamic Modelling using Newton's Laws of Motion Approach:

In [31], a two dimensional dynamic model of the Wave Glider platform has been considered for the precise positioning of the Wave Glider platform. This model was estimated in the body reference frame (coordinates system) applying the Newton Laws of Motion together with the following assumptions:

- The umbilical tether connecting the surface float to the underwater glider is always under tension.

- The Wave Glider platform is made up of rigid bodies with constant mass.

- The inputs to the system are stochastic and include the current and wind forces.

- Deepwater Stokes theory applies to the wave motion in the surrounding of the Wave Glider platform.

A simplified discrete-time nonlinear system of differential equations is obtained to describe the dynamics of the Wave Glider platform in [31] based on these assumptions.

In [15], the same author described a full nonlinear dynamic model of the Wave Glider platform. Similarly to the author's first works, Newton's Laws of Motion are employed, but in the North East Down (NED) reference frame. The position and the velocity parameters used by the author are summarised in Table 2.1.

Table 2.1: Position and velocity parameters used in [15]

Designation	Position η	Velocity ν
Surge	x	u
Sway	y	v
Heave	z	w
Roll	ϕ	p
Pitch	θ	q
Yaw	ψ	r

The dynamic model is given as:

$$M\dot{\nu} + C(\nu)\nu + D(\nu)\nu + g(\eta) = \tau, \tag{2.1}$$

where:

M is the inertia matrix of the Wave Glider platform;

$C(v)$ is the matrix of the Coriolis and centripetal terms;

$D(\nu)$ is the damping matrix;

$g(\eta)$ is the vector of the gravitational forces and moments;

τ is the vector of the applied generalised forces;

η is the position vector given by $\eta = [x, y, z, \phi, \theta, \psi]^T$ and;

ν is the velocity vector given by $\nu = [u, v, w, p, q, r]^T = \dot{\eta}$.

2.3.2 Dynamic Modelling using the Lagrangian Approach:

Besides the modelling approach built on the application of Newton's Laws of Motion, other authors use the Lagrangian approach to model the dynamics of the Wave Glider platform. That is the case in [7] where the author considers the Lagrangian approach in combination with the Denavit-Hartenberg (DH) parameters to model an hybrid platform of a similar structure to the Wave Glider Platform. The base reference b for the DH parameters is the NED reference frame. The author proposed seven reference frames with four variables in each frame. The transformation from reference frame i to the reference frame $i - 1$ ($i = 1, 2$), is performed using the transformation matrix:

$$T_i^{i-1}(d, \theta, a, \alpha) = \begin{bmatrix} \cos(\theta) & -\cos(\alpha)\sin(\theta) & \sin(\alpha)\sin(\theta) & a\cos(\theta) \\ \sin(\theta) & \cos(\alpha)\cos(\theta) & -\sin(\alpha)\cos(\theta) & a\sin(\theta) \\ 0 & \sin(\theta) & \cos(\theta) & d \\ 0 & 0 & 0 & 1 \end{bmatrix}, \quad (2.2)$$

where the DH parameters d, θ, a and α are obtained as:

- d: the distance from z_{i-1} to the z_i;

- θ: the angle about z_{i-1}, from x_{i-1} to the x_i;

- a: the length of the common normal between the two frames $i - 1$ and i;

- α angle about the common normal, from z_{i-1} to the z_i.

The reference frame that the authors of [7] used is given in Figure 2.9

The Lagrangian approach to dynamic modelling applies (2.3) to the system

$$\frac{d}{dt}\left(\frac{\partial L}{\partial \dot{q}}\right) - \left(\frac{\partial L}{\partial q}\right) + \left(\frac{\partial F_d}{\partial \dot{q}}\right) = \tau, \quad (2.3)$$

where L is the Lagrangian function given by the functional difference between the total kinetic energy T of the system and the total potential energy U of the system, i.e. $L = T - U$; F_d is the Rayleigh-like dissipation function that characterises the viscous attributes of the Wave Glider platform's joints; q is the configuration vector and τ is the generalised force vector applied to the Wave Glider platform.

An extended version of the Lagrangian method was developed and used to model the Wave Glider platform in [32] fully. This method also used the DH parametrisation in the NED inertial frame. This method used the nautical modelling of a single body to represent the equations of motion in terms of the mass, Coriolis, centripetal and restorative force matrices. This lead to a model in the following format:

$$M_{RB}(q)\ddot{q} + C_{RB}(q, \dot{q})\dot{q} + G(q) = \tau_{RB}, \quad (2.4)$$
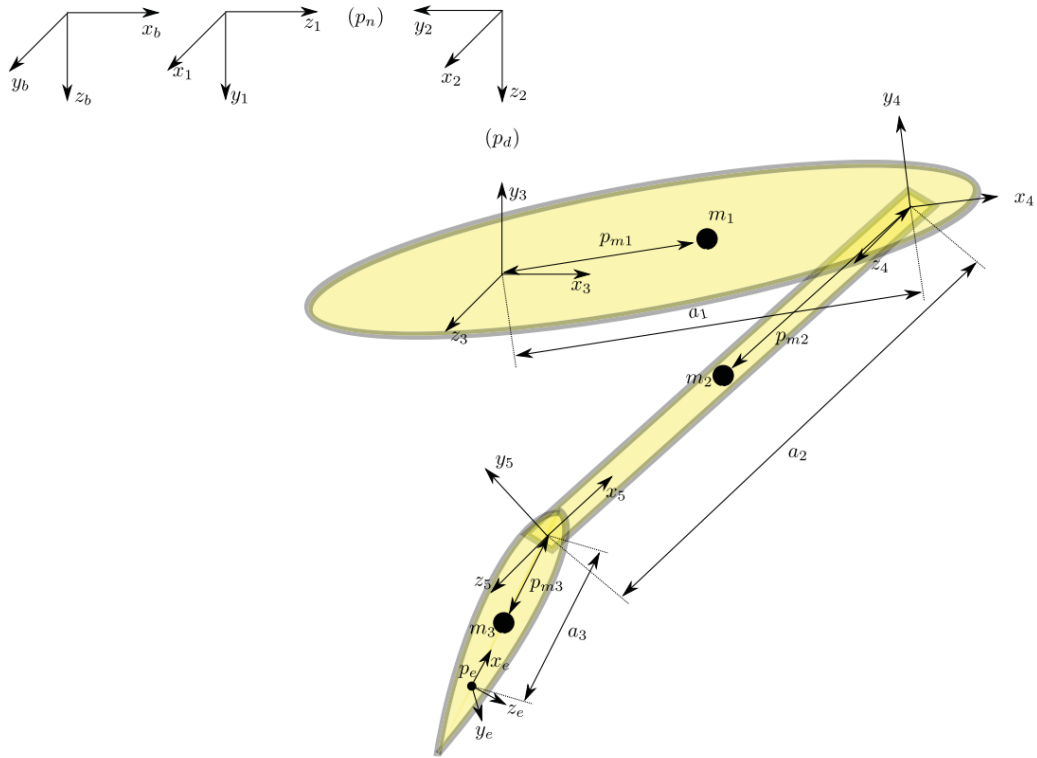
Figure 2.9: Reference frame utilised in the modelling of the Underwater Wave Glider. Taken from [7].

where $M_{RB}(q)$ is the mass matrix , $C_{RB}(q, \dot{q})$ is the Coriolis and centripetal force matrix, $G(q)$ represents the restorative force matrices, τ_{RB} is the is the external forces and moments on the system, $\tau_{RB} \in \mathbb{R}^m$, and q is the generalised coordinate vector of dimension m. The buoyancy, the hydrodynamic forces and added mass, the hydrofoil and the rudder modelling of the Wave Glider platform were then examined and used to complete the dynamic modelling of the Wave Glider Platform. The model obtained has 12 degrees of freedom.

2.4 Conclusion

This chapter has given an overview of the Wave Glider platform, and the methods used in the literature to obtain its dynamic model even though the modelling methods introduced are not the main focus of this research. Also, the approaches available in the literature regarding the sea state estimation were also explored in this chapter. Their description showed that the sea state estimation could be achieved either in the frequency domain or the time domain though a rigorous mathematical treatment has been excluded here. These methods assume that the surface elevation is linear to simplify the computations. The overview of the Wave Glider platform showed its capacities and some of its shortcoming; thus it established the background to the research in this dissertation. One of these limitations is the communication systems on the platforms.

In the next chapter, the cost of the Iridium satellite communication will be presented and compared to the low power technology proposed for the local communication system. Also,

the next chapter will outline the design of the local communication system.

Chapter 3

Design and Implementation of the LoRa-based Communication Network

The Wave Glider platforms use the Iridium Satellite Network for the majority of their communications. The costs of the commercial Iridium Satellite communication for the Short Burst Data (SBD) service option are summarised in Table 3.1.

Table 3.1: Cost Packages of the Commercial Iridium Satellite Communication for the Basic Short Burst Data are presented.

Service Option	Cost	Data length	Taken from
	US $1-1.5 /kbyte + US $20 monthly	$\leq 340\ Bytes$	[33]
Basic Short Burst	US $1.15 /kbyte + US $27 monthly	$\leq 340\ Bytes$	[34]
Data (SBD) Plan	US $1.09 /kbyte + US $15.99 monthly	$\leq 340\ Bytes$	[35]
	US $1-1.5 /kbyte + US $20 monthly	$\leq 340\ Bytes$	[36]

Table 3.1 exemplifies the high cost of the Iridium Satellite communication schemes overall. Iridium Satellite communications may not only require a monthly activation fee [36] but also requires a subsequent time-on-air cost. Thus, it can be intuitively deduced that the usage of the Iridium satellite communication on the Wave Glider platform yields a significant cost on the operational cost of the platform during missions. Also, the satellite communication could stretch out the limited electrical power (under harsh weather conditions) on the platforms. The power consumption of the Basic Short Burst Data plan cannot be explicitly found from the sources of information in Table 3.1; but looking at the data-sheet of one of Iridium SBD transceiver in [37] provided an insight. Its operation supply voltage being 12 V, the transceiver consumes 0.13 A on average per transmission. This yields a power consumption of 1.56 W during transmission. This power value would be a colossal consumption and weighs heavily on the electrical power utilisation on the Wave Glider platform if the time-on-air is considerably sizeable as in the case of near-real-time applications. The Wave Glider platform only has approximatively 10 W of power supplied by the two solar panels. This power requirement of the Iridium communication can be considered as a limiting factor for the efficient performance of the platform. These two impediments on the existing satellite communications call for the

considerations of possible substitute systems to reduce the cost of the satellite communication. These substitute systems must take into account the environmental obstacles presented at sea, where the Wave Glider platforms operate.

This dissertation proposes a LoRa-based communication system as an alternative communication system for the different applications of the Wave Glider platforms. This alternative communication system would enable local collaboration between two or more Wave Glider platforms when the distance separating them is around 10 kilometers or less. It will also facilitate the communication between a host ship and any Wave Glider platform within its surrounding region. The motivations for the selections of the LoRa technology are provided in this chapter as well as the design steps, the implementation and testing.

3.1 Low Power Wireless Communication and LoRa Technology

Cellular Networks, Broadcast radio, Satellite and Bluetooth and WiFi, are a few examples of traditional wireless communication. Applications of these wireless communication systems require high power for the transmission of information, especially in cases where the information has to travel a long distance. However, with the emergence of the Internet of Things (IoT) and the Machine-to-Machine (M2M) communication which requires low power but only provide low data rates, it became absolutely essential to transmit at low power and cover an extensive range at the same time because of the high power cost of traditional wireless communication for such applications. The Low Power Wide Area Networks (LPWAN) solutions emerged to bridge this gap [38].

After a review of the different applications of wireless communication technologies, this research focuses on the LPWAN. The next sections look closer at these technologies.

3.1.1 Low Power Wireless Communication Technologies and their Characteristics

The Low Power Wide Area Networks (LPWAN) are wireless communication networks with the potential to send information a long distance at a minimal energy per bit of information. These technologies use low-bandwidth connectivity with a low data transfer rate to achieve the long-range transmissions. The LPWAN are the first choice for IoT and M2M applications considering that LPWAN provide efficient and moderate power cost to the large number of connected devices that such applications expect [39]. Other wireless communication technologies with high data rate such as WiFi and 2G cellular networks [40] are not designed for signalling and traffic control of a large number of connected nodes because the limited number of channels they can handle simultaneously. Besides, the robust modulations, for instance, the Chirp Spread Spectrum (CSS) and the Ultra Narrow Band, applied by the LPWAN technologies, make them appropriate to connect devices in harsh environments [9], underground and at

sea; for example, as the signal can penetrate some obstacles in their path at low frequencies. However, there a trade-in between the robustness of the LPWAN and their data rate.

There are a few LPWAN technologies available for deployment in the market. The main ones are LoRaWAN™, Sigfox™, Weightless™, Ingenu™. Just like any other technology, each of these LPWAN has its pros and cons, i.e. one technology may work better for some application than others [41]. The technical characteristics of the mentioned LPWAN technologies are summarised in Table 3.2, where the model stands primarily for the support behind each technology.

Table 3.2: Overview of the characteristic of the main LPWAN technologies [16].

LPWAN	Model	Frequency	Range	Data Rate	Packet Size
LoRaWAN™	Alliance	433 / 868 / 780 / 915 MHz	Rural: 15 km Urban: 2-5 km	Uplink and downlink: 300 bps-50 kbps	User-defined
Sigfox™	Proprietary	868 / 902 MHz	Rural: 30-50 km Urban: 3-10 km	Uplink: <300 bps downlink: 8 bps per day	12 bits
Ingenu™	Proprietary	2.4 GHz	Rural: 5-10 km Urban: 1-3 km	Uplink: 624 kbps downlink: 156 kbps	0.006-10 Kbits
Weightless-W™	Alliance	400-800 MHz	5 km	Uplink and downlink: 1 kbps-10 Mbps	>10 bits
Weightless-N™	Alliance	<1 GHz	3 km	Uplink and downlink: 100 bps	<20 bits
Weightless-P™	Alliance	<1 GHz	2 km	Uplink and downlink: 0.1-200 kbps	>10 bits
Dash7™	Alliance	433 / 868 / 915 MHz	<5 km	Uplink and downlink: 10, 56, 167 kbps	<256 bits

The data rate varies a lot from one technology to another. LoRaWAN™, Sigfox™, Ingenu™ and Weightless-W™ are the technologies capable of covering a range of at least 5 kilometers, the first three coving more in non-urban areas. LoRaWAN™ and Sigfox™ are preferred for their ranges in rural areas.

For Sigfox™, the base stations are the property of Sigfox™, and the network users can connect their devices to a base station only if there is one deployed in the area. Thus, Sigfox™ is only exploited in urban areas. However, the LoRaWAN™ technologies can be used anywhere since the network user can build their own base station. Besides, a look at the literature has shown more academic support to applications using LoRaWAN™ technology like the ones in [42, 43, 44]. Also, the fact that LoRa based electronic systems (boards) are readily available and easily accessible made LoRaWAN™ the preferred LPWAN technology for this research. An overview of LoRaWAN™ is given in the next section.

3.1.2 Overview of the LoRaWAN™ Technology

LoRaWAN™ is an open-standard LPWAN technology designed by SemTech™ [45] and supported by the LoRa Alliance. LoRaWAN™ has gained momentum in the past few years because
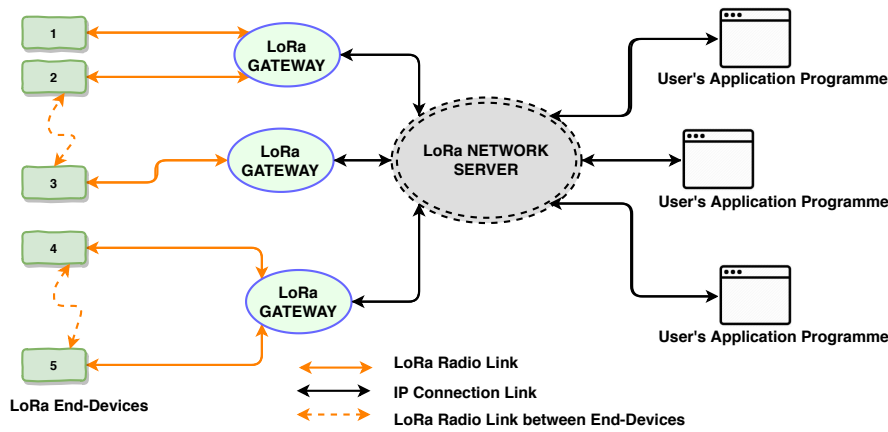
Figure 3.1: Overview of the architecture of the LoRaWAN technology. Adapted from [8].
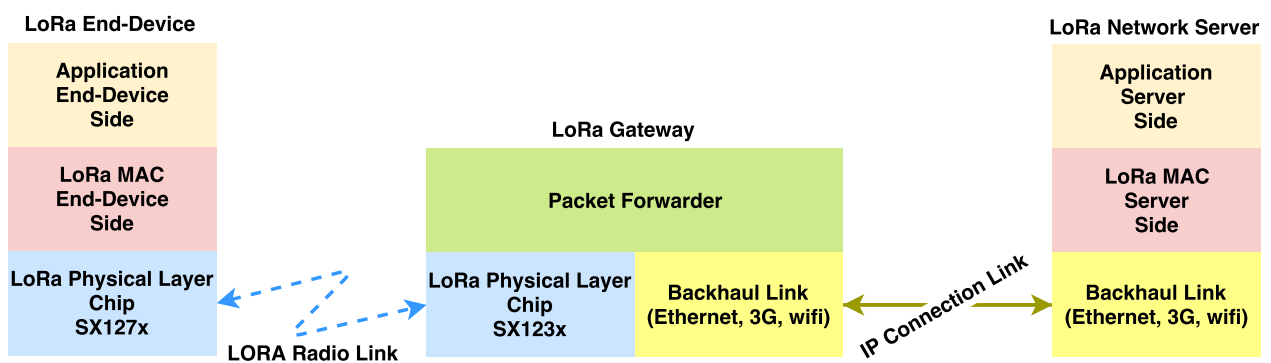
Figure 3.2: Overview of the ALOHA protocol used in the LoRaWAN technology. Adapted from [9].

of the LoRa Alliance Members and academic research focusing on the technology. LoRaWAN™ uses a LoRa microchip in its physical layer. The basic architecture of the LoRaWAN™ network, which uses a star network topology, is illustrated in Figure 3.1.

The end-devices enabled with a LoRa transceiver are connected to one or more LoRa Gateways (LoRa Concentrator) via a LoRa radio Link. In turn, all the LoRa Gateways are connected to the LoRa Network Server via an Internet Protocol (IP) connection Link. The LoRa Network Server controls the whole network, i.e. the radio resource management, the admission and traffic control, the security, and others. The IP Connection Link in the architecture is based on standard Internet communication technologies like cellular, WiFi and Ethernet.

LoRaWAN™ uses an Additive Links On-line Hawaii Area (ALOHA) network protocol [9] which is shown in Figure 3.2. This network protocol allows the use of minimum power consumption of the end-nodes in a LoRaWAN™ network, to ensure that LoRaWAN™ is a low power wireless communication technology. The minimum power consumption is achieved through the categorisation and the use of the three classes of the end-nodes.

The three classes of the LoRa end-nodes are the Class A, B and C:

- The end-nodes of Class A make the LoRaWAN network asynchronous with more priority given to uplink. The end-node opens two downlink receive windows after a transmission.

The second receive window is only open if nothing is received in the first window. This class is the default functional mode of all LoRa end-nodes and is recommended for monitoring applications.

- Class B end-nodes expand the features of Class A by their capacity to open more downlink receive windows at scheduled times. The Class B end-nodes open additional downlink receive windows only at times dictated by a synchronised beacon sent by the LoRa Gateways. This synchronised beacon also tells the LoRa Network Server about the times the end-nodes are listening. Class B end-nodes are recommended for applications where the LoRa Network Server need to send commands to the end-nodes.

- Class C end-nodes, as opposed to the first two classes, have their downlink receive window opened continuously, except when the end-nodes are transmitting.

The Class A end-nodes consume the least power whereas the Class C end-nodes use the most power. An end-node can be of Class A and Class B or Class A and C simultaneously, but it cannot function as a Class B and Class C concurrently. The LoRa nodes use a maximum transmission duty cycle of 1% to allow the Gateways to handle a large number of end-devices and minimise power usage. For the research, we anticipate the use of only a few end-devices in a point-to-point communication system. In the rest of the document, the word LoRa will be used to refer to the physical Layer of LoRaWAN™.

3.1.3 The Physical Layer of the LoRaWAN™

LoRaWAN™ technology exerts a modified version of the CSS radio modulation to attain its low cost, low power performance over long distance. The CSS is a modulation method that uses a wideband linear frequency chirp signal, i.e. a sinusoidal signal whose frequency varies over time, to encode information. The low cost, low power performance is accomplished by a chirp signal shifting in frequency perpetually, while synchronising timing and frequency offsets between transmitter and receiver. As a result, the receiver design is substantially simplified. Each message byte is also packaged with address and other fields as shown in Fig 3.3.

The Symbol Rate (R_s) of a LoRa radio Channel depends on two parameters: The bandwidth (BW) of the channel and the spreading factor. The number of bits-encoded per symbol, N_b, is related to the spreading factor through the relationship given by:

$$N_b = 2^{SF} \qquad \text{bit/Symbol.} \tag{3.1}$$

The relationship between these parameters of the physical layer is:

$$R_s = \frac{BW}{2^{SF}} \qquad \text{Symbols/sec.} \tag{3.2}$$

Where the BW values are 125, 250, or 500 kHz and the spreading factors are 7, 8, 9, 10, 11 or 12. Any two spreading factors give two orthogonal symbol codes; therefore, the value of the
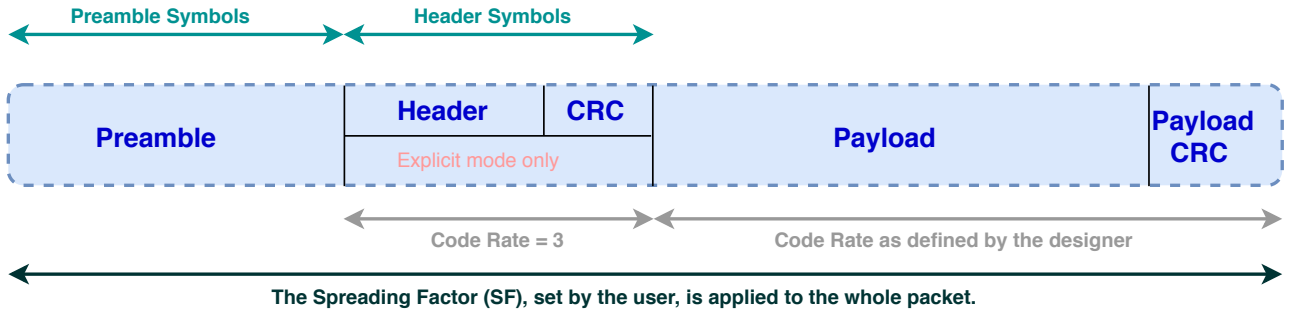
Figure 3.3: Structure of a LoRa Packet taken from the data-sheet of LoRa transceiver SX1276. Adapted from [10].

spreading factor has to be identical at both the transmitter and receiver sides. The time-on-air (T_s) of the symbols transmitted is the inverse of the symbol rate, i.e.:

$$T_s = \frac{1}{R_s} = \frac{2^{SF}}{BW} \qquad \text{sec/Symbols.} \tag{3.3}$$

It is tangible from the above expressions that, for a fixed bandwidth, the higher the spreading factor the higher the time-on-air of the transmitted information (signal) and vice versa. The modulated bit rate (R_b) of the channel is a function of the Symbol Rate (R_s) and the spreading factor and is given by:

$$R_b = SF \times R_s \qquad \text{bit/s,}$$

$$R_b = SF \times \frac{1}{\left[\frac{2^{SF}}{BW}\right]} \qquad \text{bit/s.} \tag{3.4}$$

The robustness of LoRa CSS modulation is engineered using a non-uniform forward error detection and correction method that has an advantage of redundancy of the information being transmitted [10]. Accordingly, the modulated bit rate becomes:

$$R_b = SF \times \frac{\left[\frac{4}{4+CR}\right]}{\left[\frac{2^{SF}}{BW}\right]} \qquad \text{bit/s,} \tag{3.5}$$

where CR which stands for the Code Rate, represents the scale of the forward error detection and correction. This Code Rate (CR) is an integer varying from 1 to 4.

The structure of the physical packet conveyed over a LoRa channel is illustrated in Figure 3.3. The packet encompass three segments:

1. *The Preamble* contains all the information necessary to synchronise the receiving end to the succeeding data flow. Its length varies from 6+4 to 65535+4 symbols, while the default length is 12 symbols;

2. *The Header*, when used in its explicit mode, contains details of the payload such as the value of the forward error detection and correction CR, the length of the payload in bytes as well as the presence of an optional 16-bit CRC for the payload; and

3. *The Data Payload*.

Figure 3.3 showed that forward error detection and correction (with different CR), are only applied to the Header and the payload sections of the packet. The CR is fixed at 3 for the header whereas the one for the payload is user-defined and could be any integer between 1 and 4. Meanwhile, the spreading factor is applied to every symbol in the packet.

While the maximum transmission power of a commercial LoRa transmitter is 20 dBm, the range of the transmission would depend on the power gains of the two antennas and the receiver sensitivity. In other words, the lowest power beyond which the receiver cannot detect the transmitted signal and therefore cannot retrieve the information being conveyed, when considering the Friis transmission formula stating that [46]:

$$\frac{P_R}{P_T} = G_T G_R \frac{\lambda}{2\pi d},$$
(3.6)

where P_T and P_R are respectively the transmission power and the received power; G_T and G_R are the power gain of the transmitter and receiver respectively; λ is the wavelength in free space; and d is the distance between the two antennas.

For LoRaWAN™, the sensitivity of the receiver is defined by the particular LoRa transceiver and goes as low as - 148 dBm for the SX1276 transceiver, for instance.

3.1.4 Hardware Architecture of the LoRa end-Devices

The end-device comprises two main elements: The radio (RF transceiver) and Microcontroller Unit controller (MCU) that executes the radio drivers, the sensors drivers and the LoRaWAN™ stack (MAC layer and the application layer). Two main categories of the end-devices emerge, and they are conditional on the hardware and its connections. They are [47]:

- **The Single MCU end-device**: One MCU is employed in this case to run the all the necessary software and drivers. This MCU is connected to the radio via a Serial Peripheral Interface (SPI) and manages the radio, i.e. reset the radio, read interrupts from the radio and set the antenna to transmission mode or reception mode. The MCU is the master, and the radio is the slave for the SPI.

- **The Split end-device**: This variety of end-devices is split into two components: A LoRa modem and a host controller; as a result, two MCU's are utilised. The main MCU, that is to say, the host controller executes the Application layer while the LoRa modem implements the radio drivers and the MAC layer. The host controller communicates and controls the LoRa modem, often, over a UART interface.

The advancements accomplished by the LoRa Alliance members make it feasible and afford-able to get two end nodes to converse with each other. This research exploits these features to design LoRa based communication system that may be used for point to point communication between marine surface vehicles. The next part of this chapter describes a few researchs where LoRa radio technology has featured, and continues to the description of the proposed system design.

3.1.5 LoRaWAN™ Compared to the Iridium Satellite Communication

Table 3.3 compare the LoRaWAN™ to the Iridium satellite communication in terms of the start-off and the time-on-air cost. This comparison does not include the procurement of transceivers as the Iridium is built into the Wave Glider platforms.

Table 3.3: Comparison between LoRaWAN™ and the Iridium satellite communication system. The basic SBD service option is used in this comparison for the Iridium communication. The values for the Iridium Communication are the average of the ones given in Table 3.1. The power column refers to the power consumption during the transmission of data.

Technology	Start-off Cost	Cost per kbyte of information	Power	Latency
Iridium Satellite	US $20.75 monthly	US $1.185	1.56 W	5 to 20 sec [48]
LoRaWAN™	None	None	0.396 W	up to 128 sec [49]

Assuming that time-on-air for both transceivers (Iridium and LoRa) are similar per kbyte of information, the energy per kbyte of information consumed on Iridium is higher. Looking at the cost, once the LoRa system is installed, there is no service cost for a point-to-point communication as opposed to the Iridium communication. Table 3.3 also showed the latencies of both technologies, which accounts for the time elapsed between the request of data from an end-device to the moment that data becomes available. The latency of LoRaWAN in Table 3.3 was evaluated as the time elapsed from the information leaving the end-device to the moment the information is available for viewing in the user's application programme. This latency is significantly reduced to the order of a few milliseconds for point-to-point communication.

The above comparison confirms the usefulness of a local communication system and supports the selection of the physical layer (radio) of the LoRaWAN™. After the related work in the next section, the remainder of the chapter will focus on the design, the implementation and the testing of the LoRa based local communication system.

3.2 Related Work

This research research focuses on the possible collaboration of the two or more Wave Glider platforms by considering a local communication scheme and the control of the platforms. The literature shows a shortage of studies closely related to the objectives of this research. Nevertheless, a few studies are worth mentioning.

The first one is presented in [5], where the author profiles the components of the core electronics on the Wave Glider platform, the typical mission types that the Wave Glider platform is built for as well as the performance requirements that led to the choice and conceptualisation of the Iridium satellite communication architecture for the platform. The author discusses the

Iridium satellite communication architecture through a stepwise clarification. It establishes the performance requirements of the satellite communication scheme used on the Wave Glider platforms and these requirements can be considered as the starting point for the design of the LPWAN based communication scheme for the platforms in this research.

The second study worth mentioning is presented in [50]. The authors of this publication give an overview of the capabilities and limitation of the LoRaWAN technology. At first, the authors describe the LoRaWAN technology and highlight its successes over its counterpart LPWAN technologies (Ingenu, Weightless, Sigfox) and the cellular technologies in the context of their applications for the IoT. Furthermore, the authors enlighten the reader on the limitations of the LoRaWAN. Notably, the authors insist that the duty-cycle limits the network size of the LoRaWAN and the network capacity is limited by its reliability and its densification.

The last work presented in [51] is about the control of the Wave Glider platform. The authors of this paper propose an embedded control system for the application of the Wave Glider platform. The authors suggested a neuropsychological structure model for the Wave Glider platform. This model was then used to design a self-adapting PID controller and an improved S-surface controller for the reference path following and the heading angle control respectively. Although this research is focusing on the dynamic model of the Wave Glider platforms, the two controller types advocated are worth considering for this research.

3.3 Initial LoRa System Design and Implementation

The initial design aimed to develop a vital understanding of the LoRa protocol while investigating a few crucial questions in the context of this research.

3.3.1 Hardware of the LoRa System

The initial design is based on the split end-device hardware architecture. The system has two nodes connected through a LoRa radio link. The RF1276-868 LoRa module, developed by Appcon Wireless technology limited, was procured as the LoRa modem at the nodes [52]. This module is based on the LoRa transceiver SX1276 from SEMTECH™ and was selected as it was assessed to reduce the discovery and development time in this research. Each node was built from the LoRa modem (RF1276-868), a host controller (PC for development and Arduino Mini board for field testing) and a dipole antenna. Figure 3.4 shows a block diagram illustrating the connection at the system nodes. The controller is connected to the RF1276-868 LoRa module using a UART (serial) link, and the LoRa module is connected to the antenna via a coaxial cable that has an impedance equal to 50 Ω matching the antenna. The main characteristics of the RF1276-868 LoRa module are tabulated in Figure 3.5a. An image of this LoRa module is given in Figure 3.5b.

The application layer for the end-devices was developed in the Arduino programming language for the Arduino Mini as the host controller and in Python 2.7 when a Personal Computer (PC) was used as the host controller for the split end-device architecture. Python 2.7

(a) Host Controller is an Arduino Mini Board   (b) Host Controller is a computer
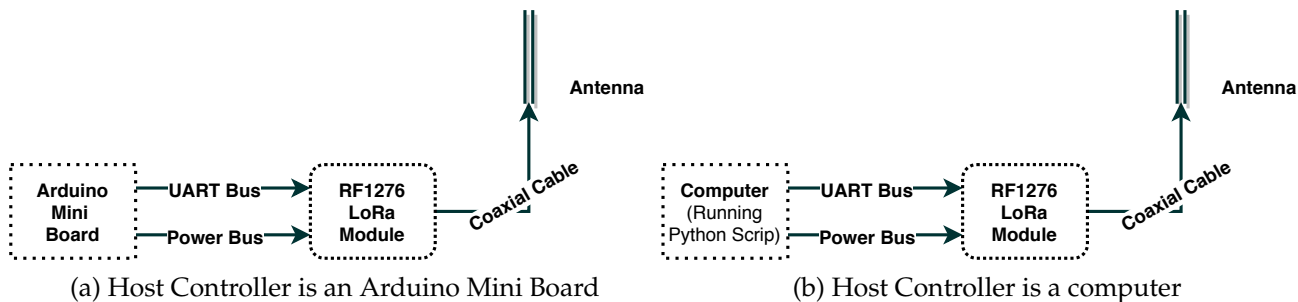
Figure 3.4: Split end-devices used for the LoRa communication system. The power supply for the Arduino mini board is not shown in the block diagram.

Characteristic	Values
Frequency	869.5 MHz
Maximum Transmission Power	20 dBm
Number of Transmission Power levels	7
Minimum Transmission Power	4 dBm
On Air Transmission	3.75 - 136.75 Bps
Air Data Rate	300 - 11000 bps
UART Data Rate	1200 - 115200 bps
Supply Voltage Level	5 Volt DC

(a) radio Characteristics of the RF1276-868 LoRa Module from Appcon Wireless technology limited. This is obtained from the data-sheet of the module. Found in [52].

(b) Image of the the RF1276-868 LoRa Module from Appcon Wireless technology limited [53].

Figure 3.5: Characteristics of the RF1276-868 LoRa Module.

was used for this task as it presented an efficient, systematic and potent routine to interface with the LoRa module using the serial communication resources available on the personal computer.

The antenna was selected with consideration to the main objective of the dissertation, namely, the desire to attain a range of up to 10 km of LoS communication using the LoRa radio technology. The desired maximum range is set to 10 km because the range of LoRa is reported to be around this value in optimal conditions. As a result, an omni-directional dipole antenna, OA-868-01, with operating frequencies ranging from 800 MHz to 900 MHz was procured from Otto Wireless Solutions. This antenna is linear and vertically polarised with a gain of 6 dBi and an impedance of 50 Ohm.

3.3.2 The Main Parameters of the LoRa Network

The LoRaWAN™ technology protocol is proprietary to Semtech™ and LoRa Alliance. Therefore, designing a LoRa communication system consists of, besides the selection of the end-devices' hardware, the decision making on the key values for the LoRa parameters and software development. These key LoRa parameters were:

- The carrier frequency;

- The signal bandwidth;

- The spreading factor;

- The coding rate;

- The transmission power;

The bandwidth and the spreading factor affect the time-on-air of the LoRa module, the data transmission rate as well as the overall range of the radio link. The LoRa modem (RF1276-868) supported four signal bandwidths, namely, 62.5, 125, 250 and 500 kHz. Nevertheless, this modem had a fixed undefined value for coding rate that could not be changed. The carrier frequency used was strongly dependent on the radio hardware acquired for the design, and it was 869.5 MHz.

Similar to the LoRaWAN protocol, there were a few other parameters specific to the RF1276-868 LoRa module that must be set by the user. These parameters were:

- **The UART baud rate**: This is the UART baud rate between the host controller (Main MCU) and the LoRa modem;

- **The RF mode**: This could be the standard mode (value of 0) or the low power mode (value of 1) or in sleep mode (value of 2);

- **The network ID**: This was used to differentiate two LoRa networks from each other. The RF1276-868 LoRa modules are engineered to ignore data transmitted over their operating

frequency unless the node where this data originated had the same network ID. This parameter was a byte in length and varied from 00 to FF in Hexadecimal (base 16);

- **The node ID**: This set the naming for the different nodes (end-devices) in the network. It is two bytes in length.

- **The serial baud rate**: As the radio was connected to another secondary MCU in RF1276-868, this baud rate defined the rate of information exchange between the secondary MCU and the radio;

- **The serial parity**: This defined the presence of the parity error check for the connection between the secondary MCU and the radio (RF transceiver);

3.3.3 The Design

The selected values for the parameters and mode of operation for the initial LoRa system design were summarised in Table 3.4:

Table 3.4: The key parameters of the RF1276-868 and their designated values for the initial LoRa system design. For the remainder of the research, these key parameters will be called RF1276-868 parameters.

Parameters	Designated Value
Signal Bandwidth	125 kHz (Recommended)
UART Baud Rate	9600 bps (Recommended)
RF Mode	0 (Standard Mode)
Network ID	5 (0x05)
Node ID	0 and 1 respectively for the two nodes
Serial Baud Rate	9600 bps
Serial Parity	2 (0x02: Even Parity Check)

The standard mode was selected as this initial design focused on getting the LoRa radio link running between two nodes to investigate the relation of the transmission power to the range in the context of the sea (ocean) surface radio communication. Therefore, the transmission power and the spreading factor were explored.

The following section describes the implementation and testing of the initial design.

3.3.4 Implementation and Testing of the First Design

The implementation encompassed the development of the software to set the parameters of the network and the application layer for the two distinct hardware configurations illustrated in Figure 3.4. Arduino sketches were written for the transmitting end node and the receiving end node in the case of the hardware using Arduino as the primary host controller. These sketches are provided in Appendix B. Similarly, for the computer as the primary host controller, Python scripts were created to transmit, receive and process (display) data. These Python scripts can

be found in Appendix B. The Python scripts were used to configure the nodes by reading and setting the values of the RF1276-868 parameters.

After a successful implementation of the two nodes, the communication system was tested in two stages. The first test sought to:

- Confirm the establishment of a LoRa radio link between the two nodes and the readiness of the system for the field test;

- Define an acceptable transmission rate that would ensure the successful reception of the total payload data;

- Identify, for a given range, the minimum transmission power and the minimum spreading factor required for a successful transmission from one node to the second.

The range for this test was set to 320 m of LoS over land. During this test, the computer-based node was used at one end as the master node; the Arduino based node was used at the other end as the slave node. Both nodes were set at the minimum spreading factor (SF = 7) and with the same network ID. The test was run as follow: The master node initiated the connection by transmitting a line of data while the slave node was monitoring the network communication. Upon reception of the line of data, the slave node would send an acknowledgement token back to the master node. The number of lines of data sent from the master and the number of acknowledgements received by the master was compared at the end of the test and a conclusion was drawn. The minimum transmission power, i.e. 4 dBm was used for this test. The line sent from the master node encompassed:

- A start word "Start";

- Data;

- An end word: "end".

The acknowledgement sent from the slave node was: "Acknowledgement: Message Received". A few tries were executed, but only the results of the first three are summarised in Table 3.5.

Table 3.5: Result of the first test. Only the results of the first three tries are show here as the results were consistent through the whole test.

Try	Number of lines sent	Number of Acknowledgements
1st try	25	25
2nd try	25	25
3rd try	25	25

The results showed that the system was ready for field tests and that the minimum transmission power (4 dBm) was enough to achieve a successful transmission over a distance of 320 m using a spreading factor of 7. For each of the lines sent, the corresponding acknowledgement was received by the master node. Nevertheless, this test had a limitation, the integrity of the
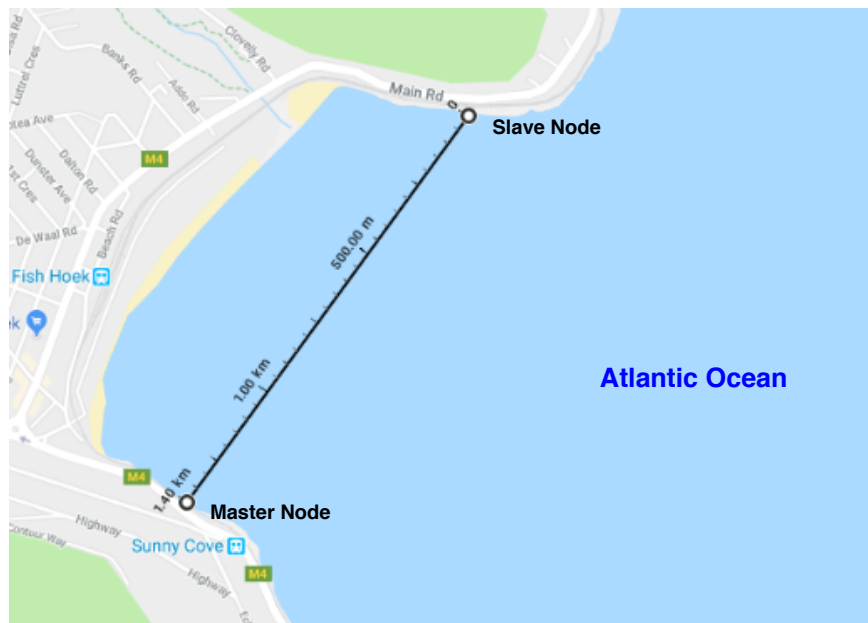
Figure 3.6: Extracted map showing the position of the nodes and the distance between the two nodes during the field test of the initial LoRa system design. This map was modified from Google Maps of Fish Hoek Bay in Cape Town.

payload received by the slave node could not be confirmed. To overcome this limitation, one should monitor the integrity of the data at the slave node by using a computer-based node at both nodes or by saving the received packets for analysis at the end of the test. Alternatively, one could resend the received data at the slave node back to the master node, but in this case, if the data becomes corrupted at the master node, it would be difficult to pinpoint at what point of the round trip the signal was corrupted. These deficiencies would be taken into account for the second stage of the test.

The second test was in the context of the communication over (or near) the surface of the ocean. This test was conducted across Fish Hoek Bay in Cape Town as illustrated on the extracted map in Figure 3.6. The nodes were 1.4 km (measured from Google Maps) apart from each other. Taking into account the limitation lessons from the first test, two computer-based nodes were employed in this test. The antennas were mounted on poles in a way that their lower end was at the mean level of the water.

This test aimed to assess the reliability of the proposed LoRa system and the LoRa radio Link near the surface of the ocean. Starting from the lowest transmission power level, i.e. 4 dBm, and the highest spreading factor (SF = 12), the test followed these two directives:

(1) If the payload data completed the round trip (from the master node to the slave node and Back to the master node) intact, decrement the spreading factor and start retransmitting at the previous transmission power;

(2) Otherwise, increase the transmission power level and continue to (1).

Sixty packets were transmitted for each combination of the transmission power and spreading factor. The results of this test are summarised in Table 3.6. The transmission was successful

Table 3.6: Summary of the outcome of the first field test conducted across Fishhoek Bay in Cape Town.

Transmission Power (dBm)	spreading factor	Outcome
4	12	Successful
4	11	Successful
4	10	Successful
4	9	Successful
4	8	Successful
4	7	14% of the total packets dropped

at 4 dBm with spreading factor equal to or bigger than 8. In other words, the payload data completed the round trips with the minimum transmission power for all the spreading factor values except for the lowest the spreading factor (SF = 7) where 14% of the payload were somehow dropped. Even though the packet drops could have been caused by the interference of other sources, some physical phenomena could be argued to be the cause of the dropped packets. It could be that during the transmission of these packets, a large wave blocked the LoS between the two antennas. Alternatively, maybe the signal was reflected (or absorbed) by the surface of the water. These are only hypotheses at this point. The rest of the dissertation considers these hypotheses in more detail, but first, it focuses on a different LoRa system that uses a Single MPU end-device configuration. This second option for the LoRa transceiver was necessary to make a consistent decision on the adequate LoRa transceiver for a maritime application.

3.4 Second LoRa System Design and Implementation

The RF1276-868 module formed the starting point of the application of the LoRa radio modulation to the quasi-local ocean surface communication using the Wave Glider as a case study. Nonetheless, a few of its prime features were not disclosed to the public, namely the specifications of the secondary MCU. Besides, the main logic behind the preference of LoRaWAN™ as the alternative communication technology was to minimise the power usage of the communication system. Thus, the use of a split end-device architecture was counter-intuitive when there was a single MPU end-device option. In other words, one micro-controller, instead of two, was the preferred option for power efficiency. In this context, the second design was carried out to improve on the shortcoming of the RF1276-868 based system and more predominantly equip the research with a second LoRa communication system. This second design featured, as aforementioned, a single MPU end-device architecture and it used a B-L072Z-LRWAN1 Discovery board from STMicroelectronics [11].

The B-L072Z-LRWAN1 board was preferred to replace the RF1276-868 module because it was designed to operate on stand-alone with AAA batteries as the main power supply and an antenna. Also, it was designed around the STM32L072CZ MCU which was part of the family of the ultra-low power micro-controllers from STMicroelectronics. These made the
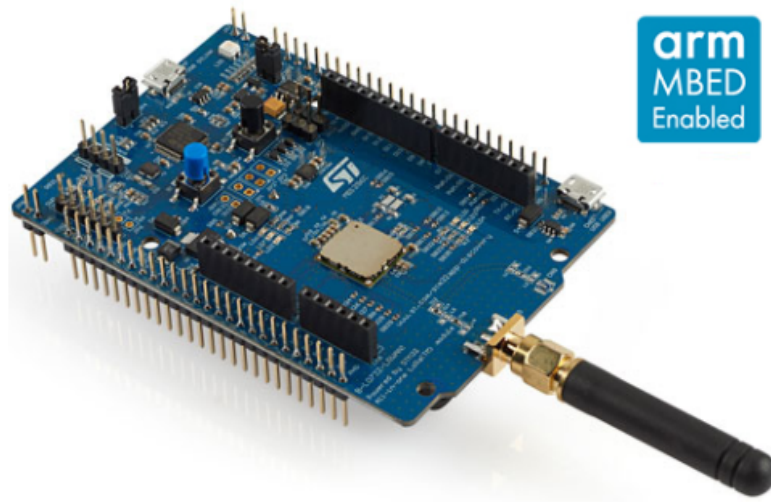
Figure 3.7: Image of the B-L072Z-LRWAN1 discovery board from STMicroelectronics [11].

B-L072Z-LRWAN1 an adequate LoRa module for use in the marine environment. Similarly to the RF1276-868 module, the B-L072Z-LRWAN1 used the SX1276 transceiver microchip from Semtech™. The most relevant attributes of the B-L072Z-LRWAN1 can be found on the product website [11]. It could execute LoRaWAN™ protocols for Class A and Class C.

Another of the advantages of the B-L072Z-LRWAN1 over the RF1276-868 was the development of its software application in the embedded C programming language. The use of embedded C optimised the execution and processing time at the LoRa system nodes. Besides the choice of the board, the design process continued on with the development of the software for the application layer, the radio drivers and sensors drivers. The radio drivers were publicly available for the SX1276 transceiver users, and a demo research on the application of the board was supplied in the I-CUBE-LRWAN firmware package by STMicroelectronics. These resources helped develop the application layer for the new LoRa code (which is given in Appendix B). The LoRa design parameters were the same as in the previous design. The remaining parameters, as in Table 3.4, that were only relevant to the RF1276-868, were not part of this design. A picture of the B-L072Z-LRWAN1 is displayed in Figure 3.7.

3.5 Testing and Comparison of the Two LoRa System Designs

The first design was tested in the field over the ocean before the second design was completed. The results of this first test served as a proof of concept of the strong possibility to use LoRa radio technology to fulfil the purpose of this research. At the completion of the second design, the two systems were tested together in the same conditions both in-land and over the ocean. The two systems were set at their maximum transmission power of 20 dBm and at the maximum spreading factor (SF = 12). The results were monitored to determine if the system performed better in terms of received signal power.

The in-land test was done at the upper campus of the University of Cape Town across the Rugby Fields (GPS location at -33.957716, 18.462764). The distance between the master node and the slave node was 380 meters. The antenna height was set to 1 meter. The principal aim of this in-land test was to have a baseline of the power performance of both LoRa systems, especially the level of the received power in the hope that it would guide the expectation of the systems' potential over the surface of the ocean with a large distance between the two nodes. The Received Signal Strength Indicator (RSSI), i.e. the received power levels recorded from this test are outlined in Table 3.7.

Table 3.7: Results of the in-land test comparing the performances of the two LoRa systems design over a distance of 380 meters.

LoRa System	RF1276-868	B-L072Z-LRWAN1
Range of RSSI Value (dBm)	-107 to -117	-118 to -129
Average RSSI Value (dBm)	-109.28	-120.82

The results indicate that the LoRa system based on the RF1276-868 radio module had a stronger received signal compared to the B-L072Z-LRWAN1 LoRa system. The received signal power from the RF1276-868 was, on average, 14.25 times stronger than the one from B-L072Z-LRWAN1. At this point, the RF1276-868 LoRa module was preferred over the B-L072Z-LRWAN1 discovery boards for the next test.

The second test was conducted across Table Bay in Cape Town. The antennas were placed near the surface of the ocean to ensure that the signal passed over the surface of the ocean from the master node to the slave nodes and back. This test was similar to the one carried out across the Fishhoek Bay except that the distance between the two nodes was five kilometers this time and the received power was monitored at the slave node. The geographical positions of the two nodes are revealed on the map in Figure 3.8. The experiment aimed to evaluate the effect of the sea (ocean) water and the sea surface wave on the reception of the packets and the levels of their received power. The protocol used for this experiment is outlined in Appendix A. The nodes in this experiment were set up using the RF1276-868 LoRa module as per the split end-device configuration. The independent variable in this experiment was the antenna height above the mean sea level, and the dependent variables were the received power level, and the packet drop rate. The external influences on this experiment were the wind speed and direction, as well as the tide level.

A successful radio link was established during the experiment. The dependent variables of this experiment were monitored and recorded as results. These results are presented over the next two chapters. The set-up of this experiment was not ideal as the building and structures behind the antenna may have provided indirect channel interference between the two nodes.
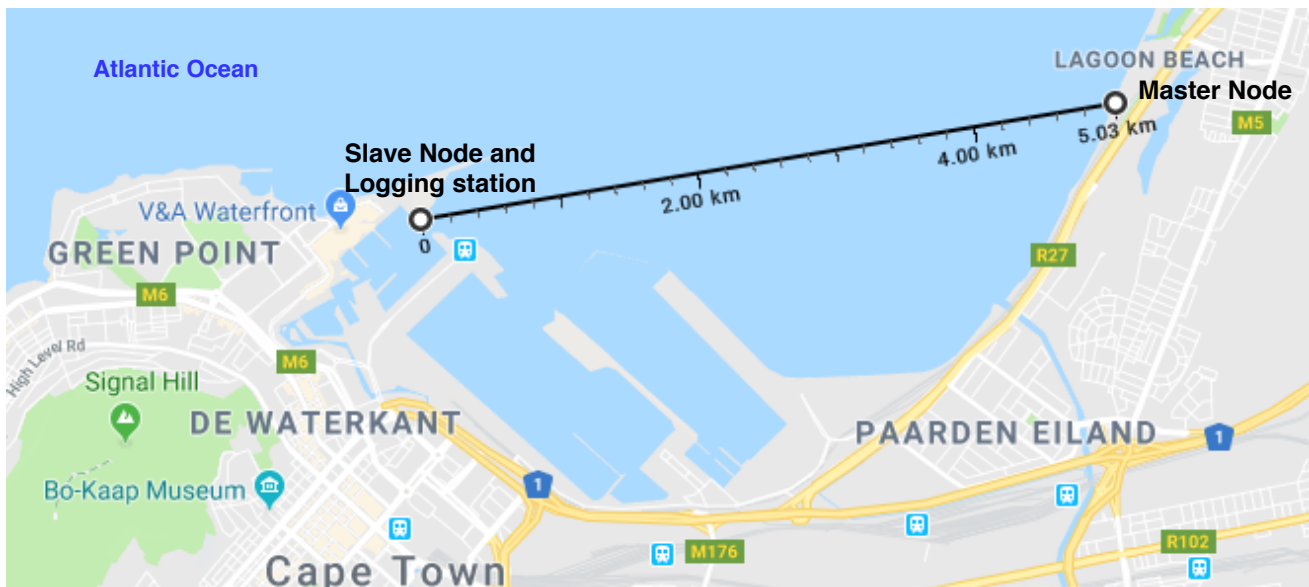
Figure 3.8: Extracted map showing the position of the master and slave nodes and the distance between them during the long distance experiment. The map was extracted from Google Maps for Lagoon Beach and V&A Waterfront area in Cape Town.

3.6 Conclusion

In this chapter, the LPWAN technology, LoRa was presented. The two point-to-point LoRa communication systems were designed to be an alternative local and low power communication system for small unmanned surface marine vehicles. The design processes were explained in detail. The tests that were carried out both in-land or over the ocean, evaluated the performances of the LoRa systems. The first test over the ocean was carried out across the Fishhoek Bay in Cape Town, with the first design based on the RF1276-868 LoRa module. This test revealed that the LoRa technology is a strong candidate technology in terms of low power communication over the surface of the sea. During this test, the effect of the seawater or the surface waves were not evaluated. Thus, a second LoRa design and further experiments were conducted to lay the basic understanding of the power behaviour at the reception of the packets and eventually evaluate the physical effects of the ocean that were missed in the first test.

After running the first comparison, in-land, between the two LoRa designs to establish the ground truth of their relative capabilities, a second experiment over the ocean, similarly to the first one, but with a significant increase in the distance between the two nodes, was conducted to evaluate the effect of the ocean as mentioned earlier. The distance was increased from 1.40 kilometers in the first test across the Fishhoek Bay to 5 kilometers across Table Bay. Given that this test was conducted over this long range, it was also critical to account for the effect of the height of the antenna from the mean sea water level and the Earth's curvature. They could affect the channel between the two nodes besides the obstacle represented by the ocean itself. In fact, the Earth curvature constituted approximatively a vertical height of 1 meters over the distance of 5 kilometers and 2 meters over the distance of 10 kilometers.

In a nutshell, to fully comprehend the results of the second ocean test conducted on the LoRa systems, a quantification of the impacts of the factors alluded above was essential. In other words, this research considered further the impacts of:

- The seawater by studying its electromagnetic (EM) properties;

- The presence of the ocean surface waves together with the Earth's curvature and the antenna heights.

The next two chapters covered the study of these factors, starting with the electromagnetic properties of seawater.

Chapter 4

Electromagnetic (EM) Properties of Seawater and FEKO Simulations

The capacity of any communication system depends strongly on the terrain where the system is operated [54, 55]. Whether it is terrestrial, offshore, or in space; whether it is an open rural area or a clustered urban area, the physical world affects the overall performance of the network system. As it stands, one cannot design a communication system for a particular terrain, for example, an open rural area, and expect this same system to perform precisely the same as in an urban area with dense buildings. To some extent, each communication system is customised to its terrain. Of course, to be able to align the design to the terrain, some knowledge of the terrain and the manner in which it can affect the communication system is required. As this research aims to propose a local communication system for marine surface vehicles, the specific environmental features of the sea must be considered.

To achieve a reliable and robust local communication system, we need to visualise and understand how the marine environment and the seawater interface would affect the transmission of radio signals near the surface of the ocean as compared to the free space transmission in the context of this research. This was realised by simulations using FEKO, an EM simulation platform [56]. The method and set-up are described in this chapter, starting with a brief overview of the theory on the EM properties of seawater.

4.1 EM Properties of Seawater and FEKO Software

4.1.1 EM Properties of Seawater

An alternative communication system is proposed in this dissertation for local information sharing via radio signal near the ocean surface. This proposed system strongly relies on the ultra-low power consumption of the transceivers. Radio communication in the marine environment presents different and difficult challenges compared to its terrestrial counterpart due to the lack of infrastructure. The seawater is an electrical conductor, and to construct a robust marine network, an understanding of the seawater medium is of great value as seawater affects the propagation of radio waves. Seawater medium has a particular set of EM attributes that, depending on the frequency (or wavelength), could have a constructive or destructive effect on the radio signal. In other words, seawater can be modelled as a good conductor or an

imperfect dielectric. The explanation of this statement follows from the approximations below.

For microwave frequencies, the total current density can be expressed as [57]:

$$\mathbf{J} = j\omega\epsilon' \left(1 - j(\frac{\epsilon''}{\epsilon'} + \frac{\sigma}{\omega\epsilon'})\right) \mathbf{E}, \tag{4.1}$$

where j is the imaginary number defined by $j^2 = -1$; ϵ' and ϵ'' are the real part and the imaginary part of the material's complex permittivity; σ is the (real-valued) conductivity of the material; ω is the frequency of propagation in radians.

The term $j(\frac{\epsilon''}{\epsilon'} + \frac{\sigma}{\omega\epsilon'})$ represents the loss factor of the material and the real value $(\frac{\epsilon''}{\epsilon'} + \frac{\sigma}{\omega\epsilon'})$ is the "loss tangent", $tan\ \delta$. For dielectric materials, the conductivity σ is taken as zero. Thus, the dielectric losses can be quantified by the simplified "loss tangent":

$$tan\ \delta \approx \frac{\epsilon''}{\epsilon'}. \tag{4.2}$$

Similarly, for conductors, the conductivity encompassed all the loss, making the total current density equal to:

$$\mathbf{J} = j\omega\epsilon' \left(1 - j\frac{\sigma}{\omega\epsilon'}\right) \mathbf{E}. \tag{4.3}$$

If the ratio $\frac{\sigma}{\epsilon'}$ is smaller than the frequency (in radians), the loss is very small and the "loss tangent" can be approximated as:

$$tan\ \delta \approx \frac{\sigma}{\omega\epsilon'}. \tag{4.4}$$

In the case of seawater, which is a conductor, the conductivity σ is given in [57] as 4 S/m, and agrees with the results in [58] which showed that the ocean conductivity varies from 2.5 to 5.5 S/m and that it is dependent on the salinity, temperature and pressure parameters (water depth for instance) in the global ocean circulation model. In the meanwhile, the permittivity of the seawater is given by the ratio $\frac{\epsilon'}{\epsilon_0} = 81$ where ϵ_0 is the vacuum permittivity constant equal to 8.854×10^{-12} F/m. At the frequency 868 MHz and taking $\sigma = 4\ S/m$, the "loss tangent" is:

$$tan\ \delta \approx \frac{\sigma}{\omega\epsilon'} = 1.0227. \tag{4.5}$$

The result in (4.5) means that the ratio $\frac{\sigma}{\epsilon'}$ is approximatively equal to the frequency, ω. At this frequency, the seawater lies at the boundary between a good conductor and a lossy dielectric. In the context of the subsequent simulations, seawater was considered as a lossy conductor with the "loss tangent" given by the result in (4.5).

4.1.2 A Brief Description of the FEKO Software and Related Works

a) FEKO: Description

FEKO is a widely used Computational Electromagnetic (CEM) software from Altair [56]. It is used to solve a variety of EM problems in the maritime, aerospace or telecommunications industries. Its main applications include, amongst others, antenna design and placement, Elec-

tromagnetic Compatibility (EMC) analysis, bio-electromagnetic, waveguides and microstrip circuits. FEKO can be set-up to find solutions to customised EM problems as was the case in the research.

FEKO is subdivided into two separate user-interfaces, namely CADFEKO GUI and POST-FEKO GUI. CADFEKO GUI is used to construct the complete EM problem in all of its geometrical details and to generate meshes before running the EM solvers. POSTFEKO GUI is employed to visualise, in 2D or 3D, the solutions obtained from the EM solvers. POSTFEKO GUI is also used to extract reports on the solution into commonly available document formats. The different EM solvers in FEKO's software package can be separated into two main categories, rigorous and asymptotic, depending on the methods the solver employs to get its solutions. The rigorous solvers are [12]:

- **Method of Moments (MoM)**: This solver is recommended for EM studies involving radiation and coupling. It fully solves Maxwell's integral equation for wave solutions in the frequency domain. It is numerically very efficient for small size EM problems but is computationally demanding as the size of the problem increases.

- **Multilevel Fast Multipole Method (MLFMM)**: It is a substitute formulation of the MoM. It is strongly linked to the electrically large EM problem. It presents a significant advantage over the MoM in computational requirements as it looks for the solution for groups of mesh elements instead of each element at a time.

- **Finite Difference Time Domain (FDTD)**: Recommended for broadband frequency analysis, and for modelling of inhomogeneous bodies, this solver is a time domain method that uses Fourier Transform analysis to convert its time domain solutions into frequency domain solutions.

- **Finite Element Method (FEM)**: It is a volume discretisation method for representing random shapes using tetrahedral mesh elements. It is the recommended solver when dealing with EM problems containing many dielectric entities. It is generally used in conjunction with the MoM for the solution. It can also be used with the MLFMM for large geometries.

Moreover, the asymptotic solvers are [12]:

- **Physical Optics (PO)** is a current-based asymptotic high-frequency numerical method that is suggested for very large radiation and scattering investigations concerning metallic or dielectric structures.

- **Large Element Physical Optics (LE-PO)** is similar to the PO method, but it allows a bigger number of mesh elements and therefore it is used for larger bodies. It can be a substitute for the PO method.
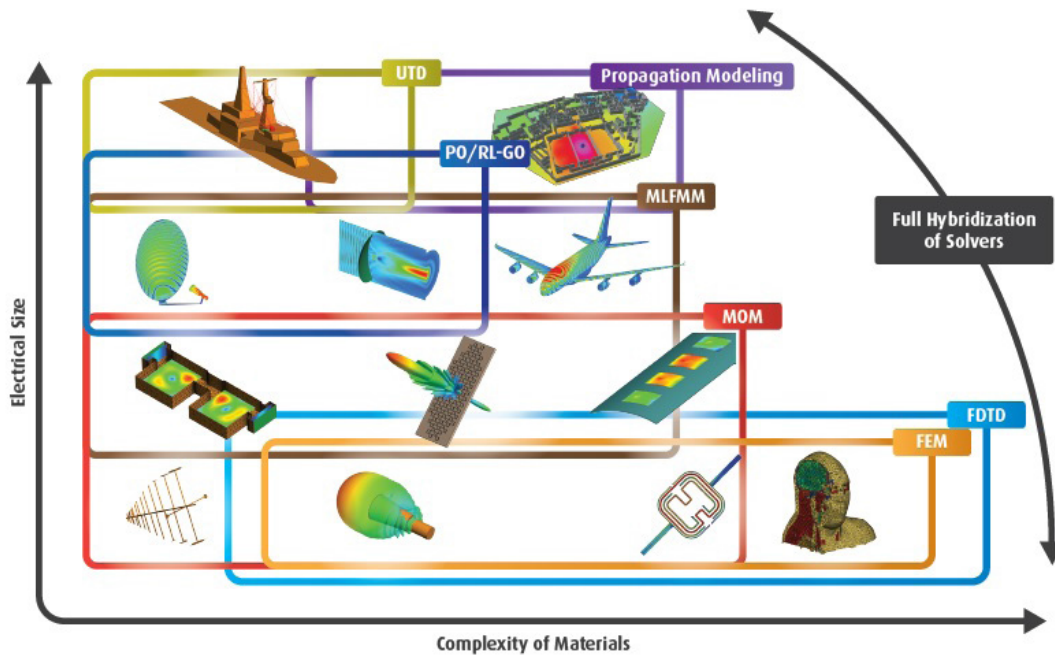
Figure 4.1: Graph showing the different numerical solvers found in the package of FEKO relative to the complexity of EM materials and the sizes of the models. Taken from [12].

- **Ray Launching Geometrical Optics (RL-GO)**: This solver is also suitable for electrically enormous metallic and dielectric scattering problems. This method involves shooting rays from all radiating mesh elements and using the Huygens sources to model interaction of the rays with any metallic or dielectric materials in the problem.

- **Uniform Theory of Diffraction (UTD)**: This solver is the one proposed for huge EM problems. It works better with Perfect Electrically Conduction material (PEC). FEKO combines this solver with the current-based MoM to improve the accuracy of the solutions.

Figure 4.1 shows the different EM solvers and their capabilities regarding the size of the EM problem in space and the complexity of the EM materials involved in the EM problem. The region of operation of these solvers is correlated to the actual problem since the unit of the size is not outlined. The typical applications where the different solvers are commonly employed are hinted at on the graph. This graph also illustrates the overlap between the different solvers, meaning that for a particular EM problem, more than one option of solvers is available to the users.

39

4.2 Radio Wave Simulations using FEKO

The main of objective of the simulations was to investigate how the ocean surface (seawater) interacts with the radio signal emitted by the LoRa transceivers in the context of the design of a LoRa network at the frequency of 868 MHz for surface marine vehicles such as the Wave Glider platforms. With every detail drawn from the geometry of the numerical experiment, a model was derived for the simulations. This model does not include individual surface waves. The 2017 version of FEKO was employed to execute the different simulations.

4.2.1 FEKO Model Setup

The model comprised two antennas (nodes), the medium of transmission which was, in this case, air (or vacuum) and seawater (ocean surface). The two nodes were separated by a distance D. An illustration of the geometry of the experiment was given in Figure 4.2.

The Earth's curvature was incorporated into the arrangement elucidated in the figure above. The height conferred by the curvature was dependent on the distance, D, between the two nodes. This height was approximated using the following expression for a fixed distance D. Figure 4.3 was given to support logic on which the approximation of this height is based. For example for a distance of D equal to 10 kilometers, Δh was equal to approximatively 2 meters.

$$\Delta h = R - \sqrt{R^2 - \left(\frac{D}{2}\right)^2}. \tag{4.6}$$
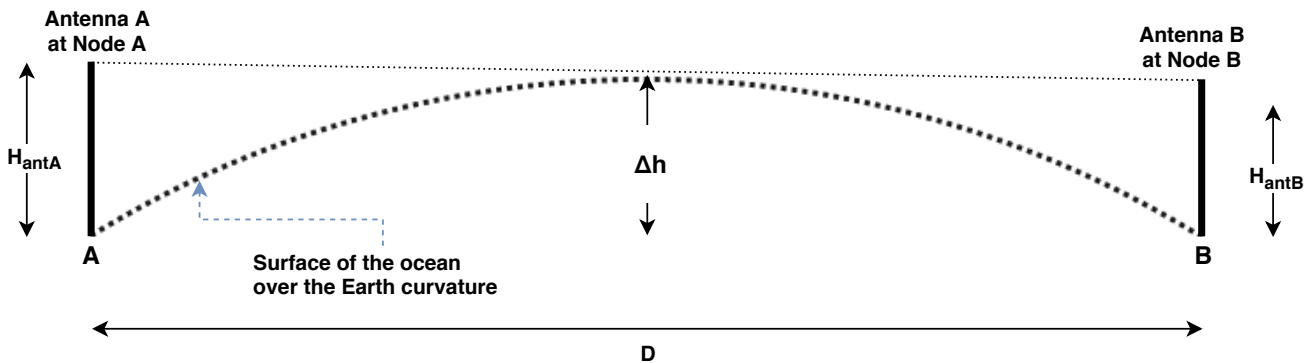
Figure 4.2: Two-dimensional geometry illustrating the position of the antennas and showing the curvature of the Earth. Here, the surface of the ocean was regarded as the mean seawater level, ignoring the presence of surface waves for simplicity. The antennas are normal to the local surface.

Working from the 2D geometry in Figure 4.2, a 3D FEKO model was constructed on CAD-FEKO. This model is shown in Figure 4.4. Granted that the model was a substantial structure in the context of EM simulation, the UTD solver was preferred over the rest because the UTP solver is recommended for geometrically vast EM problem similar to the one in this research. Also, this solver reduces the computation associated with solving the EM problem by working
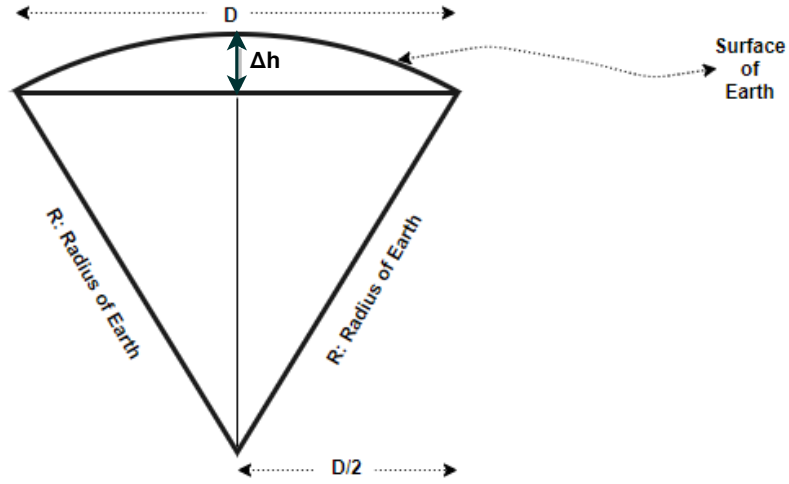
Figure 4.3: Extension of the geometry in Figure 4.2 demonstrating the logic for the approxima-tion of the height of the Earth's curvature.

around flat surfaces as they are and not dividing them into smaller meshes. However, this approach only apply to the flat surfaces.

The two antennas were modelled as half-wavelength dipole antennas. Given that the frequency of interest was 868 MHz, the wavelength is:

$$\lambda = \frac{C}{f} = \frac{2.997 \times 10^8 \ m/s}{868 \times 10^6} = 0.3452 \ m. \tag{4.7}$$

Therefore, the antenna height was 0.1726 m in the model. The blue-white-red sphere in Figure 4.4 represented the antennas. The total maximum power that each antenna (node) could transmit was fixed at 20 dBm, which is the highest transmission power of the LoRa modules. The ocean surface was modelled as a lossy conductor with the loss coefficient set to the value calculated in the previous section. Considering the roundness of the Earth, the ocean surface in the 3D FEKO model was constructed as a paraboloid with a circular base instead of a sphere. The paraboloid was preferred to a sphere (for the surface of the Earth) primarily because it allowed the scaling down of the problem to a working size that FEKO can handle with minimum computational issues. The focal depth of the paraboloid was chosen such that the height at the centre of the paraboloid was equal to the value of Δh calculated for the diameter. This model does not include the presence of ocean surface waves and assumes a smooth ocean surface. The surface waves are included in the study in the next chapter. Finally, the thickness of the surface of the ocean was set to 1 meter. The value was selected to be much larger than the skin depth, δ_{se}, which is around 15 mm at 868 MHz as shown in (4.8) [59].

$$\delta_{se} = \sqrt{\frac{1}{\pi f \mu \sigma}} = 15.13 \ mm \tag{4.8}$$

where the permeability of seawater, μ, is $1 \times 4\pi \times 10^{-7}$ H/m.

(a) Isometric view

(b) Front view

(c) Left view

(d) Top view
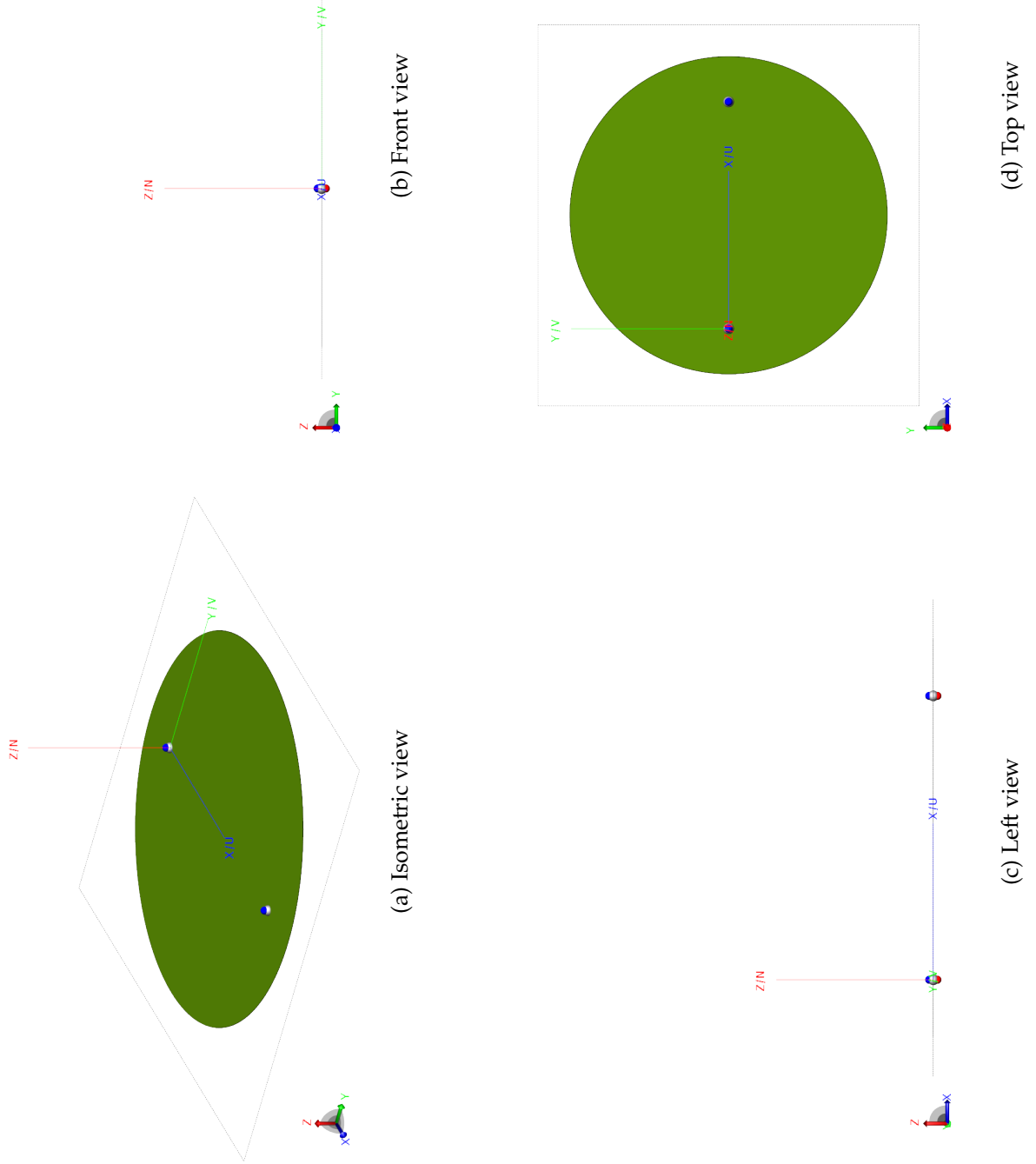
Figure 4.4: Three Dimensional Model Developed in CADFEKO. The base radius of the paraboloid was 7 km giving the heigh Δh equal to 3.8455 m. The ratio of the height over the diameter was too small. Thus the surface seemed flat.
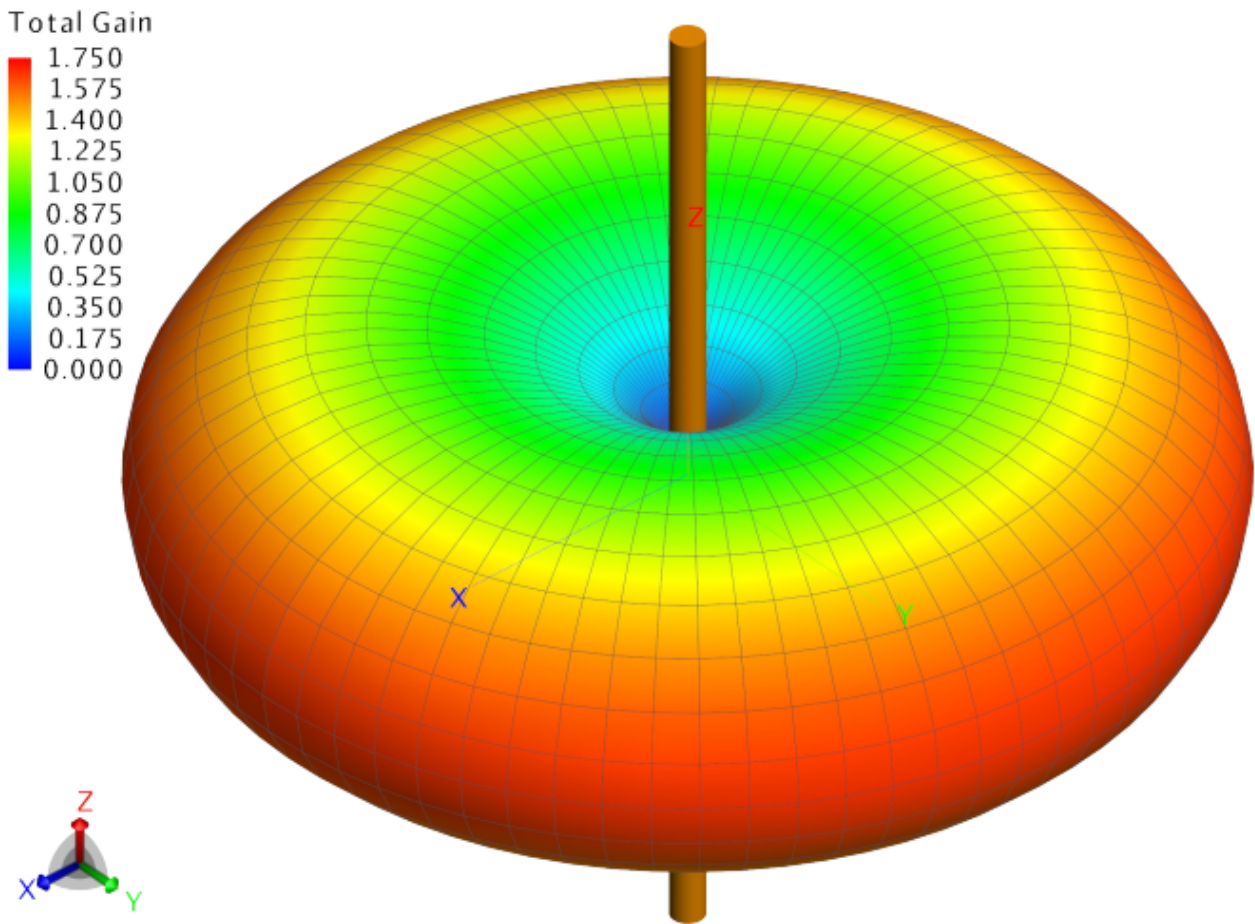
Figure 4.5: Power radiation of the half-wavelength dipole antenna in free space.

4.2.2 Simulation and Results

The simulation consisted of creating the meshes for the model and solving the EM problem posed by the model using the built-in EM solver of FEKO. It started with the simulation of the half-wavelength dipole antenna in free space; this was done to visualise the propagation pattern of the signal transmitted by such an antenna in a vertical position. This pattern is shown in Figure 4.5. As expected, it demonstrates that the power was radiated evenly in all radial directions normal to the antenna. Assuming this result is the reference point, the simulation was repeated, this time the antenna was placed near the surface of the seawater similarly as in the model shown in the previous subsection. This second simulation was to conceptualise the consequences of the seawater surface near the source of transmission. The result is presented in Figure 4.6.

The result of the second simulation was inconsistent with the first one. The surface of the seawater appeared to affect the propagation pattern of the antenna significantly. The majority of emitted signals were reflected in the upward direction (away from the surface) by the seawater surface. Nevertheless, a small percentage of the power was absorbed by the seawater surface. The reflection from the seawater makes the pattern directional, which explains the increase of the total gain in Figure 4.6. It should be emphasised, here, that these results were for signals transmitted at the frequency of 868 MHz.

(a) Isometric view

(b) Front view
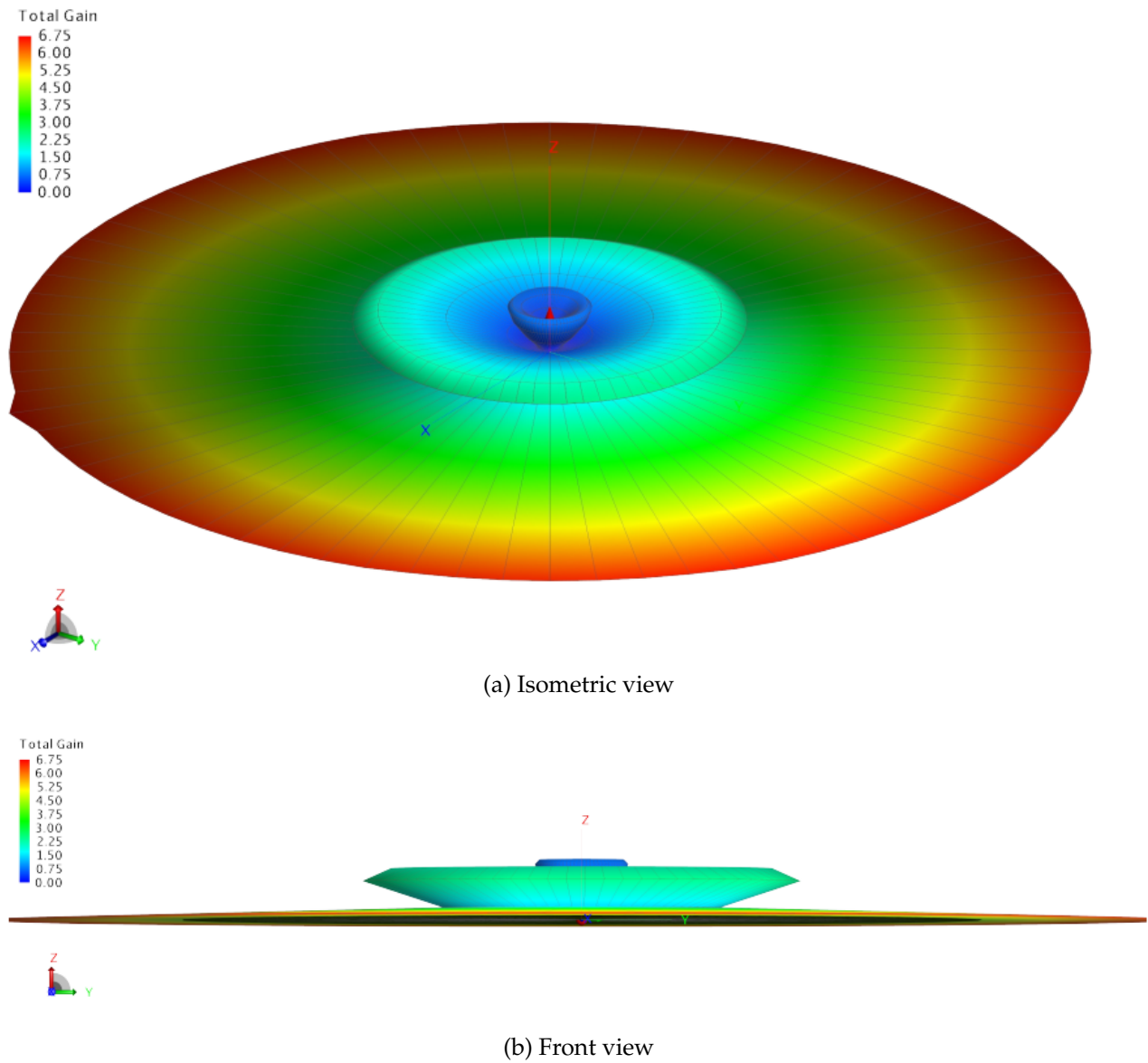
Figure 4.6: Power radiation of the half-wavelength dipole antenna on the surface of the seawater (ocean surface). The radiated signal is above the surface.

Table 4.1: Power levels at the receiver antenna for different orientations of the transmitter antenna in the ZX and ZY planes. These results are compiled for a distance of 10 km and 5 km separating the two antennas respectively in the model. The transmitted power was 20 dBm.

Orientation		Power Level (dBm)	
Plane	Angle (Degrees)	10 km	5 km
ZX	0	- 74.98	- 71.33
	15	- 75.35	- 71.79
	30	- 76.70	- 73.17
	45	- 79.20	-75. 52
	60	- 82.70	- 79.14
	75	- 88.90	- 85.31
ZY	0	- 74.98	- 71.33
	15	- 75.40	- 71.63
	30	- 76.30	- 72.58
	45	- 77.95	- 74.34
	60	- 80.95	- 77.35
	75	- 86.70	- 83.07

The first two simulations discussed above focused only on the use of one antenna transmitting at 20 dBm. The rest of the simulation looked at the FEKO model in Figure 4.4. The two antennas were separated by a distance of 10 km and were centred at 2 m above the surface of the seawater. One antenna was considered as an ideal source antenna with a maximum transmission power set at 20 dBm while the second antenna emulated an ideal receiving antenna. The EM problem of this arrangement was solved using the UTD solver. The source antenna's radiation in free space was solved first, and the solution was saved as a "ffe" file to reduce the computational burden and improve the speed of the simulation. The "ffe" file was then imported into the model displayed in Figure 4.4 showing the full model simulation.

During the simulations, the power level at the receiving antenna was monitored. Initially, the antennas were both vertically orientated. However, subsequently, the orientation of the antenna was varied in the ZX and ZY planes respectively. The received power was logged in each case. The received power levels are summarised in Table 4.1.

The maximum power level at the receiving antennas was -74.98 dBm when the transmitting antenna was vertical. It went as low as -88.90 dBm with the antenna at $\pm$ 75 Degrees to the vertical in the ZX plane. This minimum power was higher than the sensitivity of the LoRa transceiver. The sensitivity of the LoRa transceiver was -137 dBm [60]. The results of the simulation support the argument that the LoRa communication system proposed in this dissertation was adequate for the deployment on the surface marine vehicles such as the Wave Glider platforms.
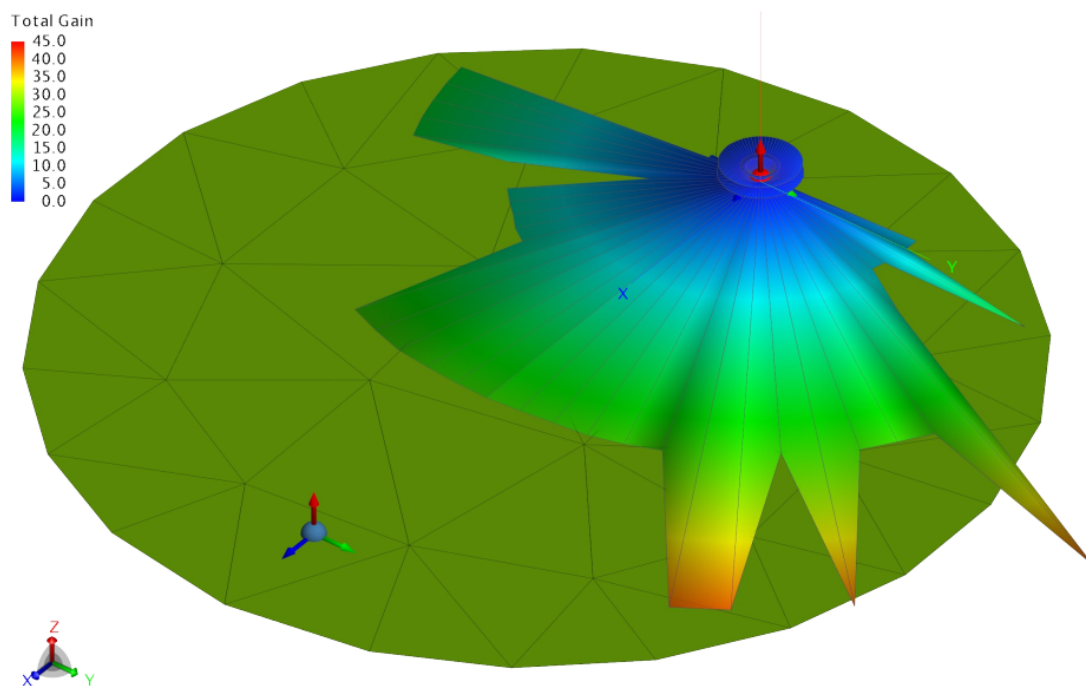
Figure 4.7: Visualisation of the solution to the EM problem in POSTFEKO. The radiation from the source antenna is shown. The asymmetrical pattern of the radiation is due to the graphical limitations of the POSTFEKO. This radiation pattern was in agreement with previous results.

For completeness, the visualisation of the solution of the EM problem was given in Figure 4.7. This solution is for the simulations where the two antennas were vertical. The visualisation was seen in POSTFEKO. The radiation pattern of the source antenna shown is similar to the one in Figure 4.6, although the two simulations were completed differently.

4.3 Practical Results

The practical results described in this section were the results of the experiment organised and carried out over the sea. This experiment was introduced towards the end of the previous chapter. The LoRa systems designed from the RF1276-868 LoRa module was used. The positions of two nodes of the LoRa system were shown previously in Figure 3.8. The results here concerned the received power of the signal. Given that the distance separating the two nodes during the experiment was 5 km, another set of FEKO simulations were conducted similarly to the one in the previous section. However, the distance between the transmitter and the ideal receiver was shortened to 5 km and the antenna height was set to 1 meter. The results of these simulations were appended to Table 4.1. With the distance shortened, the received power levels had improved marginally. When the antenna was vertical, the received power at the ideal receiver was -71.33 dBm compared to -74.98 dBm when the distance was 10 kilometers.

The results of the experiment are outlined in Table 4.2. The heights in the table were the

Table 4.2: Averages and the standard deviations of the recorded received power during the experiment conducted across the ocean over a distance of 5 kilometers. The average was taken over 120 recorded power values for each antenna height. The height of the antenna's base were (harshly) evaluated from the mean ocean water level.

Height of antenna's base (meters)	Average received power (dBm)	Standard deviation (dBm)
0	- 82.55	3.20
0.25	- 81.61	1.95
0.50	- 74.52	3.08
0.75	- 72.77	2.59
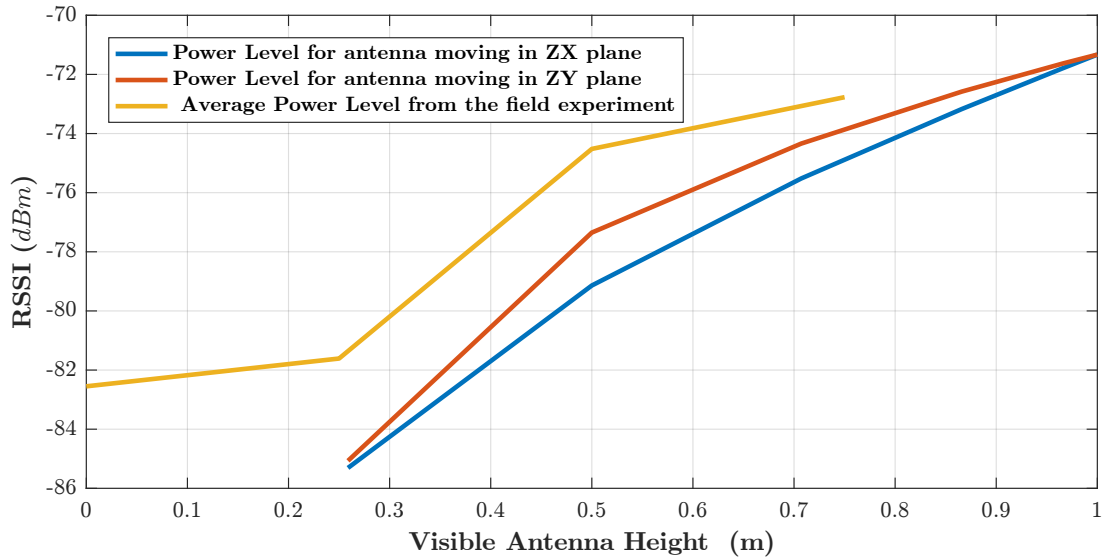
Figure 4.8: Comparison of the received power from simulations and the field experiment.

vertical distance between the mean surface of the seawater and the lower end of the antenna. The antenna itself was 0.82 meters high. The power levels recorded during the experiment were comparable and in agreement with the simulation results in Table 4.1 regarding the 5 kilometers antenna separation distance. In addition, the recorded received power level was proportional to the total height of the antenna as the the received power improved with the increase in the total height of the antenna. This also confirms with the behaviour of power levels from the FEKO simulation because the angle of orientation could be interpreted as a change in the total height of the antenna.

The received power levels in Tables 4.1 and 4.2 are plotted in Figure 4.8. The received power levels are plotted against the vertical component of antenna height, which is the product of the antenna height (1 meter) and the cosine of the orientation angle in Table 4.1, for the simulations results. The received power levels are against the height of the antenna's base for the experiment results. The plots follow a similar trend, demonstrating a good agreement between the simulations and the field experiment. The results of the field experiment support the simulation results on FEKO.

4.4 Conclusion

This chapter addressed one part of research question regarding the effect that the ocean surface has on the performance of the proposed LoRa communication system. The low power wide area system was simulated in FEKO by an ideal emitter source transmitting at a maximum power of 20 dBm. This source was placed near a material simulating the properties of the ocean surface as illustrated in the FEKO model in Figure 4.4. With an ideal receiver antenna placed at a distance of 5 km and 10 km away from the source, the power levels at these distances were logged. The outcome of the simulations revealed that the power level at this distance away was still higher than the sensitivity of the LoRa transceiver. Therefore, this outcome reinforced the viewpoint that the proposed LoRa system is feasible for the local communication scheme for marine surface vehicles in general and Wave Glider platforms in particular. The viewpoint was strengthened by the results of an experiment conducted in real life as these practical results were in agreement with the simulation results.

Besides, the propagation pattern of the source antenna was generated and compared for two different scenarios: The source antenna placed in free space and the source antenna placed near the surface of the ocean surface. The results shown in this chapter demonstrate that the ocean surface redirected the majority of propagating power upward while there was a negligible power absorbed by the surface. The comparison of the power level obtained from the in-land experiment over a short distance described in the previous chapter (see Table 3.7) to the power level obtained from the experiment over the ocean with a longer distance in Table 4.2 suggests that the seawater reflected the signals and acts as an amplifier, thus improving the received power levels over the ocean. The received power was on average -109.28 dBm inland over a distance of 380 m compared to -82.55 dBm received on average over the sea for the same antenna height. This conclusion is solely valid at the frequency of 868 MHz.

FEKO was an adequate CEM tool for this study. Nevertheless, the spatial dimensions of the model designed for the study reduced the efficacy and efficiency of the software to analyse further the effect of the ocean surface on the capability of the LoRa system. Accordingly, the ocean surface waves were not included in the simulations. The ocean surface waves constituted the focus of the study in the following chapter.

Chapter 5

Probability of the Line of Sight

In the previous chapter, the focus was on the investigation of the influence of the ocean surface and the curvature of the Earth on the performance, i.e. the transmission and reception of information over a LoRa Network, where the presence of ocean surface waves was neglected. In this chapter, the influence of the ocean surface waves is now included in the model. The surface elevation of ocean waves is a stochastic process and based on the results in the previous chapter; the seawater surface redirects the antenna propagation pattern at 868 MHz. It was apparent from these two assertions that, stochastically, some transmitted packets would be dropped and not reach the receiver at the destination in the absence of a clear LoS between the two nodes. In other words, it is hypothesised that the signal conveying the information will be attenuated by a high enough ocean surface wave depending on physical quantities such as the two antenna heights and angles, elevation of the surface waves and the Earth curvature, to mention a few.

This chapter presents a probabilistic method to quantify the likelihood of attenuation and the probability of complete loss of LoS due to the presence of ocean surface waves. The first section reviews and discusses the theory on the probability distribution of ocean surface waves. This method is part of the solution initiated to improve the performance of the local inter-vessel communication with the use of opportunistic temporal channels similar to the meteor scatter communication channels. The meteor scatter communication is a communication method that relies upon the reflections of signals (at very or ultra-high frequency) by the trail of ionisation begotten by the meteors as they burn in the upper layers of the Earth's atmosphere [61]. The signals are only reflected for a short time as the density of the ions degrades. Furthermore, the reflection intervals are randomised as they depend on the meteor entering the Earth's atmosphere [62].

5.1 The Probability Properties of Ocean Surface Waves

5.1.1 Definitions

Before we look at the probability distribution functions, Figure 5.1 illustrates some important definitions in ocean wave theory that are relevant for the understanding of the content of this chapter:

- The surface elevation, $\eta(\mathbf{x}, t)$, is the vertical deviation of the ocean surface from the mean water level at $\eta = 0$. $\mathbf{x}$ stands for location (x, y), t is the time variable and $\eta(\mathbf{x}, t)$ is in a Cartesian coordinate system (x, y, z).

- The wave crest, A_c, is the maximum surface elevation between two successive down-crossings or up-crossings of the mean water level. The wave crest has a positive value.

- The wave trough, A_t, is the minimum (negative) surface elevation between two successive down-crossings or up-crossings of the mean water surface.

- The wave height, H, is the positive vertical distance from the trough to the crest of the wave ($H = A_c - A_t$).

- The wave amplitude, A, is half of the wave height ($A = \frac{H}{2}$).

- The wavelength, λ, of the wave is the horizontal distance between two consecutive crests or troughs of the wave.

- The wave period, T, is the time elapsed between two consecutive crests or trough passing through the same location $\mathbf{x}$ in space. T is usually expressed in seconds.

- The wavenumber is $k = \frac{2\pi}{\lambda}$ and represents the number of waves crests (or troughs) per unit of distance. It is also called the spatial frequency.

- The angular frequency ω, also called the temporal frequency, is equal to $\frac{2\pi}{T}$ and it is the angular displacement of the wave per unit of time.

- The phase velocity, c, of the wave is the velocity of the wave crests moving in space. The phase velocity is equal to the ratio of the temporal frequency to the spatial frequency: $c = \frac{\omega}{k}$.

The wave spectrum (or variance spectrum) $S(\omega)$ is a measure of the energy distributed over the different frequency components of the wave field. It can be expressed as a function of the wavenumber to give a wavenumber spectrum or as a function of the temporal frequency for the frequency spectrum. The two types of frequencies and spectra are related to each other by the linear dispersion relation given by:

$$\omega^2 = gk \, tanh(kh), \tag{5.1}$$

where g is gravitational acceleration equal to 9.807 $m.s^{-2}$ and h is the depth of the ocean of interest.

In this research, the focus was on the deep water ocean where the depth h is larger than a quarter of the wavelength, i.e. $kh >> 1$. This makes $tanh(kh) \approx 1$ and simplifies the dispersion relation to:

$$\omega^2 = gk. \tag{5.2}$$
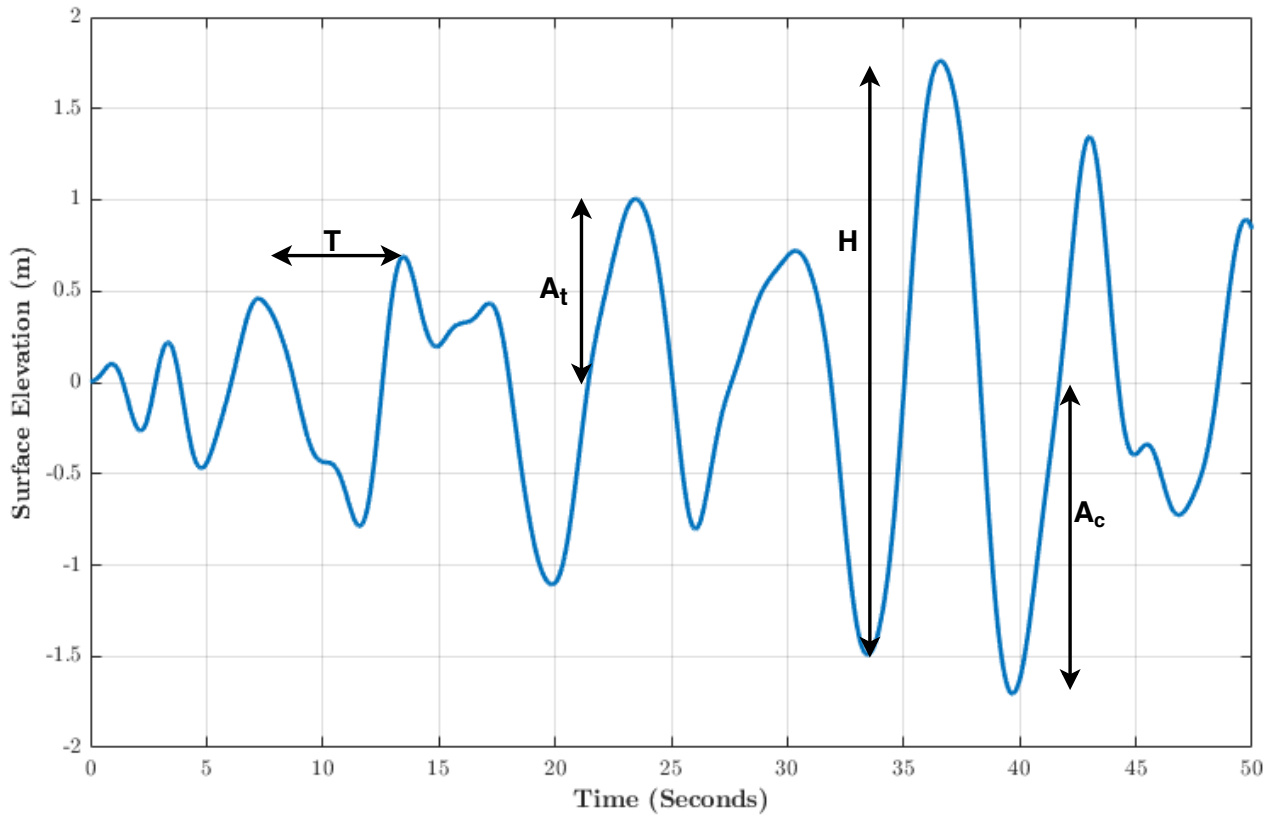
(a) Surface Elevation $\eta(t)$
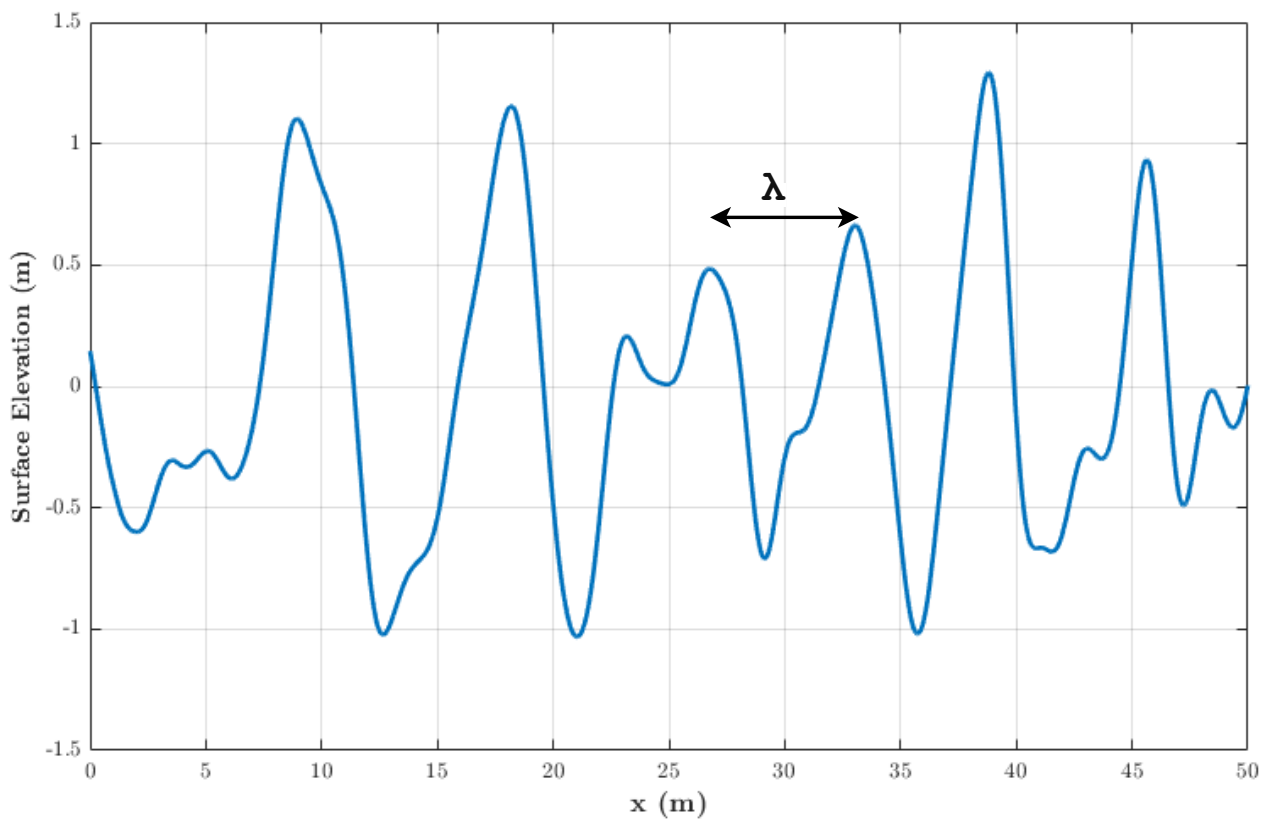
(b) Surface Elevation $\eta(x)$

Figure 5.1: An illustration of the different properties of the ocean waves.

Many wave spectra have been derived in the literature using the empirical method, i.e. recreating the mathematical expression from experimental and field measurements. The Pierson-Moskowitz spectrum and the JONSWAP spectrum are the most commonly mentioned spectra [63, 64, 65]. The Pierson-Moskowitz spectrum is related to a fully developed sea and is dependent on the wind speed. The fully developed sea is defined as the equilibrium stage that the ocean waves reach when the wind has blown long enough over a large area of the sea, and the phase speed of the waves is equal to the wind speed. The expression of the frequency Pierson-Moskowitz spectrum is:

$$S(\omega) = \alpha g^2 \omega^5 \exp\left[-\beta \left(\frac{g}{\omega U_{19.5}}\right)^4\right],$$ (5.3)

where α and β, both unitless constant parameters [66], were empirically derived as 8.1×10^{-3} and 0.74 respectively; ω is the frequency in rad/s; and $U_{19.5}$ is the wind speed in m/s at 19.5 m above the sea surface level [63]. The peak frequency of the spectrum is related to the wind speed by the expression [67]:

$$\omega_p = 0.877 \frac{g}{U_{19.5}}.$$ (5.4)

Rearranging equation 5.3 in terms of the peak frequency yields:

$$S(\omega) = \alpha g^2 \omega^5 \exp\left[-\frac{5}{4}\left(\frac{\omega}{\omega_p}\right)^{-4}\right].$$ (5.5)

The JONSWAP spectrum was developed from empirical data collected in 1973 in the North Sea [64]. It is an extension of the Pierson-Moskowitz spectrum that includes fetch-limited sea, i.e. sea that is not large enough to satisfy the conditions set by Pierson and Moskowitz for a fully developed sea. The JONSWAP frequency spectrum is [64]:

$$S(\omega) = \alpha g^2 \omega^5 \gamma^\delta \exp\left[-\frac{5}{4}\left(\frac{\omega}{\omega_p}\right)^{-4}\right],$$ (5.6)

with

$$\delta = \exp\left[-\frac{(\omega - \omega_p)^2}{2\sigma_0^2 \omega_p^2}\right],$$ (5.7)

where γ is the peak enhancement factor used to represent the wind-wave growth and equal to 3.3, σ_0 is the peak shape factor and equal to 0.07 for $\omega \leq \omega_p$ and equal to 0.09 for $\omega > \omega_p$, while α and ω_p are given, respectively, by:

$$\alpha = 0.076 \left(\frac{gX}{U_{19.5}^2}\right)^{-0.22},$$ (5.8)
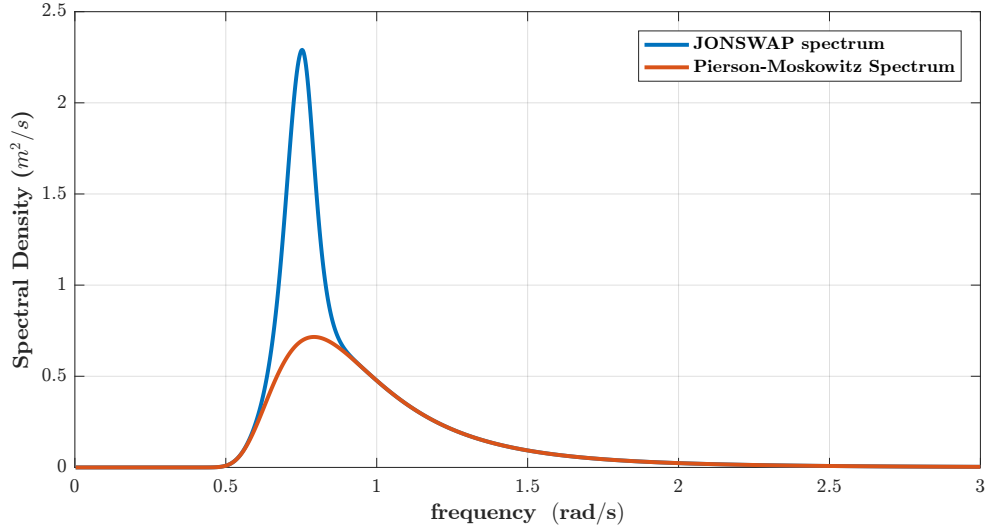
Figure 5.2: Plot of the Pierson-Moskowitz and JONSWAP spectra for a wind speed of $U_{10} = 10\ m/s$ and the fetch of 250 km for the JONSWAP spectrum. The JONSWAP spectrum has an enhancement at the peak frequency which is 0.75 rad/s.

and

$$\omega_p = 7\pi \left(\frac{g}{U_{19.5}} \right) \left(\frac{gX}{U_{19.5}^2} \right)^{-0.33}. \tag{5.9}$$

The parameter $\frac{gX}{U_{19.5}^2}$ is the non-dimensional fetch of the waves and X is the dimensional fetch in kilometers. Using either the approximation:

$$U_{19.5} = 1.075 \times U_{10}, \tag{5.10}$$

proposed in [68] or

$$U_{19.5} = 1.026 \times U_{10}, \tag{5.11}$$

proposed in [67], the two spectra and their parameters can be expressed in terms of U_{10}, which is the wind speed in m/s measured at 10 m above the sea surface. The first proposition is 1.0478 times the second proposition. We adopted the first approximation between U_{10} and $U_{19.5}$ for the calculations when it is required. Figure 5.2 shows the plot of the Pierson-Moskowitz and JONSWAP frequency spectra. These plots correspond to a fully developed sea at $U_{10} = 10\ m/s$. JONSWAP spectrum is in agreement with the Pierson-Moskowitz spectrum at lower and high frequency. However, there is a noticeable difference around the peak frequency, i.e. the reinforced peak of the JONSWAP spectrum. This stiffened peak is supported by the ongoing energy input from the wind to the wave field in the limited fetch region.

Besides the two wave spectra, other spectra had been proposed in the literature. The Donelan spectrum presented in [69] and the "Elfouhaily spectrum" proposed in [14] are some examples of the long list of other spectra used to examine, describe and model ocean waves. The Pierson-Moskowitz spectrum and the JONSWAP spectrum, described above, are used

for the investigation undertaken in this chapter because they constitute the building blocks of the rest of the wave spectra. Beyond that, they are omnidirectional spectra. They can be converted into directional spectra by means of the multiplication with a spreading function. Mathematically, the directional spectrum is obtained using the expression:

$$S(\omega, \theta) = S(\omega) \times D(\omega, \theta), \tag{5.12}$$

where $D(\omega, \theta)$ is the spreading function, and θ is the wave direction with respect to the wind direction. Similar to the case of the wave spectrum, different spreading functions can be found in the literature. In reality, the energy in the wave is not the same in every direction. The spreading function redistributes the total energy of the surface waves and ensures that this energy propagates in the direction of the winds. Therefore, it presumes very negligible energy propagates in a direction normal to the wind direction. Only the prominent spreading function is mentioned here as this chapter deals more with the omnidirectional spectrum. That is the cosine-power spreading function. It was first proposed in [70] and it is given in the form of:

$$D(\omega, \theta) = G(s) \cos^{2s}\left(\frac{\theta}{2}\right), \tag{5.13}$$

where s is the spreading parameter, and a function of the wave phase speed c and the wind speed U_{10}. $G(s)$ takes many forms but its primary purpose is to normalise the integral of $D(\omega, \theta)$ over the interval $[0, 2\pi]$ to 1. In [14] for instance, the spreading parameter s is given as:

$$s = 11.5\left(\frac{c}{U_{10}}\right)^{2.5}. \tag{5.14}$$

5.1.2 Probability Distribution of the Surface Wave Elevation

The surface elevation $\eta(\mathbf{x}, t)$ is a function of time t and position $\mathbf{x}$ (see Figure 5.1). Supposing that the surface waves are linear entities, the surface elevation can be expressed as a summation of cosine waves of random amplitudes with different frequencies and phases [65]:

$$\eta(\mathbf{x}, t) = \sum_{i=1}^{I} \sum_{j=1}^{J} a_{ij} \cos\left([k_i(x \cos \phi_j + y \sin \phi_j)] - \omega_i t + \theta_{ij}\right), \tag{5.15}$$

where k_i are the spatial frequencies (or wavenumbers), ϕ_j are the phase of the individual waves, ω is the angular frequency and θ_{ij} is the phase (assumed to be uniformly distributed between the interval $[-\pi, \pi]$). Carrying on with the linearity of the surface elevation and windowing the focus to a single point $\mathbf{x_0}$ in space, it can be presumed further that $\eta(\mathbf{x}, t)$ is a normally distributed random variable with zero mean ($\bar{\eta} = 0$) and a variance σ_η^2. This assumption is based on imperial observation [71].

Table 5.1: Computed values for the surface elevation variances with their corresponding wind speed U_{10} from the Pierson–Moskowitz spectrum (fully developed sea).

Wind Speed U_{10} (m/s)	Variances σ_η^2 (m^2)	RMS Height H_{rms} (m)
7.5	0.1252	1.009
10	0.3958	1.7794
12.5	0.9663	2.7803
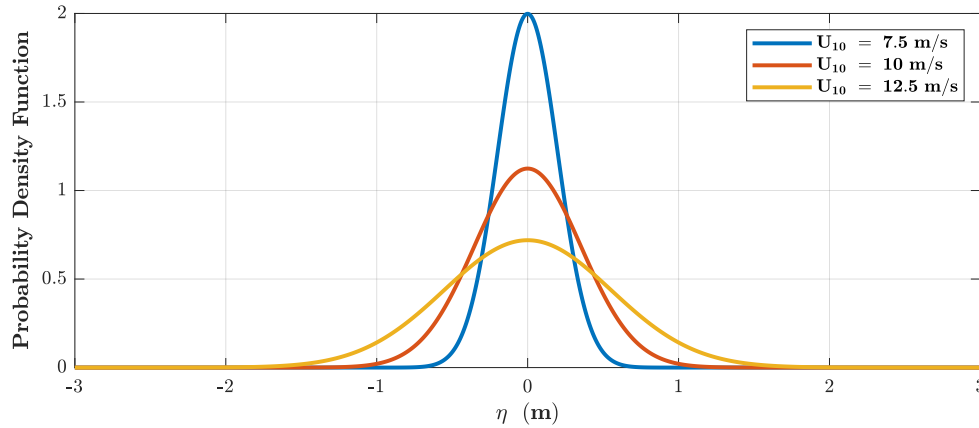
Figure 5.3: Plots of the probability density function of the ocean surface elevation for different wind speeds at 10 m above the mean surface level for fully developed sea.

Therefore, the probability density function of the surface elevation is [65]:

$$f(\eta) = \frac{1}{\sqrt{2\pi}\sigma_\eta} \exp\left[-\frac{\eta^2}{2\sigma_\eta^2}\right]. \tag{5.16}$$

The variance σ_η^2 of the surface elevation is related via Parseval's Theorem to the frequency wave spectrum [65]:

$$\sigma_\eta^2 = \int_{-\infty}^{\infty} \eta^2 f(\eta)d\eta = \frac{1}{\pi} \int_0^\infty S(\omega)d\omega. \tag{5.17}$$

Applying the equation (5.17) to the Pierson–Moskowitz spectrum for the three wind speeds at 10 m above the sea level and using the results, the probability density of the surface elevation was plotted for the three wind speeds. The wind speeds were 7.5, 10 and 12.5 m/s, the plots are shown in Figure 5.3, and the variance values are tabulated in Table 5.1. As expected the variance's value increases with the growing wind speed. This is explained by the increase in energy contained in the waves for larger wind speeds. The relationship between the variance and the wind speed is transferred to the probability density function plotted for the surface wind speed.

5.1.3 Probability Distribution of the Surface Wave Height

In some cases in physical oceanography and ocean engineering, researchers and engineers are more interested in the wave height rather than the surface elevation. This is because the wave height may reveal better the critical characteristics of the wave field. Examples of these cases
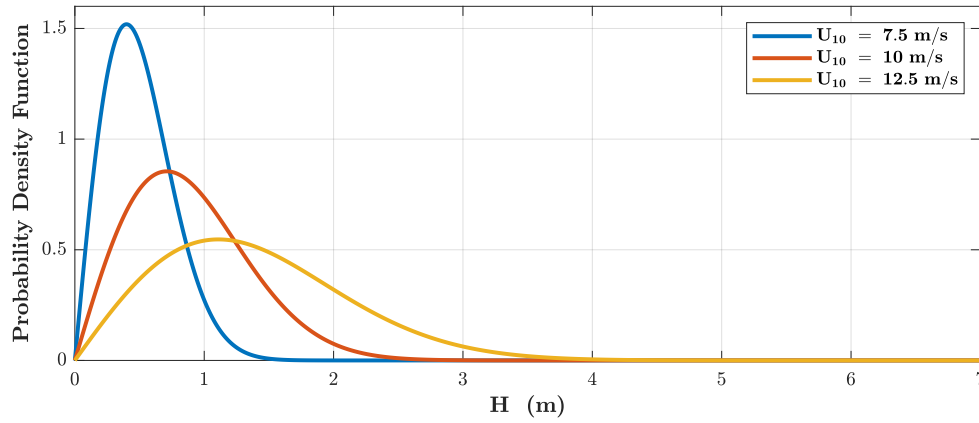
Figure 5.4: Plots of the probability density function of the wave height for different wind speeds at 10 m above the mean surface level (U_{10}) for fully developed sea using the Pierson–Moskowitz spectrum.

would be the design of coastal and offshore structures or the process of approximating the speed of self-propelling surface marine vehicle like the Wave Glider platform that converts wave energy into propulsion. Knowing the probability distribution of the wave height will play an essential role in the approximation of the probability of the LoS on the surface of the ocean as well as it does in wave energy extraction applications. The derivation of the mathematical expressions for the probability of the wave height is beyond the scope of this research.

Unlike the surface elevation which is a Gaussian process and using the same assumptions as in the previous section, the wave height has been shown in [72] to be a Rayleigh distributed random variable, and its probability density function (pdf) is given by [65]:

$$f_H(H) = \frac{2H}{H_{rms}^2} \exp\left[-\frac{H^2}{H_{rms}^2}\right], \tag{5.18}$$

where H is the individual wave height and H_{rms} is the root mean square (RMS) value of the wave height. The RMS value of the wave height is related to the variance σ_η^2 of the surface elevation by the expression:

$$H_{rms} = 2\sqrt{2}\sigma_\eta. \tag{5.19}$$

The work leading to the probability density of the wave height is detailed in [65]. Continuing from the variance values in Table 5.1, the RMS value of the wave height corresponding to each variance was computed as well, then used to obtain a graphical representation of the probability density function of the wave height that is Figure 5.4.

5.1.4 Probability Distribution of the Extreme Surface Height

This study paid close attention to define extreme waves as they are the most likely waves to block the transmissions of a radio wave from one transceiver to the others. Let H_e be an extreme wave height sampled out of N waves. The waves are either spatially distributed in

space or temporally distributed at a given location point $\mathbf{x}$ in space. As a consequence of the sampling of a random variable (wave height), H_e is also by itself a random variable. Focusing on a one-dimensional spatial distribution, the sample number N of waves considered for these plots was related to the distance D, covered by all the waves by:

$$N = \frac{D}{\lambda}, \tag{5.20}$$

where λ is the wave wavelength which was in turn extracted from the linear dispersion relation for deep sea (see equation (5.2)) and the peak wave frequency ω_p (see equation (5.4)). The expression for evaluating the wavelength is:

$$\lambda = \frac{2\pi U_{19.5}^2}{0.877^2 g}. \tag{5.21}$$

Letting $f_{H_e}(H_e)$ be the probability density function of the extreme wave height H_e over N waves, then it has been proven in section 4.3.4 of [65] that:

$$f_{H_e}(H_e) = N f_H(H_e) \left[F_H(H_e) \right]^{N-1}, \tag{5.22}$$

where $f_H(H_e)$ is the probability density function of the individual wave height, and $F_H(H_e)$ is the cumulative probability distribution of the individual wave height.

By definition, the cumulative probability distribution is the integral of the probability density functions, i.e.:

$$F_H(H_e) = \int_0^{H_e} f_H(h_e) dh_e. \tag{5.23}$$

Starting from the probability of the wave height given in (5.18), we have:

$$f_H(H_e) = \frac{2H_e}{H_{rms}^2} \exp \left[-\frac{H_e^2}{H_{rms}^2} \right], \tag{5.24}$$

and

$$F_H(H_e) = 1 - \exp \left[-\frac{H_e^2}{H_{rms}^2} \right]. \tag{5.25}$$

Substituting (5.24) and (5.25) into (5.22) gives:

$$f_{H_e}(H_e) = N \frac{2H_e}{H_{rms}^2} \exp \left[-\frac{H_e^2}{H_{rms}^2} \right] \left[1 - \exp \left[-\frac{H_e^2}{H_{rms}^2} \right] \right]^{N-1}. \tag{5.26}$$

In a similar fashion as the two previous cases, this probability density function was plotted for the same three wind speeds and their corresponding RMS values for the wave height. These plots are in Figure 5.5. The distance used in the plots was 5 km.

Furthermore, the probability density of the extreme height were plot in Figure 5.6 for different distances D. These distances were 0.1, 1, 5 and 10 km. At wind speed of $U_{10} = 10 m/s$, the wavelength λ is approximatively 96 m. Therefore, the aforementioned distances
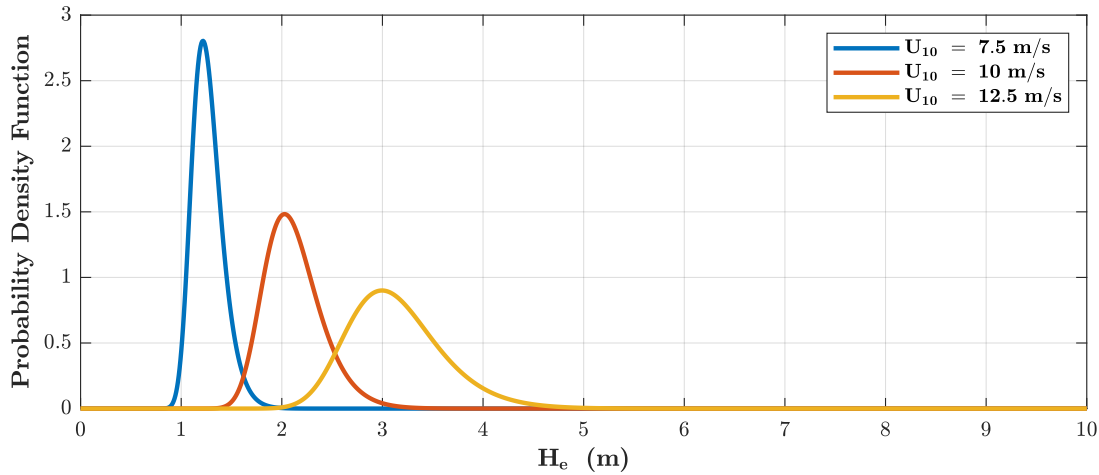
Figure 5.5: Plots of the probability density function of extreme wave heights for different RMS values of wave height tabulated in Table 5.1 for different wind speed U_{10} and over a distance of 5 km.

corresponds to 1, 10, 50 and 10 wavelengths respectively. As the distance D increases, the effect of bigger wave heights on the probability density function of extreme wave heights are dominant. The increase of the wind speed and the increase of the distance have similar results as it is seen in Figure 5.5 and Figure 5.6.

5.2 Related Work on the Probability of the LoS

The communication of LoS is preferred in contexts where losses due to penetration and diffraction are significant. This is generally the case for millimeter waves that are mostly employed in the LoS communication. The communication channels built around the presence of a LoS may become imperative in locations where the medium is very lossy for sub-gigahertz radio transmission. The seawater at 868 MHz qualifies as a substantial impediment to a radio wave carrier, therefore triggering the absolute necessity of communication using LoS. It is indispensable to have an estimation of the probability of the LoS, i.e. an approximation of the likelihood that there is no single obstacle between the two points of interest in the communication, to achieve robust and reliable transmission. In the literature, three techniques are mainly used in the calculation of the probability of the LoS. These are:

- Empirical method: This technique is defined around collecting real-world measurements and fitting a curve to the measurements. This method is straightforward and precise, but cannot be applied to environments with different conditions to the set-up in which the data were collected in the first place.

- Deterministic method: This method uses electromagnetic first principles along with the prior knowledge of the terrain to determine the communication channel and its gain. This method requires a clear understanding of the physical environment; it becomes
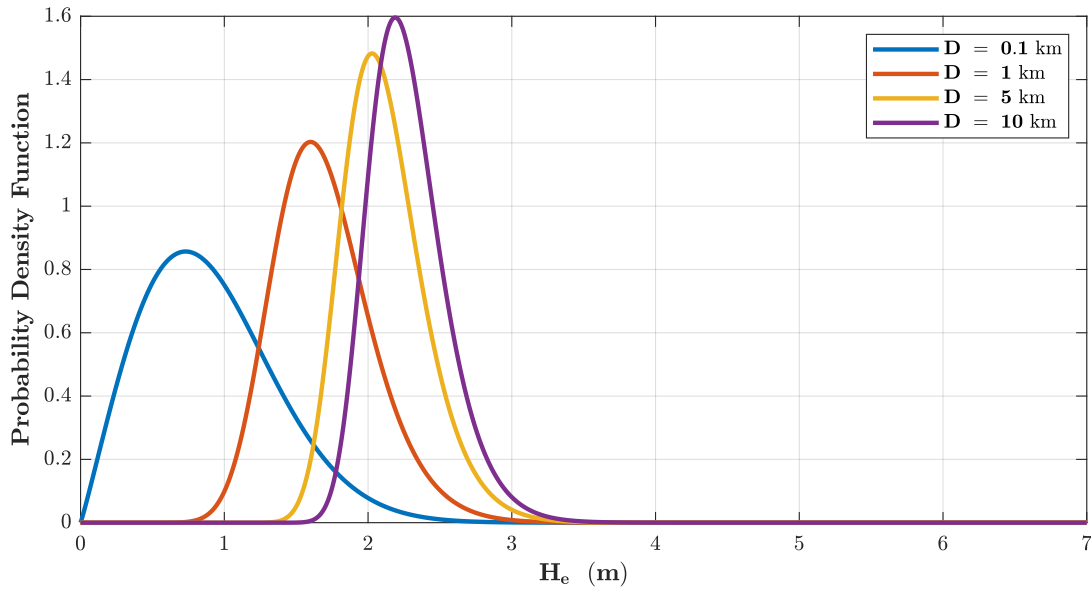
Figure 5.6: Plots of the probability density function of extreme wave heights over four different distances D. The wind speed is $U_{10} = 10 \, m/s$.

irrelevant and infeasible when the physical conditions, i.e. the position or the size of the impediments change in the terrain.

- Stochastic method: This technique extracts acceptable analytical expressions of the probability of the LoS by considering the conditions in the environment as a set of random variables that have known moments or at least these moments can be evaluated with assurance.

Amongst these three methods, the last one is widely used. In [73], the authors analysed and proposed an estimate for the probability of the LoS for millimeter waves using the stochastic methods in a 3D environment. Their estimation depended on the carrier frequency of the channel and agreed with the work completed in [74] when it comes to the 2D approximation. These papers both dealt with an urban environment where the buildings and structures are assumed to be fixed in position and size and modelled to be the Homogeneous Poisson Point Process (HPPP). The deterministic method could also be applied to their physical settings provided that the terrain was studied ahead of the analysis.

5.3 The Probability of the LoS

This section presents the approach applied to determine the probability of the LoS. It starts by investigating the background and the problem statement first and then considering the two-dimensional geometry set-up of the problem. The section continues with the definition and the approximation of the relevant random variables and finishes with the materialisation of the probability of the LoS.

5.3.1 Background and Problem Statement

Consider two flat surface marine vehicles, floating on the surface of the ocean separated by some distance, that are required to collaborate, i.e. to share information using radio frequency transmission at a local level; they could both be Wave Glider platforms or two different types of vehicles. The surface elevation of the ocean is a random quantity with properties that affect radio frequency transmission. This was discussed in the previous chapter. Besides the electromagnetic properties of the ocean surface, the relatively small height of surface vehicles, like that of the Wave Glider platforms make it difficult to achieve a reliable radio channel between the two vehicles over large distances. It is suggested that the information should be shared from one vehicle to the other when there is a clear and direct LoS between the two surface vehicles. This suggestion makes sure that the information is successfully transmitted to the other end and the power lost due to communication is minimised. Nevertheless, four scenarios arise where there is an obstacle blocking the LoS. These scenarios are:

Scenario 1: The whole body of a surface vehicle is at the trough of a big wave.

Scenario 2: The two surface vehicles are on top of the local crests, but there is a large wave in between them.

Scenario 3: The two surface vehicles are on a steep wave and the consequence, their antennas are at an inclined angle regarding the vertical, changing polarisation of the radio wave.

Scenario 4: The distance between the two surface vehicles is large enough to consider the Earth's curvature as the prominent factor blocking the LoS.

For all these scenarios, it was assumed that both surface vehicles have sufficient transmission power to cover the distance separating the vehicles. One solution that comes to mind could be used to establish a LoS almost all the time when information is being transmitted. This solution would be to navigate the vehicles in unison to the top of the largest local wave that would ensure the presence of the LoS. This solution requires real-time information of the wave field in the region surrounding both vehicles and a real-time navigation system to control the vehicles to the desired position for transmission. This solution is not practical for a few reasons considering the case of the Wave Glider platform. The most prominent one being the lack of wave field state information in the region where the platforms are used. This solution will be investigated in the next chapter.

In this chapter, one solution is preferred. This solution uses the information available, or that could be easily acquired to approximate, at any given time, the likelihood of the presence of a LoS between the two points of interest on the surface of the ocean. It is called the probability of the LoS (P_{LoS}) and its approximation was derived from the physical quantities such as the average wind speed in the region of interest, the instantaneous surface elevation at the locations of the vehicles and the distance between the two vehicles.
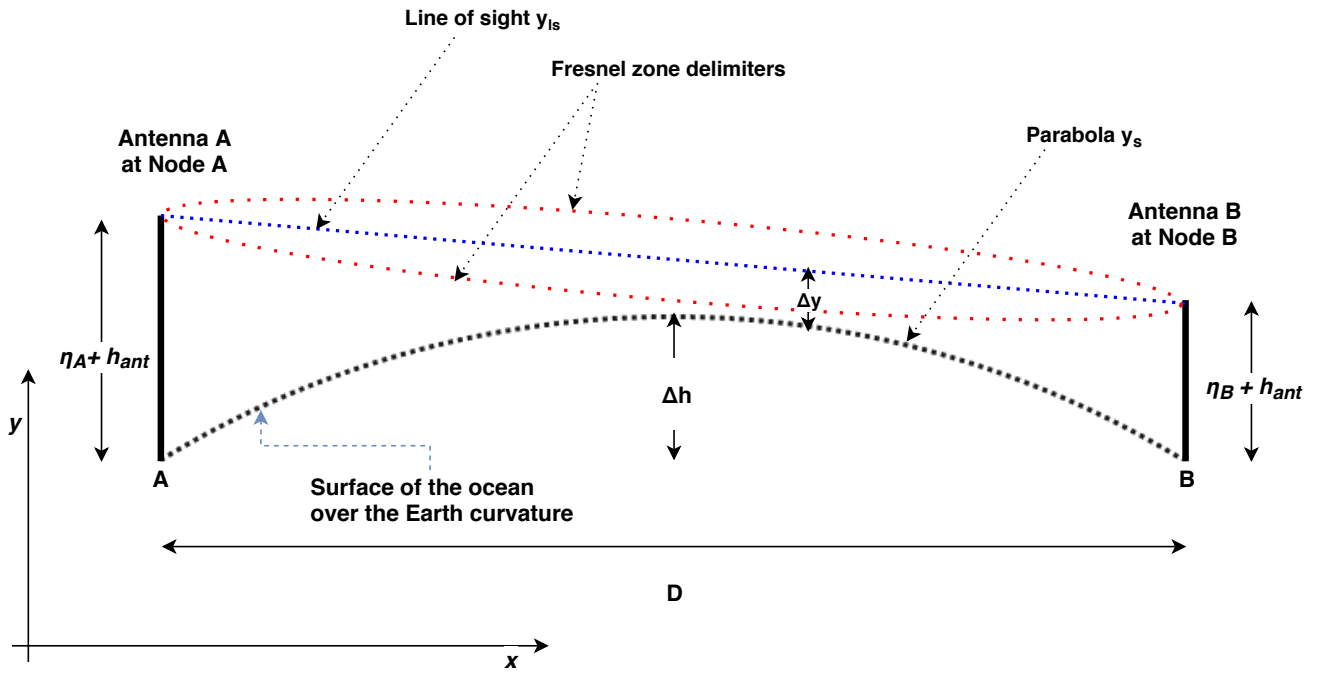
Figure 5.7: Geometrical representation of the probability of the LoS studied in this chapter. The surface elevation at location A and B are highlighted respectively by η_A and η_B. The Earth's curvature (dotted dark line) and the Fresnel zone (dotted red line) are also represented.

5.3.2 Geometrical Representation of the Problem

Figure 5.7 gives the geometrical representation of the problem studied in this chapter. This representation is very similar to the one in Figure 4.2, except here the ocean surface elevation is included. At location A and B, the surface elevations are called η_A and η_B respectively. For simplicity, both antennas are assumed to have the same height h_{ant}. The height Δh is the effect of the Earth's curvature over the distance D separating the two antennas.

The geometrical representation also shows the direct LoS line joining the two antennas (dotted blue line) as well as a sketch of the Fresnel zone (dotted red line), which is also a measure of the LoS.

For reasons that will become clear later, we define y_A and y_B as:

$$y_A = \eta_A + h_{ant}, \tag{5.27a}$$
$$y_B = \eta_B + h_{ant}. \tag{5.27b}$$

5.3.3 Approximation of the Parameters and Random Variables

The height Δh as a result of the Earth's curvature has already been approximated in the previous chapter in (4.6). Shifting the focus to the surface of the ocean, the two-dimensional mean water level over a relatively small distance D (order of a few kilometers), and as represented in

Figure 4.2 and 5.7, can be approximated by a *parabola* characterised by:

$$y_s = -\frac{4\Delta h}{D^2}x^2 + \Delta h, \tag{5.28}$$

in a vertical (x, y) Cartesian coordinate system where x is along the distance D (see Figure 5.7). The origin of the Cartesian coordinate system is the centre of the segment joining A and B.

Similarly, and still in the same Cartesian coordinate system, the LoS, i.e. the line joining the top of the two antennas is modelled as an affine equation:

$$y_{ls} = \frac{y_A - y_B}{D}x + \frac{y_A + y_B}{2}. \tag{5.29}$$

The vertical distance between the surface of the ocean y_s and the LoS y_{ls} is:

$$\Delta y = y_{ls} - y_s, \tag{5.30a}$$

$$\Delta y = \frac{y_A - y_B}{D}x + \frac{y_A + y_B}{2} + \frac{4\Delta h}{D^2}x^2 - \Delta h. \tag{5.30b}$$

Consider the point called x_{ymin} and defined as the point where the vertical distance Δy is a minimum along the segment sustained by A and B. There is a higher likelihood that the waves around the point x_{ymin} will block the LoS between two nodes at points A and B as the surface is much closer to the line (blue dotted line in Figure 5.7). Thus, the attention can be shifted to the waves around this point, x_{ymin}, in the evaluation of the probability of the LoS. Letting Δy_{min} be this minimum mean distance, it is obtained as a function g of y_A, y_B and Δh:

$$\Delta y_{min} = g(y_A, y_B, \Delta h), \tag{5.31a}$$

$$\Delta y_{min} = -\frac{(y_A - y_B)^2}{16\Delta h} + \frac{y_A + y_B}{2} - \Delta h. \tag{5.31b}$$

ranging over $\mathbb{R}$. This expression for the minimum mean vertical distance between the ocean surface of the line joining the two antennas and going through the centre of the Fresnel zone will be used to formulate the probability of the LoS.

5.3.4 Formulation of the Probability of the LoS

Assuming that the amplitude of the highest waves around the point x_{ymin} is A_e, there is a direct LoS between the antennas at points A and B provided that A_e is less than Δy_{min}, i.e.:

$$A_e - \Delta y_{min} < 0. \tag{5.32}$$

The probability of the LoS, P_{LoS}, is then obtained by computing:

$$P_{LoS} = P(A_e - \Delta y_{min} < 0) \quad \text{or} \quad P_{LoS} = P(A_e < \Delta y_{min}). \tag{5.33}$$

To be able to compute this probability, the joint pdf of the random variables Δy_{min} and A_e must first be acquired.

a) Probability Density Function of Δy_{min}

It has been shown that the variable Δy_{min} is a function of the surface elevation at both locations A and B, the height of the antenna used, and the Earth's curvature. y_A and y_B are a normally distributed random variable with zero mean and variance σ_η; the last two, the height of the antenna used, and the Earth's curvature, are considered as constants at this point. It is evident that Δy_{min} is also a normally distributed random variable and therefore its Gaussian probability density function can be obtained. The Taylor series approximation presented in [75] was used to derive the expectations (means) and variances of y_A, y_B and Δy_{min} respectively. The distance D separating the two locations is large enough to infer that y_A, y_B are independent random variables. A distance varying from 5 km to 10 km will be considered. Starting with y_A, its expectation and variance are:

$$\bar{y}_A = \mathbb{E} < y_A >= \mathbb{E} < \eta_A > +h_{ant}, \tag{5.34a}$$
$$\bar{y}_A = h_{ant}, \tag{5.34b}$$

$$Var\{y_A\} = Var\{\eta_A + h_{ant}\}, \tag{5.35a}$$
$$Var\{y_A\} = \sigma_{\eta_A}^2, \tag{5.35b}$$

where $\mathbb{E} < \cdot >$ and $Var\{\cdot\}$ are the expectation and the variance operators respectively. Similarly,

$$\bar{y}_B = \mathbb{E} < y_B >= \mathbb{E} < \eta_B > +h_{ant}, \tag{5.36a}$$
$$\bar{y}_B = h_{ant}, \tag{5.36b}$$

$$Var\{y_B\} = Var\{\eta_A + h_{ant}\}, \tag{5.37a}$$
$$Var\{y_B\} = \sigma_{\eta_B}^2. \tag{5.37b}$$

Finally, the expectation and variance of Δy_{min} from (5.31) give:

$$\overline{\Delta y}_{min} = \mathbb{E} < \Delta y_{min} >= g(\bar{y}_A, \bar{y}_B), \tag{5.38a}$$
$$\overline{\Delta y}_{min} = h_{ant} - \Delta h, \tag{5.38b}$$

$$Var\{\Delta y_{min}\} = Var\{\eta_A\} \left(\frac{\partial g(\bar{y}_A, \bar{y}_B)}{\partial y_A}\right)^2 + Var\{\eta_B\} \left(\frac{\partial g(\bar{y}_A, \bar{y}_B)}{\partial y_B}\right)^2, \tag{5.39a}$$

$$Var\{\Delta y_{min}\} = \frac{1}{4}\sigma_{\eta_A}^2 + \frac{1}{4}\sigma_{\eta_B}^2. \tag{5.39b}$$

Presuming that σ_{η_A} and σ_{η_B} are equal in value to each other and equal to σ_η, the variance of Δy_{min} is:

$$Var\{\Delta y_{min}\} = \frac{1}{2}\sigma_\eta^2. \tag{5.40}$$

The probability density function of Δy_{min} was obtained as:

$$f(\Delta y_{min}) = \frac{\sqrt{2}}{\sqrt{2\pi}\sigma_\eta h_{ant}} \exp\left[-\frac{1}{2}\frac{(\Delta y_{min} - h_{ant} + \Delta h)^2}{(\frac{1}{\sqrt{2}}\sigma_\eta)^2}\right]. \tag{5.41}$$

b) Probability Density Function of A_e

The amplitude of a wave is given by the half of its height. Drawn from this definition, A_e is half of the extreme wave height H_e, i.e.:

$$A_e = \frac{H_e}{2}, \tag{5.42}$$

with wave extreme amplitude A_e being a positive quantity. The probability density function of the extreme amplitude was derived by applying the variable transformation to the probability density function of the extreme wave height H_e. The variable transformation stipulates that:

$$\text{if } \beta = h(\alpha), \quad \text{then} \tag{5.43a}$$

$$f(\beta) = f[h(\alpha)] \left|\frac{dh(\alpha)}{d\alpha}\right|. \tag{5.43b}$$

The probability density function of the extreme wave amplitude A_e was obtained as:

$$f(A_e) = 8N\frac{A_e}{H_{rms}} \exp\left[-\left(\frac{2A_e}{H_{rms}}\right)^2\right] \left[1 - \exp\left[-\left(\frac{2A_e}{H_{rms}}\right)^2\right]\right]^{N-1}. \tag{5.44}$$

As this pdf only depends on the parameters that had been computed in Table 5.1, its plot is shown in Figure 5.8. This plot is very similar to the one of the extreme wave height in shape for all the wind speeds. However, the difference that must be noticed is the shift to the left in Figure 5.8 showing clearly the relation between the two random variables.

c) Joint Probability Density Function of A_e and Δy_{min}

The conspicuous independence between the two random variables permits one to say that the joint probability of A_e and Δy_{min} was the product of their respective individual probability
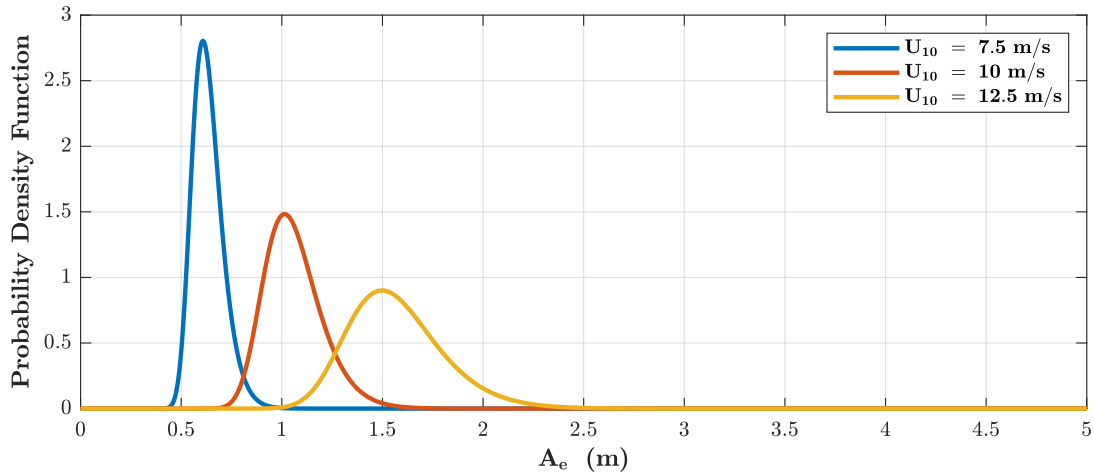
Figure 5.8: Plots of the probability density function of the extreme wave amplitude for different RMS values of wave height tabulated in Table 5.1 for different wind speed U_{10} and over a distance of 5 km. Notice that the amplitudes corresponding to the highest pdf are half of the values in Figure 5.5 for the different wind speed.

density functions. This meant that:

$$f(A_e, \Delta y_{min}) = f(A_e) \times f(\Delta y_{min}). \tag{5.45}$$

d) Probability of the LoS

The calculation steps involved in the derivation of the actual probability of the LoS were:

$$P_{LoS}(\cdot) = P(A_e < \Delta y_{min}), \tag{5.46}$$

with $(\cdot)$ meaning that the probability of the LoS can be evaluated as a function of one or more random variables that relates directly to the physical environment of the ocean surface or the communication system. For instance, the probability of the LoS could be computed as a function of the wind speed or the distance separating the two platforms (transceiver nodes). Using the joint probability density function of A_e and Δy_{min}, this probability could be written as:

$$P_{LoS}(\cdot) = \int_{-\infty}^{+\infty} \int_0^{\Delta y_{min}} f(A_e, \Delta y_{min}) \ dA_e \ d\Delta y_{min}, \tag{5.47a}$$

$$P_{LoS}(\cdot) = \int_{-\infty}^{+\infty} \int_0^{\Delta y_{min}} f(A_e) \times f(\Delta y_{min}) \ dA_e \ d\Delta y_{min}. \tag{5.47b}$$

Substituting $f(A_e)$ and $f(\Delta y_{min})$ by their respective expressions yielded:

$$P_{LoS}(\cdot) = \int_{-\infty}^{+\infty} \int_0^{\Delta y_{min}} \frac{\sqrt{2}}{\sqrt{2\pi}\sigma_\eta h_{ant}} \exp\left[-\frac{1}{2}\frac{(\Delta y_{min} - h_{ant} + \Delta h)^2}{(\frac{1}{\sqrt{2}}\sigma_\eta)^2}\right],$$

$$8N\frac{A_e}{H_{rms}}\exp\left[-\left(\frac{2A_e}{H_{rms}}\right)^2\right]\left[1 - \exp\left[-\left(\frac{2A_e}{H_{rms}}\right)^2\right]\right]^{N-1} dA_e \, d\Delta y_{min}. \tag{5.48}$$

Rearranging and evaluating the inner integral gave the following:

$$P_{LoS}(\cdot) = \int_{-\infty}^{+\infty} \frac{\sqrt{2}}{\sqrt{2\pi}\sigma_\eta h_{ant}} \exp\left[-\frac{1}{2}\frac{(\Delta y_{min} - h_{ant} + \Delta h)^2}{(\frac{1}{\sqrt{2}}\sigma_\eta)^2}\right]$$

$$\int_0^{\Delta y_{min}} 8N\frac{A_e}{H_{rms}}\exp\left[-\left(\frac{2A_e}{H_{rms}}\right)^2\right]\left[1 - \exp\left[-\left(\frac{2A_e}{H_{rms}}\right)^2\right]\right]^{N-1} dA_e \, d\Delta y_{min}, \tag{5.49}$$

$$P_{LoS}(\cdot) = \int_{-\infty}^{+\infty} \frac{\sqrt{2}}{\sqrt{2\pi}\sigma_\eta h_{ant}} \exp\left[-\frac{1}{2}\frac{(\Delta y_{min} - h_{ant} + \Delta h)^2}{(\frac{1}{\sqrt{2}}\sigma_\eta)^2}\right]$$

$$\left[1 - \exp\left[-\left(\frac{2\Delta y_{min}}{H_{rms}}\right)^2\right]\right]^N d\Delta y_{min}, \tag{5.50}$$

$$P_{LoS}(\cdot) = \int_{-\infty}^{+\infty} \frac{1}{\sqrt{\pi}\sigma_\eta h_{ant}} \exp\left[-\frac{(\Delta y_{min} - h_{ant} + \Delta h)^2}{(\sigma_\eta)^2}\right]$$

$$\left[1 - \exp\left[-\left(\frac{2\Delta y_{min}}{H_{rms}}\right)^2\right]\right]^N d\Delta y_{min}. \tag{5.51}$$

The evaluation of this probability required further effort as it looked sophisticated and long. A few numerical methods were investigated in the attempt to evaluate this probability of the LoS, but only one of them piqued the interest in this context because it agrees with the format of the expression of the probability of the LoS and is applicable in the probability and statistical studies. This numerical scheme is introduced next, followed by an explanation of how it was used to evaluate this probability numerically.

5.4 Numerical Evaluation of the Probability of the LoS

The numerical method proposed here to evaluate the probability in equation (5.51) numerically is the Gauss-Hermite quadrature. This is used in many fields such as Statistics and Finance [76] to mention a few. The Gauss-Hermite quadrature is a type of Gaussian quadrature used to

evaluate or estimate an integral in the form of (5.52) numerically.

$$\int_{-\infty}^{+\infty} \Phi(x) \exp\left[-x^2\right] dx. \tag{5.52}$$

This quadrature approximates the integral above using the numerical scheme characterised by the summation:

$$\int_{-\infty}^{+\infty} \Phi(x) \exp\left[-x^2\right] dx = \sum_{i=1}^{m} w_i \Phi(x_i). \tag{5.53}$$

where x_i are the roots of the mth order Hermite polynomial and w_i are the corresponding weights. The calculation of the parameters x_i, w_i as well as the Hermite polynomial are beyond the focus of this work; however, these parameters are calculated and tabulated in [77, 78] for $m = 64, 96, 128$.

Often, as it is the case here, the integral to be evaluated may not be in the form expressed in equation (5.52) because the exponential term of the integrand is predominantly not merely a function of $-x^2$. It is, therefore, required to have some variable manipulation to get the integral of interest in the proper form so that the Gauss-Hermite quadrature approximation could be applied. Fortunately, the integrands are made in such a way that a simple variable change is sufficient to get to the integral in equation (5.52). The variable change was exerted as follows.

Creating a new variable ζ and letting it be:

$$\zeta = \frac{\Delta y_{min} - h_{ant} + \Delta h}{\sigma_\eta}. \tag{5.54}$$

This is equivalent to:

$$\Delta y_{min} = \sigma_\eta \zeta + h_{ant} - \Delta h. \tag{5.55}$$

Using the above relationship and the principle introduced in (5.43b), the mathematical expression of the probability of the LoS in (5.51) was rewritten into the required form for the implementation of the Gauss-Hermite quadrature as:

$$P_{LoS}(\cdot) = \int_{-\infty}^{+\infty} \frac{1}{\sqrt{\pi}} \exp\left[-\zeta^2\right]$$
$$\left[1 - \exp\left[-\left(\frac{2(\sigma_\eta \zeta + h_{ant} - \Delta h)}{H_{rms}}\right)^2\right]\right]^N d\zeta. \tag{5.56}$$

The function $\Phi(\zeta)$ can clearly be read off as:

$$\Phi(\zeta) = \left[1 - \exp\left[-\left(\frac{2(\sigma_\eta \zeta + h_{ant} - \Delta h)}{H_{rms}}\right)^2\right]\right]^N. \tag{5.57}$$

The probability of the LoS can be numerically calculated using equation (5.56) or (5.57) and (5.53). The expression of the probability of the LoS provided by equation (5.56) is dependent on the parameters such as the variance (or the standard deviation) of the surface elevation of the
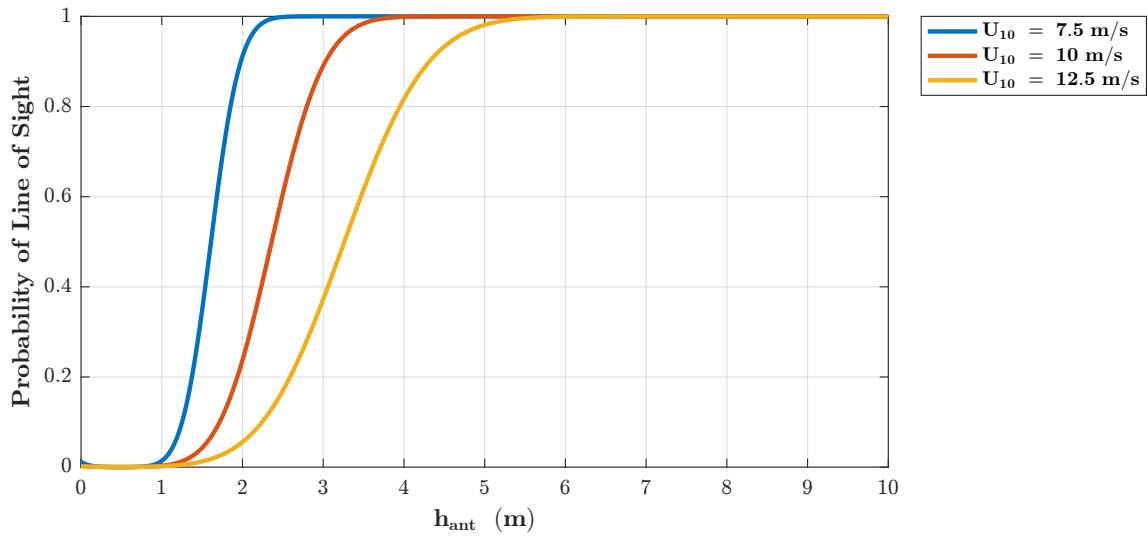
Figure 5.9: probability of the LoS as a function of the antenna height h_{ant} for different wind speeds at 10 m above the mean surface level for fully developed sea using the Pierson–Moskowitz spectrum. The nodes are 5 km apart.

ocean, the RMS value of the wave height, the distance separating the two transceiver nodes, the height of the antenna, and by induction the wind speed. Thus, equation (5.56) could be used to compile the probability of the LoS as a function of either one of these mentioned parameters (or random variables) while fixing the values of the rest. Alternatively, it could be used to compute the joint probability of any number of these random variables and dependences. The actual calculation of the probability of the LoS is the focus of the next section of this chapter. The calculations are accomplished for different random variable parameters.

5.5 Simulations and Validation of the Probability of the LoS

Before the probability of the LoS developed above could be used, it must be proven to have the properties of a probability function. In other words, the probability of the LoS $P_{LoS}(\cdot)$ must be bounded and monotonic in the interval $[0, 1]$ for any random variables. In this section, the value of $P_{LoS}(\cdot)$ will be calculated and plotted for the different random variables in the attempt to confirm that it is an actual probability function. A Matlab™ script was created to accomplish this task.

5.5.1 Evaluation of the Probability of the LoS for the Antenna Height

Starting with the antenna height h_{ant} as the random variable and fixing the distance D between the two nodes to 5 km, the probability of the LoS was computed for three values of wind speed U_{10}. These values are 7.5, 10 and 12.5 m/s. The result is plotted in Figure 5.9.

This result shows firstly that the expression derived is, in fact, a probability function, its values are positive and increasing to a maximum value of 1 with respect to the random variable h_{ant}. The plot is also monotonic. Secondly, the effect of the wind speed is noticeable;
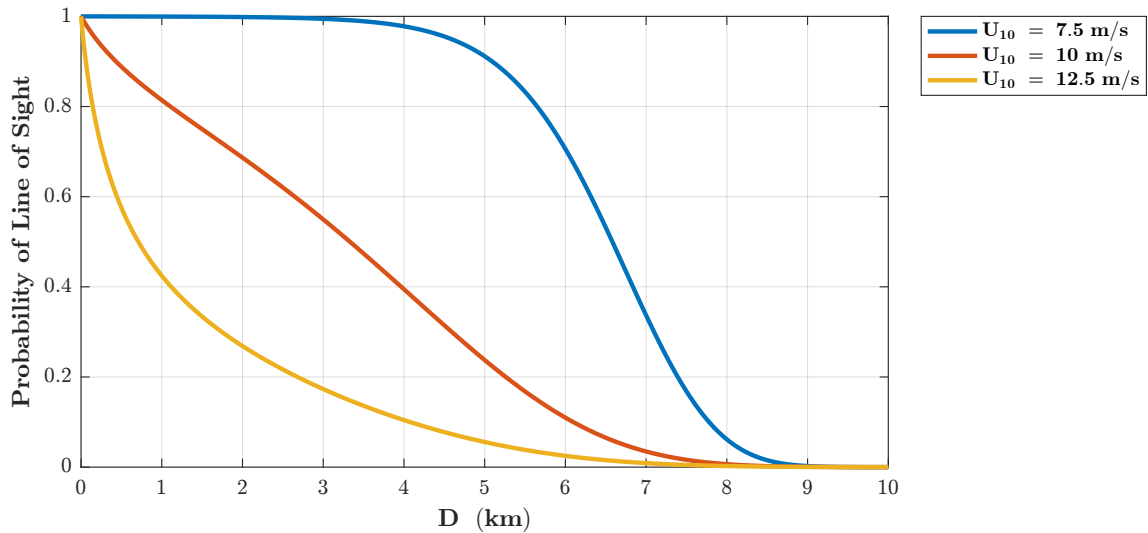
Figure 5.10: probability of the LoS as a function of the distance D for different wind speeds at 10 m above the mean surface level for fully developed sea using the Pierson–Moskowitz spectrum. The antenna height is 2 m.

the probability of the LoS decreases with increasing value of the wind speed U_{10}. This is expected as higher wind speeds translate to bigger waves in a fully developed sea. Also, the probability remains zero for $h_{ant} \leq 1$ m, this justifies the impact of the earth curvature on the probability of the LoS. The "1 m" here corresponds to the Δh and indicates that the total antenna height must be larger than the Δh for successful initiation of the LoS between the two nodes.

5.5.2 Evaluation of the Probability of the LoS for the Distance

To fully comprehend the impact of the distance separating the two points A and B on the LoS, the probability of the LoS was also compiled as a function of this distance. The value of h_{ant} was fixed to 2 m as this was the case in the previous chapter's simulation. Similarly, the wind speed was fixed at 7.5, 10, 12.5 m/s. The results are illustrated in Figure 5.10. Although typical applications will be limited to the distance around 10 km, a vast range of distances was used to compile the results in Figure 5.10 to show the global behaviour of the probability of LoS looking from the distance perspective.

They agreed with the previous ones in Figure 5.9 in the context of the impact of the wind speed. Also, these results show that the probability is decreasing as the distance increases. The decline of the probability of the LoS can be explained by the rise of the impact of the Earth's curvature expressed by the parameter Δh. This assessment is valid for relatively small distances, i.e. a distance up to the 10 km mark.
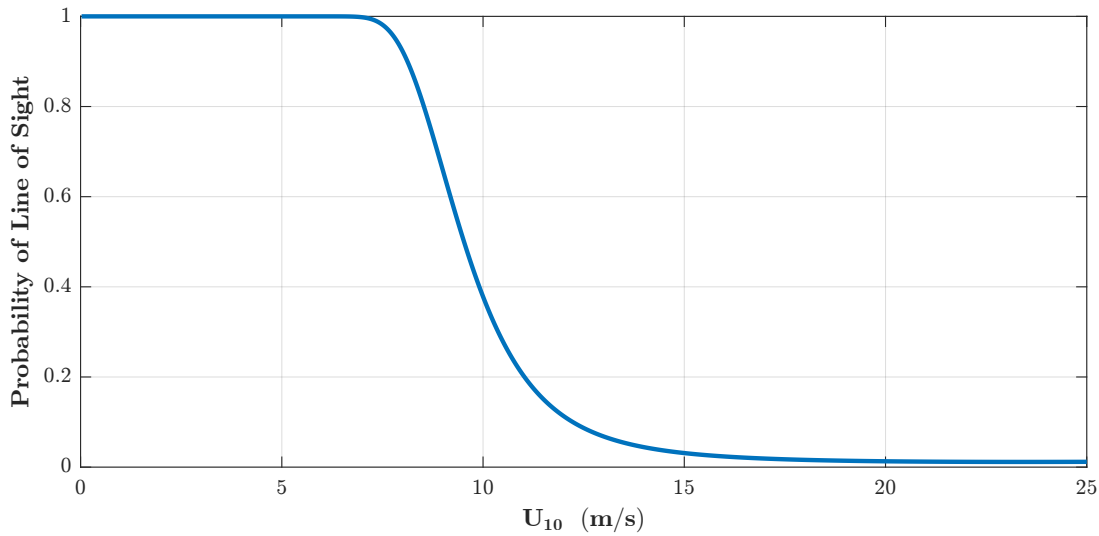
Figure 5.11: probability of the LoS over 5 km as a function of the wind speed U_{10} for fully developed sea using the Pierson–Moskowitz spectrum. Antenna height is 2 m.

5.5.3 Evaluation of the Probability of the LoS for the Wind Speed

For completeness, the probability of the LoS was computed as a function of the wind speed U_{10}. The range of the wind speeds was considered for very calm seas with $U_{10} \leq 5$ m/s to stormy seas where U_{10} is around 25 m/s. The antenna height was kept at 2 m and the distance D at 5 km. The results are presented in Figure 5.11.

This effect of the wind speed on the probability of the LoS is in agreement with the previously displayed results. The probability is very high for wind speeds ranging from 0 to 6 m/s and starts decreasing for wind speeds larger than 6 m/s. The rate of change of the probability is significant for the wind speed in the interval 6 to 15 m/s and becomes small when the wind speed reaches 15 m/s. The probability remains small at high wind speed.

5.6 Experimental Results

In this section, we looked at the results of the second experiment over the ocean from the perspective of the probability of the LoS. During this experiment, the number of packets dropped and the total number of packets transmitted were catalogued. Assuming that the probability of a packet being received is directly equal to the probability of the LoS because of the reliability of the LoRa channel, the probability of the LoS could be evaluated numerically for each of the antenna heights. The probability was expected to improve with the total antenna height rising. However, there were some inconsistencies in the error rate observed from the experiment. An external factor caused the inconsistency in the experiment. The experiment was conducted in an environment where all the details could not be controlled. The geographical position of the slave node was a site with boat activities, and the movement of the boats could not be anticipated. As a result, the packet drop rate, i.e. the error rate, was influenced by not only the ocean surface waves but also the blockages and the wakes
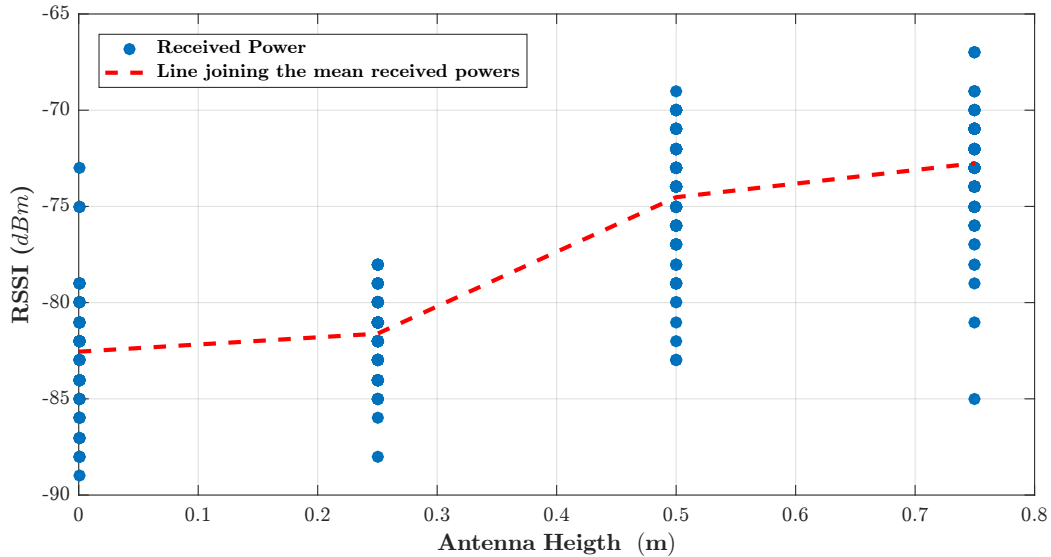
Figure 5.12: Scatter plot of the received power concerning the height between the antenna and the mean water level. The curve joining the average point of the received power is also shown.

of the surface seawater perpetuated by the boats. The recorded error rates were, hence, not conclusive in regard to the probability of the LoS.

The behaviour of the received power does provide some further insights into the footprint of the total antenna height on the probability of the LoS. The scatter plots of the received power concerning the height from the mean water level to the lower end of the antenna are given in Figure 5.12. The line fitting (in red dashes) shows the trends of the received power level. It concurs with the simulation results in Figure 5.9 where it was noticed that an increase in the antenna height enhances the likelihood of the signals being received at the receiver node. Even though more experimental data are required to make conclusive deductions, it can be partially inferred from these results that the general tendency of the received power level is expected to improve from a low level at small antenna height to fixed power level for large antenna heights.

Moreover, a Monte Carlo simulation was conducted to evaluate the probability of the LoS from the statistical characteristics of surface elevations at the two nodes and all the N wave amplitudes along the distance D. In the Monte Carlo simulation, the wave heights and amplitudes were simulated along the line joining the two nodes, A and B; and the presence of the LoS was associated with the condition in (5.58) being true for every single wave along that line:

$$y_{ls}^i \geqq y_s^i + A^i, \quad i = 1, 2, 3, ...N, \tag{5.58}$$

where A^i is the amplitude of the ith wave along the segment A and B (or distance D). y_{ls}^i and y_s^i are respectively the value of the line y_{ls} (given in (5.29)) and the value of the parabola y_{ls} (given in (5.28)) at the position of the ith wave along the segment A and B.

The results of the Monte Carlo simulation concurred with the analytical solutions proposed in (5.51). Figure 5.13 shows the results of the Monte Carlo simulation in comparison with the

71
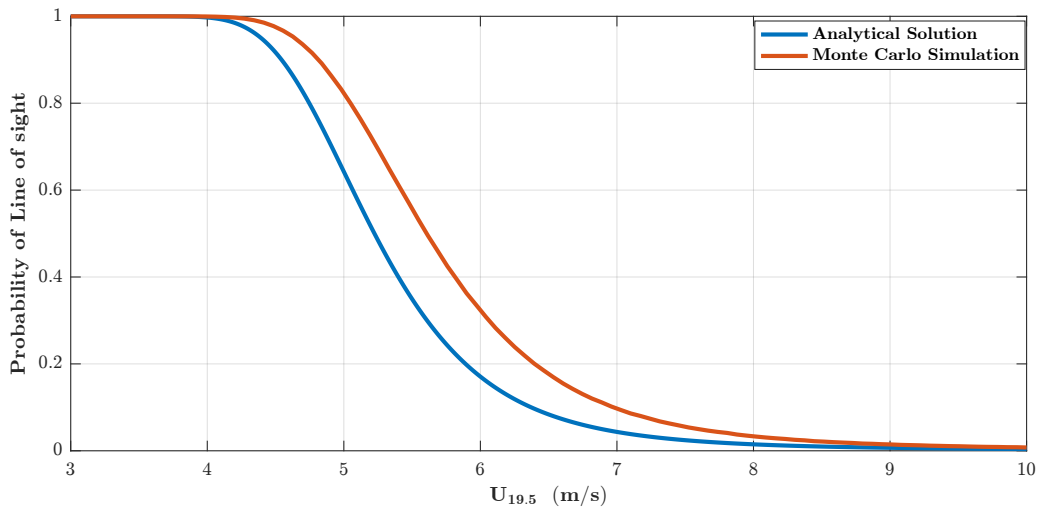
Figure 5.13: Comparison of the Monte Carlo simulation results and the analytical solution for the antenna height at 1 m and the distance D at 5 km.

analytical solution. Of the two results, the analytical solution in (5.51) uses the worst-case scenario by assuming that the extreme wave amplitude that is more likely to block the LoS is located around the peak of the parabola y_s. This assumption explains its underestimation of the probability of the LoS relative to the Monte Carlo results, which considered each wave in its actual position on top of the parabola joining the nodes.

5.7 Conclusion

In this chapter, the derivation of an expression for the probability of the LoS for local communication near the surface of the ocean was presented. Starting with a few key definitions, the chapter looked into the literature concerning the statistical and probabilistic properties of the ocean surface waves. The probability density function of the surface wave elevation and the surface wave height were described as the building blocks of the probability density function of the extreme wave heights. After that, the context of the study leading to the requirement of the evaluation of the probability of the LoS in the marine environment was described. It was argued that the estimation of this probability would add value to the local communication scheme of marine surface vehicles in the like of the Wave Glider platform. The added value will come from the minimisation of the power lost due to the local communication; this is an important aspect of the operation of the Wave Glider platforms, for instance, especially when these platforms are operating in a region with little to non-existent sunshine like the Southern Ocean in winter.

The elaboration of the context of the study was followed by a geometrical portrayal of the problem in Figure 5.7 and the introduction to the parameters that were later used in the derivation of the expression for the probability of the LoS. The derived probability was expressed in equation (5.51). Given the complex nature of this expression, the Gauss-Hermite quadrature was proposed as a numerical scheme to evaluate the values of the probability. In

this regards, equation (5.51) was converted into a form that was amiable to the Gauss-Hermite quadrature advancing to equation (5.56).

Additionally, the probability of the LoS was computed, using the proposed numerical scheme, for the following single random variables: the antenna height, the distance separating the two transceiver points and the wind speed at 10 m above the mean sea level. The results demonstrated that the derived expression was indeed a cumulative probability density function as its values were bounded within the interval $[0, 1]$. Also, the same results showed that the probability diminishes when either the wind speed or the distance between the two nodes increases. On the other hand, the probability increases in the case where the antenna height rises.

Lastly, the error rates, recorded during the test of the LoRa communication system across the surface of the ocean over a distance of 5 kilometers, were insufficient to evaluate the probability of the LoS from real life data. The causes of the inadequacy of the recorded error rates were the high activities of boats around the site of one of the antennas during the experiments. The temporal presence of the boats blocked the LoS between two nodes. As result, it became difficult to differentiate the packet lost due to the ocean surface waves to the ones cause by the boats when they passes between the two nodes.

Chapter 6

Sea State Estimation using Kalman Filter

6.1 Introduction

The preceding chapter proposed an approach to evaluate the probability of the LoS, near the ocean surface, between two small surface marine vehicles. The results obtained regarding antenna height indicated that the probability of the LoS would be improved with increased antenna height. Above the sea surface, it can be deduced from the same results that enabling the two nodes to transmit when they are simultaneously positioned at the crest of their nearest local wave would also improve the probability of the LoS. This idea was introduced in the previous chapter with the implication of the required knowledge concerning the surrounding wave field. Actually, mapping of the waves, i.e. the location and the amplitude of the wave in the surrounding of the platform must be know or at least be estimated in order to arrange for the platforms to send information when they are both of the highest crests locally. It means that this approach requires the three-dimensional information or estimation of the wave field which could be attained from the wave encountered by the platforms.

This chapter is an initial exploration into the application of the Kalman Filter to propose a provision to this estimation problem to improve the overall performance of the local communication system used in this research. The first part of the chapter describes further the literature on sea state estimation, the algorithm of the Kalman Filter and all the other literature applied in the accomplishment of the task as mentioned earlier.

6.2 The State Model for the Kalman Filter

The objective of this part of the research was to estimate or model the sea state in the attempt to extend the evaluation of the probability of the LoS to 3D and navigate efficiently small surface marine vehicles such as the Wave Glider platforms.

Assuming that the platforms will provide measurements (acceleration, rate, magnetic field and air pressure) that will be used to infer the elevation of the surface at their respective positions, the estimation of the wave field will be done using the Kalman Filter. The estimation method of the sea state is derived from the wave equation.

6.2.1 The Full Wave Equation

The wave equation is a partial differential equation that governs the behaviours of water waves, acoustic waves or light waves as they materialise in physics. The general one-dimensional and the two-dimensional wave equations with no loss are given respectively in (6.1) and (6.2).

$$\frac{\partial^2 \eta}{\partial t^2} - c_x^2 \frac{\partial^2 \eta}{\partial x^2} = f(t, x), \tag{6.1}$$

$$\frac{\partial^2 \eta}{\partial t^2} - c_x^2 \frac{\partial^2 \eta}{\partial x^2} - c_y^2 \frac{\partial^2 \eta}{\partial y^2} = f(t, x, y). \tag{6.2}$$

As this research deals with ocean water waves, it was appropriate that η represents the surface elevation of the water waves, t is the time variable, x and y are the spatial variables, and c_x and c_y are the phase speeds in the x and y directions respectively. On the right side of the two equations, $f(\cdot)$ is the resultant source function that excites the waves and is a function of time and location. The wave equation is a second order linear equation. When the excitation function is zero, the wave equation is called the homogeneous wave equation. The one dimensional homogeneous wave equation has an analytical solution in the form of:

$$\eta(t, \mathbf{x}) = \phi(\mathbf{x} - ct) + \psi(\mathbf{x} + ct). \tag{6.3}$$

where $\phi(\cdot)$ and $\psi(\cdot)$ are arbitrary functions. The author of [79] explains this in detail and validates this analytical solution. However, this research is considering a numerical solution in this chapter provided the initial and boundary conditions are known. Furthermore, an analytical form of the source function for the excitation of ocean waves is difficult to derive. This leads to a lack of sea state estimation based on the wave equation. Most authors focus on the estimation of the distributed wave spectrum in the frequency domain as indicated in Chapter 2. This research attempts to fill this lack by proposing a solution based on the Kalman Filter and the homogeneous wave equation. The purpose of the filter is to provide the missing link in the two-dimensional homogeneous wave equation, i.e. the source function in combination with the boundary conditions, and ultimately generates a solution for the inhomogeneous wave equation.

The derivation of the state-space model for the estimator is the focus of the next segment of this chapter.

6.2.2 The Transition Matrix and the State Equation

The general and basic form of the linear state equation (without white noise) for a Kalman Filter is:

$$\mathbf{x_{n+1}} = \mathbf{A}\mathbf{x_n} + \mathbf{B}\mathbf{u_n}, \tag{6.4}$$

where $\mathbf{x_n}$ is the state vector at the current time instant and $\mathbf{x_{n+1}}$ is the state vector at the next time instant. $\mathbf{A}$ is the state transition matrix, $\mathbf{B}$ is the input matrix, and $\mathbf{u_n}$ is the input to the

system at the current time instant n. In this subsection, the development of the transition matrix **A** for the application of the wave field estimation using the Kalman Filter is presented. The second term on the RHS of (6.4) is neglected as the input matrix **B** is small and the system's input **u** is unknown.

The matrix A is derived from the homogeneous wave equation. The homogeneous wave equation in three dimensions is expressed by:

$$\frac{\partial^2 \eta}{\partial t^2} - c_x^2 \frac{\partial^2 \eta}{\partial x^2} - c_y^2 \frac{\partial^2 \eta}{\partial y^2} = 0. \tag{6.5}$$

This partial differential equation is discretised in space and time at the spatial and time intervals of Δx, Δy and Δt respectively based on the finite difference method for a region $X \times Y \times T$. Using the Leapfrog discretisation scheme in 2D [80], the discretised wave equation is:

$$\frac{\eta_{i,j}^{n+1} - 2\eta_{i,j}^n + \eta_{i,j}^{n-1}}{\Delta t^2} = c_x^2 \frac{\eta_{i+1,j}^n - 2\eta_{i,j}^n + \eta_{i-1,j}^n}{\Delta x^2} + c_y^2 \frac{\eta_{i,j+1}^n - 2\eta_{i,j}^n + \eta_{i,j-1}^n}{\Delta y^2}, \tag{6.6}$$

where i and j represent the cell indices in the x and y directions, and n is the time index. Through algebraic manipulations, (6.6) is explicitly rearranged to:

$$\eta_{i,j}^{n+1} = 2\left(1 - \frac{c_x^2 \Delta t^2}{\Delta x^2} - \frac{c_y^2 \Delta t^2}{\Delta y^2}\right)\eta_{i,j}^n - \eta_{i,j}^{n-1} + \frac{c_x^2 \Delta t^2}{\Delta x^2}\eta_{i+1,j}^n + \frac{c_x^2 \Delta t^2}{\Delta x^2}\eta_{i-1,j}^n + \frac{c_y^2 \Delta t^2}{\Delta y^2}\eta_{i,j+1}^n + \frac{c_y^2 \Delta t^2}{\Delta y^2}\eta_{i,j-1}^n. \tag{6.7}$$

This is further rewritten in a vector multiplication format as:

$$\eta_{i,j}^{n+1} = \mathbf{H}\chi_n, \tag{6.8}$$

with

$$\mathbf{H} = \left[\left(\frac{c_x^2 \Delta t^2}{\Delta x^2}\right) \quad 2 \times \left(1 - \frac{c_x^2 \Delta t^2}{\Delta x^2} - \frac{c_y^2 \Delta t^2}{\Delta y^2}\right) \quad (-1) \quad \left(\frac{c_x^2 \Delta t^2}{\Delta x^2}\right) \quad \left(\frac{c_y^2 \Delta t^2}{\Delta y^2}\right) \quad \left(\frac{c_y^2 \Delta t^2}{\Delta y^2}\right)\right],$$

and

$$\chi_n = \left[\eta_{i-1,j}^n \quad \eta_{i,j}^n \quad \eta_{i,j}^{n-1} \quad \eta_{i+1,j}^n \quad \eta_{i,j-1}^n \quad \eta_{i,j-1}^n\right]^T.$$

T is the transpose operation on the vector. Assimilating a spatial grid example shown in Figure 6.1a and exploded in Figure 6.1b, a set of (6.8) could be written out for each cell, rearranged and combined into a matrix equation in the form of:

$$\mathbf{x_{n+1}} = \mathbf{Ax_n}, \tag{6.9}$$

where $\mathbf{x_n}$ is a column vector of the surface elevation at each grid cell for the present and the previous time instants (time instant n and previous time instant $(n-1)$ and **A** is the transition matrix formed by the interpolation of the vector **H** of each cell.

(a) Example of spatial grid of 3×3 cells

(b) Grid of 5 cells extended over 3 time instants $\mathbf{n-1}$, $\mathbf{n}$ and $\mathbf{n+1}$
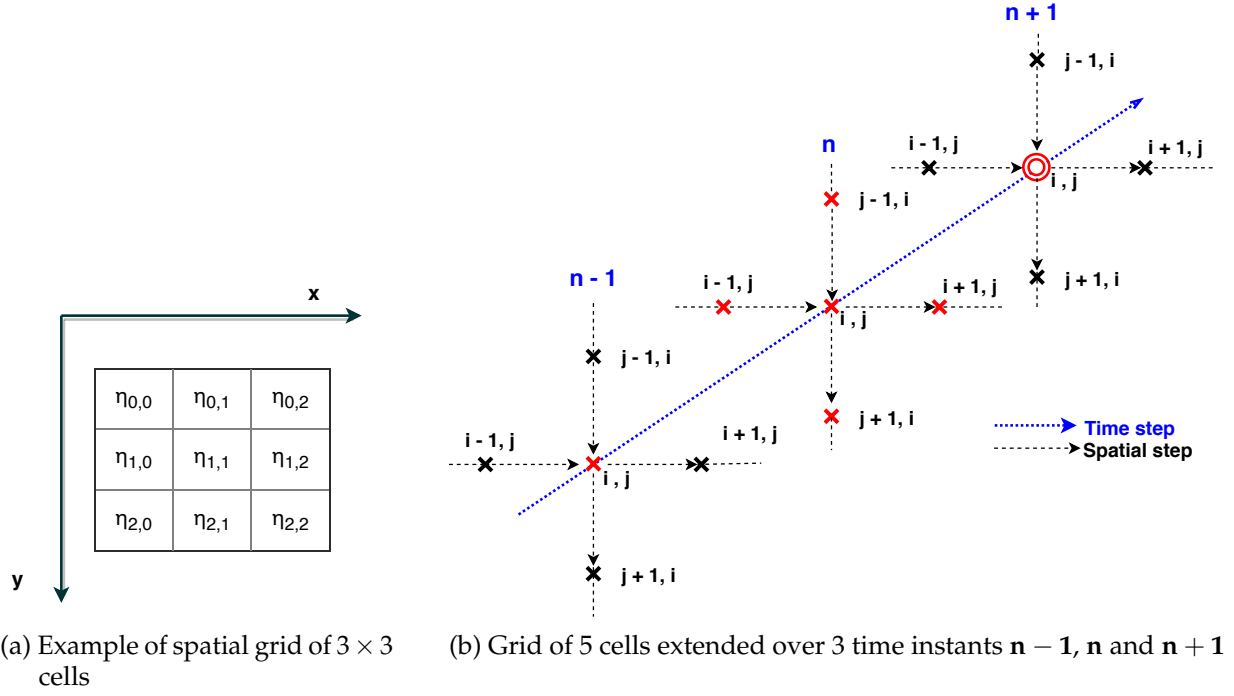
Figure 6.1: Spatial and temporal grids supporting the development of the system model. In (b), the same spatial grid was extended over three time instants to illustrate the different points (cells marked with ✖) needed in space and time to evaluate the surface elevation at location (i, j) at time $n + 1$ (marked by two concentric circles).

The size of $\mathbf{x_n}$ is $m = 2 \times N_x \times N_y$ with N_x equal to the number of cells in the x-direction and N_y in the y-direction. The factor of 2 is required to account for the temporal 2nd order of the homogeneous wave equation and retain in memory the previous time value of the surface wave elevation at each grid cell. The size of the transition matrix $\mathbf{A}$ is, therefore, $m \times m = (2 \times N_x \times N_y) \times (2 \times N_x \times N_y)$.

Adding the excitation source to the equation as mentioned earlier, it becomes a non-homogeneous discretised wave equation given by:

$$\mathbf{x_{n+1}} = \mathbf{A}\mathbf{x_n} + \mathbf{w_n}, \tag{6.10}$$

with $\mathbf{w_n}$ assumed to be white noise representing the excitation energy from the wind predominantly at each cell of the grid region and associated with $f(\cdot)$. The covariance of $\mathbf{w_n}$ is justified by an insight on the physic governing the magnitude of change in the surface elevation over one time step. In other words, $\mathbf{w_n}$ is meant to contribute for all changes in $\mathbf{x_{n+1}}$ that are not predicted by the term $\mathbf{A}\mathbf{x_n}$. Thus, it depends on the size of the time step which is itself linked to the wind speed as explained in the following part of the section.

The pattern used to assemble the column vector $\mathbf{x_n}$ is extended in (6.11), building on from the grid shown previously in Figure 6.1a.

$$\mathbf{x_n} = \begin{bmatrix} \eta_{0,0} & v_{0,0} & \eta_{1,0} & v_{1,0} & \eta_{2,0} & v_{2,0} & | & \eta_{0,1} & v_{0,1} & \eta_{1,1} & v_{1,1} & \eta_{2,1} & v_{2,1} & | & \eta_{0,2} & v_{0,2} & \eta_{1,2} & v_{1,2} & \eta_{2,2} & v_{2,2} \end{bmatrix}^T . \tag{6.11}$$

The column vector is delimited in three parts to show how the surface elevation $\eta_{i,j}$ are assigned in comparison to their position on Figure 6.1a. The columns of the grid (y-direction) are stacked together in an increasing order (the first column on top) to get one column vector $\mathbf{x_n}$. For each $\eta_{i,j}$, there is an associated $v_{i,j}$ which represent the value of $\eta_{i,j}$ at the previous time instant. In other words, $v_{i,j}$ retains the previous value of $\eta_{i,j}$ at the same location (cell). The presence of $v_{i,j}$ is imperative and justified by the order of the wave equation.

6.2.3 Numerical Stability Condition of the Model

The numerical stability is a key concern in the application of any numerical scheme. Here, the Leapfrog numerical scheme is not an exception to this rule. For the results produced by either (6.6) or (6.7) to be stable, the selection of the spatial and time steps Δx, Δy and Δt must abide by a certain stability condition. The condition states that:

$$\left(\frac{c_x \Delta t}{\Delta x}\right)^2 + \left(\frac{c_y \Delta t}{\Delta y}\right)^2 \leq \frac{1}{2}. \tag{6.12}$$

This stability condition is called the Courant-Friedrichs Lewy condition or CFL condition. For the wave, the CFL condition ensures that the wave does not propagate spatially for more than a fraction of the grid-cell during a single time step and thus ensures a stable propagation of the waves across the region of interest [80].

The approach in (6.13) was implemented in the determination of the value of Δt that would provide stability when the values of Δx, Δy, c_x and c_y are fixed.

$$\Delta t = min \left[\frac{\Delta}{\sqrt{2(c_x^2 + c_y^2)}}, \frac{\Delta y}{\sqrt{2(c_x^2 + c_y^2)}} \right]. \tag{6.13}$$

From this routine, the minimum Δt that satisfies the stability condition was obtained. Complying with this CFL stability condition was a sufficient prerequisite for elaboration of a stable transition matrix $\mathbf{A}$, i.e a transition matrix $\mathbf{A}$ that would produce a stable state vector (wave surface elevation) from (6.9).

6.2.4 Boundary Conditions

The Leapfrog numerical (discretisation) scheme is a second order centre difference method. The boundary conditions at all four sides of the spatial region are therefore essential for the correct implementation of this numerical solution being offered in this chapter. Considering the same grid shown in Figure 6.1a, the region is folded around itself to get the boundary conditions. The resulting spatial grid is demonstrated in Figure 6.2. This boundary condition is reflected in the transition matrix $\mathbf{A}$. Looking back at the Leapfrog numerical scheme in its explicit form as in (6.7), (6.8) is recomputed to include the new cells at the boundaries. This leads to new entries of the transition matrix $\mathbf{A}$. For a 3×3 region as illustrated in Figure 6.2,

Figure 6.2: Example of spatial grid of 3×3 cells.

the transition matrix $\mathbf{A}$ is a 18×18 matrix and is constructed in (6.14). The zero entries are left empty to highlight the strong structure of the matrix. The transition matrix $\mathbf{A}$ is displayed to show its structure and its dimensions. The coefficient in $\mathbf{A}$ are: $\alpha_x = \left(\frac{c_x \Delta t}{\Delta x}\right)^2$, $\alpha_y = \left(\frac{c_y \Delta t}{\Delta y}\right)^2$ and $\alpha = 1 - (\alpha_x + \alpha_y)$. These coefficients are the same in the row vector $\mathbf{H}$ introduced in (6.8).

$$
A = \begin{bmatrix}
2\alpha & -1 & \alpha_x & & \alpha_x & & \alpha_y & & & & & \alpha_y & & & & & & \\
1 & & & & & & & & & & & & & & & & & \\
\alpha_x & & 2\alpha & -1 & \alpha_x & & & & \alpha_y & & & & & \alpha_y & & & & \\
& & 1 & & & & & & & & & & & & & & & \\
\alpha_x & & \alpha_x & & 2\alpha & -1 & & & & & \alpha_y & & & & & \alpha_y & & \\
& & & & 1 & & & & & & & & & & & & & \\
\alpha_y & & & & & & 2\alpha & -1 & \alpha_x & & \alpha_x & & \alpha_y & & & & & \\
& & & & & & 1 & & & & & & & & & & & \\
& & \alpha_y & & & & \alpha_x & & 2\alpha & -1 & \alpha_x & & & & \alpha_y & & & \\
& & & & & & & & 1 & & & & & & & & & \\
& & & & \alpha_y & & \alpha_x & & \alpha_x & & 2\alpha & -1 & & & & & \alpha_y & \\
& & & & & & & & & & 1 & & & & & & & \\
\alpha_y & & & & & & \alpha_y & & & & & & 2\alpha & -1 & \alpha_x & & \alpha_x & \\
& & & & & & & & & & & & 1 & & & & & \\
& & \alpha_y & & & & & & \alpha_y & & & & \alpha_x & & 2\alpha & -1 & \alpha_x & \\
& & & & & & & & & & & & & & 1 & & & \\
& & & & \alpha_y & & & & & & \alpha_y & & \alpha_x & & \alpha_x & & 2\alpha & -1 \\
& & & & & & & & & & & & & & & & 1 &
\end{bmatrix}.
$$

$$(6.14)$$

This approach for boundary conditions has its merits, it ensures the continuity and the periodicity of the wave in the region. One disadvantage of this approach is that the difference in the surface elevation between two opposing sides might be too big and, as a result, introduce a discontinuity in the region. This effect can be minimised by making the spatial and time steps small.

6.2.5 The Measurement Equation and Observability of the State-space Model

The measurement equation, also known as the observation equation is given in the form:

$$\mathbf{y_n} = \mathbf{C^T x_n} + \mathbf{v_n}, \tag{6.15}$$

where $\mathbf{y_n}$ is the measurement at time t_n taken from some of the cells within the region of interest, $\mathbf{C^T}$ is the output matrix and $\mathbf{v_n}$ is the measurement error or white noise associated with the observation. In the context of the local communication that is evaluated in this research, it is assumed that there would be two measurement points (cells) in the region of interest. In that regard, the measurement matrix $\mathbf{C^T}$ is $2 \times m$ in size and in the form:

$$\mathbf{C^T} = \begin{bmatrix} 0 & \cdots & p_1 & \cdots & \cdots & 0 \\ 0 & \cdots & \cdots & p_2 & \cdots & 0 \end{bmatrix}. \tag{6.16}$$

The dots represent the continuation of the zero entries. p_1 and p_2 are integers indicating the locations of the two measurement cells. They relate the coordinates in meters (or grid position) of the cells where the measurements are collected into $\mathbf{C^T}$. Given the spatial discretisation factors, N_x and N_y, the length (and width) of the spatial region, L, as well as the Cartesian coordinates of the two measurement points, (a_i, b_i), $i = 1, 2$ (in meters within the region), the following expression was developed to calculate the value of the positions of p_1 and p_2 in $\mathbf{C^T}$.

$$p_i = (2N) \times (B_i - 1) + 2 \times (A_i - 1) + 1 \qquad i = 1, 2, \tag{6.17}$$

where $A_i = \frac{a_i \times L}{N}$ and $B_i = \frac{b_i \times L}{N}$. A_i and B_i are rounded up to the nearest integer to ensure that p_i is an integer. The values of the entries at p_1 and p_2 are set to 1 as they capture the surface elevation which is the state variable. Using the work accomplished in [81], the gradient of the measurement at each point could be extracted from the Inertial Measurement Unit (IMU) on board the Wave Glider platform and can be included in the measurement vector. This complementary measurement data would alter the form of the $\mathbf{C^T}$. This addition is beyond the scope of this research.

The observation equation and the discretised wave equation give (6.18), the full Kalman Filter model equation.

$$\begin{aligned} \mathbf{x_{n+1}} &= \mathbf{A x_n} + \mathbf{w_n}, \\ \mathbf{y_n} &= \mathbf{C^T x_n} + \mathbf{v_n}. \end{aligned} \tag{6.18}$$

The observability of a system is an indicator of the insight that the measurement data can provide on the evaluation of the value of all the states of such a system. For a state-space

model system of order m, the full rank of the observability matrix Obv, expressed by:

$$Obv = \begin{bmatrix} \mathbf{C^T} \\ \mathbf{C^T A} \\ \mathbf{C^T A^2} \\ \vdots \\ \vdots \\ \vdots \\ \mathbf{C^T A}^{m-1} \end{bmatrix}, \tag{6.19}$$

implies that the system is fully observable. Whereas, the opposite stipulates that the system in not fully observable. Both the transition matrix $\mathbf{A}$ and the measurement $\mathbf{C^T}$ are very sparse with $\mathbf{C^T}$ only having two non-zero elements. The observability matrix has a very low rank depending on the size of the domain of interest where the ocean surface elevation is estimated. The rank of Obv gives a binary outcome on the observability of the state-space system, but does not indicate which states are not observable in the system. The large number of states in this study makes it almost impossible to identify and separate the non-observable state from the observable ones.

In a nutshell, the system model expressed in (6.18) is not fully observable as the observability matrix Obv does not have a full rank. Table 6.1 draws attention to the number of system states that are observable out of the total of $m = 2 \times N_x \times N_y$.

Table 6.1: The number of observable system states based on the rank of the observability matrix in (6.19). This table was compiled for a domain of 30 meters by 30 meters and a wind direction of $\dfrac{\pi}{6}$ rad.

N_x	N_y	Total number of system states ($m = 2 \times N_x \times N_y$)	Numerical Rank of Obv
2	2	8	6
4	4	32	12
8	8	128	38
16	16	512	106
32	32	2018	535
64	64	8192	3544

The value in Table 6.1 indicated a poorly observable system overall, meaning that the state estimation errors would be reasonably small around the observation points and increase for system states away from the two observation points. The observability of the system is significantly better when N_x and N_y are set to 64 compared to 32. However, the computational requirement at 64 was beyond the computational resources available in the research for the Kalman Filter algorithm. The value of N_x and N_y are thus set to 32 in the Kalman filter simulations.

The wave field assimilation process is summarised in Figure 6.3 showing the different parts
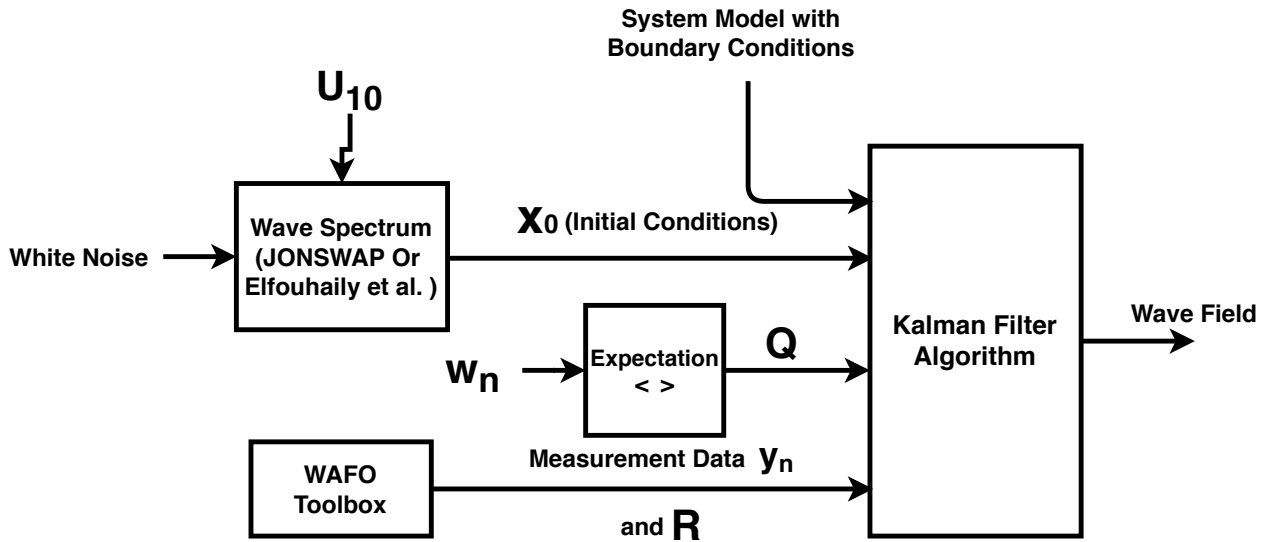
Figure 6.3: Block diagram illustration the process for the Kalman Filter model.

required in the formulation of the solution for the wave equation using the Kalman Filter. The last part needed before the evaluation of the method is the initial conditions. The generation of these initial conditions is the focus of the last part of this section.

6.2.6 Initial Conditions for the Wave Field

The initial wave field conditions, i.e. the starting surface wave elevations, were generated from one of the 2-dimensional wave spectra introduced in the previous chapter using the 2D Fourier transform. The 2D parametric (directional) wave spectrum developed in [14] is employed in the generation of the initial wave field. This wave spectrum was employed in this chapter because it provides flexibility to generate a variety of seas, changing from a young via a mature to a fully developed sea for a given wind speed of U_{10}. The fully developed sea corresponds to the Pierson–Moskowitz (PM) sea. Its directional wavenumber version is given in Appendix C.

The surface elevation was generated as coloured noise from the wave spectrum following the approach instantiated below:

- Select the spatial region size ($L \times L$) and the number ($N \times N$) of spatial samples (grid cells);

- Select the wind speed, U_{10} (or $U_{19.5}$), wind direction, θ, and the wave age parameter, Ω;

- Compute the spatial frequencies, k_x and k_y and the corresponding directional spectrum magnitude;

- Create the array of randomised discrete Hermitian Fourier amplitudes from the spectrum magnitudes. The Hermitian Fourier amplitudes are essential to ensure that the Inverse Fourier Transform to be computed next gives real values for the surface elevation (i.e. the imaginary part of the complex values from the Inverse Fourier Transform must be zero);

- Convert the random Hermitian Fourier amplitudes to the physical wave heights using the 2-dimensional Inverse Fourier Transform;

- Extract the sea surface heights from the inverse Fourier Transform which is a complex value. The surface elevation is the real part of the complex value obtained from the inverse Fourier operation.

6.3 Preliminary Results

This section presents the preliminary results obtained from the procedures and literature described beforehand. These results include the initial wave field generated from the directional wave spectrum from the Inverse Fourier Transform and the outcome of (6.9) performed on the generated wave field representing X_n. The latter result illustrates the numerical stability of the state matrix $\mathbf{A}$.

6.3.1 Surface Wave Elevation

The surface elevation, η, was generated for a small region of 20 m $\times$ 20 m with 128 $\times$ 128 grid cells. Figure C.1 in Appendix C displays the wave field for a fully developed sea for a wind speed U_{10} equal to 10 m/s with three different wind directions θ. The different wind directions were 0, $\frac{\pi}{4}$ and $\frac{\pi}{2}$ rad. Comparable results are shown in Figure C.2 for the same conditions, i.e. fully developed sea but at a lower wind speed of 7 m/s.

6.3.2 Outcome of the State Equation

The state equation was conveyed in (6.9). The state vector $\mathbf{x_n}$ was attained from the surface generated η and displayed in Figure C.1 and Figure C.2 by converting the 2-dimensional surface elevation array into a column vector. Thereafter, $\mathbf{x_{n+1}}$ was computed as per (6.10). The resulting column vector $\mathbf{x_{n+1}}$ was transformed back into a 2-dimensional surface elevation array. This operation was computed iteratively while closely watching the value of $\mathbf{x_{n+1}}$ and considering the numerical stability of the system. The results after 100 iterations are plotted in Figure C.3 and Figure C.4 for the wind speed U_{10} set to 10 m/s and 7 m/s respectively in Appendix C.

These results showed that the state equation is numerically stable, and can be used in conjunction with the measurement equation to practically estimate the ocean surface elevation for engineering and oceanographic applications. This estimation is the focus of the next section of this chapter.

6.4 Sea State Estimation

This section presents the three-dimensional sea state estimation based on the system model and initial surface condition presented in the first part of the chapter. The state estimation will be developed around the Kalman Filtering algorithm which was developed and published by Rudolf Emil Kalman in 1960 [82]. The Kalman Filter is a linear assimilation routine used to approximate the states of a system and update the state values when any measurement or observation is available.

6.4.1 The Kalmam Filter Algorithm

This algorithm is summarised here for a discretised state-space model in form of (6.18) where the covariances of $\mathbf{w_n}$ and $\mathbf{v_n}$ are respectively represented by the matrices $\mathbf{Q}$ and $\mathbf{R}$. They are defined by [13]:

$$
\begin{aligned}
\mathbb{E} < \mathbf{w_i w_j}^T > \quad &= \quad \begin{cases} \mathbf{Q}, & \text{if } i = j, \\ \mathbf{0}, & \text{otherwise}, \end{cases} \\
\mathbb{E} < \mathbf{v_i v_j}^T > \quad &= \quad \begin{cases} \mathbf{R}, & \text{if } i = j, \\ \mathbf{0}, & \text{otherwise}, \end{cases} \\
\mathbb{E} < \mathbf{w_i v_j}^T > \quad &= \quad \mathbf{0}, \text{ for all } i \ \& \ j,
\end{aligned}
\tag{6.20}
$$

where $\mathbb{E} < \cdot, \cdot^T >$ and T are the expectation and transpose operator respectively as stated earlier in the dissertation. The covariance matrix $\mathbf{Q}$ depends on the wind speed as described before.

The Kalman Filter algorithm is a recursive routine, and each iteration constitutes four steps of computations:

1. The first one is the computation of the Kalman gain $\mathbf{K_n}$.

2. This is followed by the correction or update step where the estimated system states are updated using the Kalman gain and the available measurements.

3. The next step is the computation of the updated state error covariance.

4. Moreover, the final step is the prediction or the researchion stage where the values of the system states for the next time instance and the estimated state error covariance are estimated.

The diagram in Figure 6.4 illustrates the four steps described above with all the matrix' computations required at each step of the iteration.

Each iteration requires, at its start, the estimated states $\hat{\mathbf{x}}_\mathbf{n}^-$ and the estimated state error covariance matrix $\mathbf{P_n^-}$ from the previous one if there were any other iterations or as the filter's initial conditions (if it is the first iteration). The estimated state error covariance matrix $\mathbf{P_n^-}$ is defined by:

$$
\mathbf{P_n^-} = \mathbb{E} < \mathbf{e_n^- e_n^-}^T > = \mathbb{E} < \left(\mathbf{x_n} - \hat{\mathbf{x}}_\mathbf{n}^- \right) \left(\mathbf{x_n} - \hat{\mathbf{x}}_\mathbf{n}^- \right)^T >,
\tag{6.21}
$$

The Initial Conditions:
State $\mathbf{x}^-_0$ and
its error covariance $\mathbf{P}^-_0$

Computation of the Kalman gain :
$$\mathbf{K_n = P_n^- (C_n{}^T)^T (C_n{}^T\, P_n^-\, (C_n{}^T)^T\, + R)^{-1}}$$

Computation of the state estimate for the next time instance :
$$\mathbf{x^-_{n+1|n} = A\, x_n}$$
$$\mathbf{P^-_{n+1|n} = A\, P_n\, A^T\, + Q}$$

Update of state estimates with measurement $\mathbf{y_n}$:
$$\mathbf{x_n = x_n^- + K_n\, (y_n - (C_n{}^T)\, x_n^-)}$$

Computation of the error co-variance for the updated state estimate :
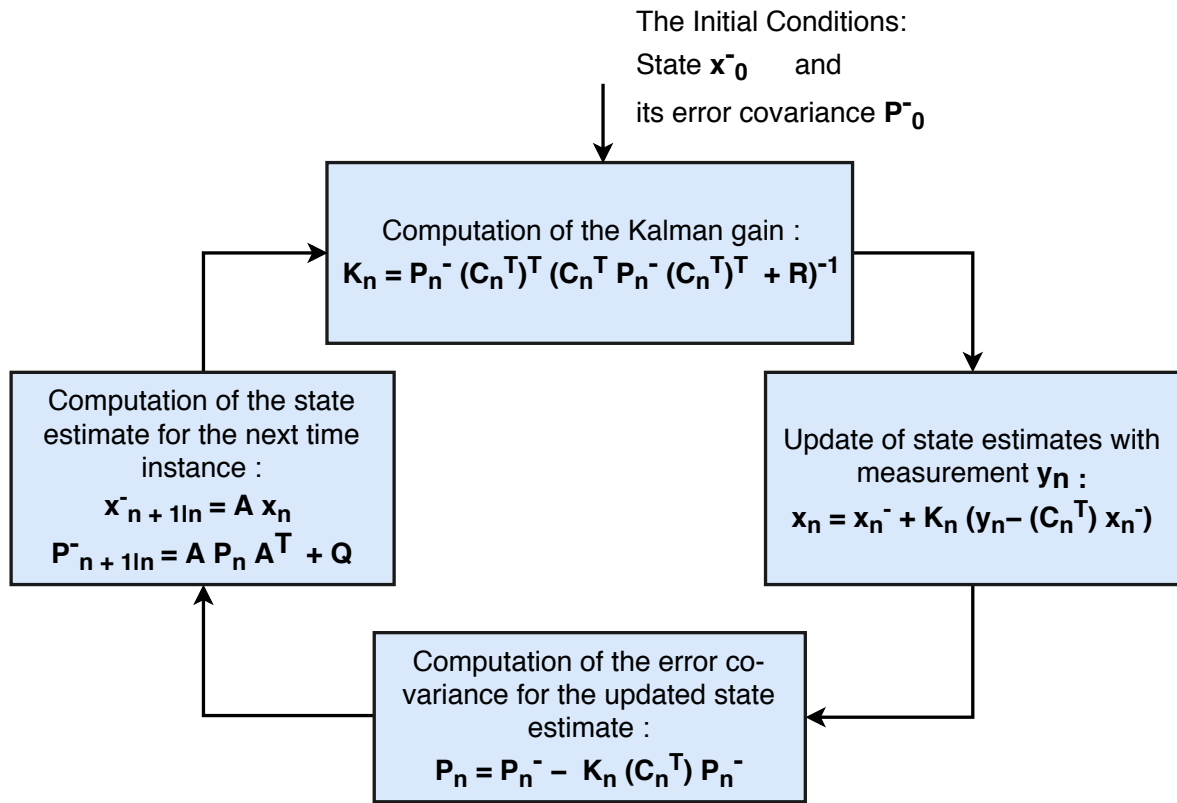$$\mathbf{P_n = P_n^- -\; K_n\, (C_n{}^T)\, P_n^-}$$

Figure 6.4: The four steps in each iteration of the Kalman Filter routine. Here $\mathbf{x_n}$ represents the estimated states. It should not be confused with the actual system state values because of the missing ˆ. This diagram is adapted from [13].

and the updated state error covariance matrix $\mathbf{P_n}$ is:

$$\mathbf{P_n} = \mathbb{E} < \mathbf{e_n e_n}^T >= \mathbb{E} < \left(\mathbf{x_n} - \hat{\mathbf{x}}_\mathbf{n}\right)\left(\mathbf{x_n} - \hat{\mathbf{x}}_\mathbf{n}\right)^T > . \tag{6.22}$$

The superscript sign ⁻ differentiates the estimated state or state error covariance from the corrected (updated) one.

6.4.2 Generation of Measurements Data

Measurement is an important aspect of the Kalman Filter application to state estimations. This research is an initial study; no field test to collect sea state data in a controlled environment is associated with this initial study. This introduces a lack of real sea surface elevation data which is required for the implementation and assessment of the Kalman Filter in this research. A compromise was attained to produce measurement data using simulations to overcome the limitation instigated by the out-of-scope field test. It involved the use of the Matlab Toolbox WAFO developed for analysis and simulations of random waves and random fatigues [83] induced by waves on marine structures. The name, WAFO, stands for Wave Analysis for Fatigue and Oceanography, it is designed for physical oceanographers and engineers. This toolbox has routines to simulate or analyse random (Gaussian and Lagrange) waves or random loads in two or three dimensions. It can also be used to study the statistical properties of the

real sea surface wave data collected from the sea using any observation methods and sensors such as the sea buoys [83]. Its computational and graphical tools are based on the regression approximation and general contemporary methods.

In this research, the Matlab toolbox WAFO was used to simulate a Lagrange wave field from which the measurement data were extracted at two selected coordinates (within the grid of the simulated wave field). According to the authors of [84], the Lagrange wave model leads to more realistic ocean waves as this model produces asymmetric ocean waves similar to the ones in the real ocean. The required parameters for the Lagrange wave field's simulation routines were the significant wave height, the dominant wave period and the principal wave direction. Other prerequisites were the selections of the spreading function and the wave (variance) spectrum. The different options for these two prerequisite selections are explained in the tutorials [85, 86] made available by the authors of the toolbox. The JONSWAP wave spectrum and the "cos2s" spreading function were selected. The Lagrange wavefield simulation is accomplished with the 2D Fast Fourier Transform (FFT) over space followed by an iteration over time. The routine is also memory consuming. In this regard, the focus is only put on the first order Lagrange wave field for the target of these tasks.

As aforementioned, we required two observation points of the 2-dimensional spatial grid to imitate the readings from two small surface marine vehicles. The wave elevations at the two selected points were extracted from the measurement data by selecting any two appropriate points to satisfy this condition. This measurement data were two pointwise time-varying surface wave elevations. For a given significant wave, dominant wave period and wave direction, the two pointwise time series data acquired at the two defined positions on the regional grid is presented under the simulation results section of this chapter.

6.4.3 Simulations

With the measurement data secured from the WAFO simulations, the values of the initial state covariance, $\mathbf{P_0^-}$, was deduced. The deduction was in consideration of the initial condition wave field. The initial state covariance $\mathbf{P_0^-}$ was set to:

$$\mathbf{P_0^-} = \left(10^{-2} \times \mathbf{I_{m \times m}}\right)^2 \text{ meters square.} \tag{6.23}$$

where $\mathbf{I}$ is the identity matrix of order m. Giving the properties of the grid and the time step of the time discretisation. The characteristics of white noise $\mathbf{w_n}$ were selected to reflect on the approximated step change of the surface elevation at each grid point from one time instant to the next one. Therefore, the co-variance $\mathbf{Q}$ of the white noise $\mathbf{w_n}$ approximates the energy input per unit of area to the system. $\mathbf{Q}$ is set to:

$$\mathbf{Q} = \left(10^{-2} \times \mathbf{I_{m \times m}}\right)^2 \text{ meters square per time step.} \tag{6.24}$$

This means the standard deviation of $\mathbf{w_n}$ is 0.01 meters. The measurement data were adopted with high confidence, leading to a standard deviation of 5% for observation error. The measurement errors' co-variance $\mathbf{R}$ was therefore:

$$\mathbf{R} = (0.05 \times \mathbf{I_{2 \times 2}})^2 . \tag{6.25}$$

The simulation was completed for a smaller region of 30×30 meters square subdivided into a 32×32 grid cell. The memory capacity of the computer dictated the area of the simulation region as the computer could only handle $2 \times 32 \times 32$ system states (which is small) in the Kalman Filter algorithm without running out of memory. Also, the 30×30 meters square was deemed sufficient to indicate whether or not the Kalman Filter algorithm together with the homogeneous wave equation can be employed to estimate the wave field in 3-dimension for scientific and engineering applications, which include the communication of LoS between two small surface marine vehicles.

For a wind speed U_{10}, its associated significant wave height and dominant wave period were used to generate the measurement data as explained previously. The transition matrix $\mathbf{A}$ was derived for the defined wind speed and the observation/measurement matrix $\mathbf{C^T}$ was derived per the specified measurement location in the grid. The initial conditions for the wave field, i.e. $\mathbf{x_0}$, was generated similarly to the example shown in Figure C.1 but this time for the defined wind speed and the region of 30×30 meters square. All the essential matrix and vectors were obtained and fed into the Kalman Filter routines. We considered three wind speed values for these simulations. These wind speeds were 7.5, 10 and 12.5 m/s; however, solely the results of the simulations with the wind speed equal to 10 m/s are put forward to remain in the decreed length of this document.

6.4.4 Results of the Kalman Filter Simulations

The plots of the time series surface elevations obtained from the WAFO simulation for the measurement data are shown in Figure 6.5. This observation data were collected at the coordinates (3,5) and (25,26) which were selected. The sampling time of the measurement was set to be equal to the discretisation time step. The discretisation time step, also used to construct the state transition matrix $\mathbf{A}$, was depending on the wind speed through its dependence on the phase speeds of the surface wave as revealed in (6.13). The phase speeds c_x, and c_y were calculated from the wind speed U_{10} given that the wave spectrum defines them. Table 6.2 summarises all numerical values of the key parameters for each of the wind speed considered for these wave field estimations.

Starting with the initial conditions for the surface elevation, $\mathbf{x_0}$, given in Figure 6.6, the sea state was estimated in simulation in MATLAB. Figure 6.7 shows the predicted surface elevations at the measurement locations given afore. The predicted surface elevation at the observation locations converged with the measured surface elevation at their corresponding cells (locations) throughout the simulation. This is the case although the initial wave field was
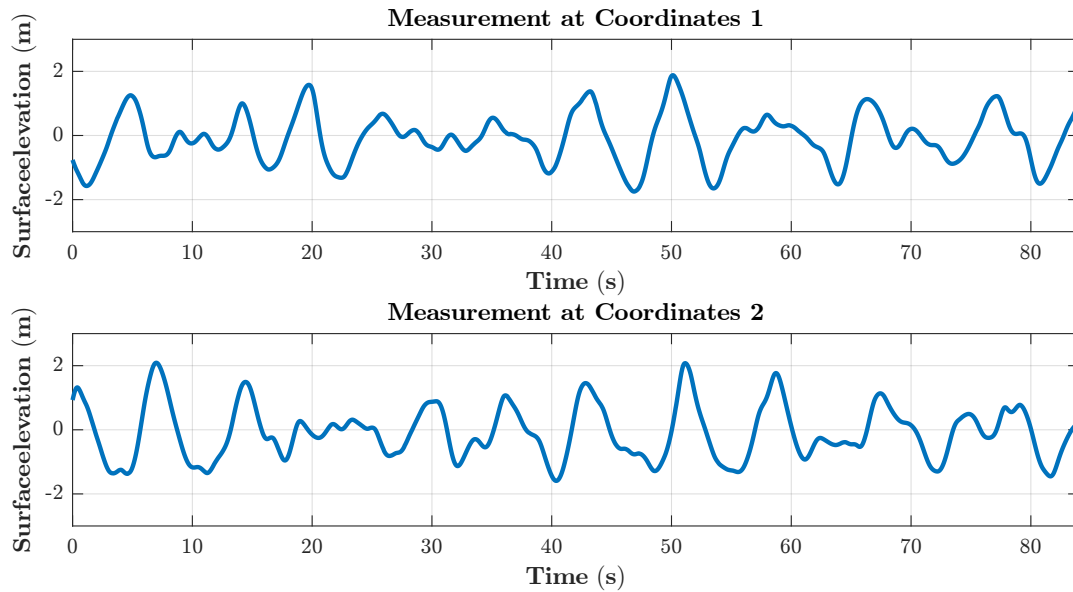
Figure 6.5: Point-wise measurement data generated using WAFO toolbox for a region of 30 ×
30 meters square at the coordinates (3,5) for Location 1 and (25,26) for Location 2.

Table 6.2: Key parameters depending on the wind speed and required for the 3D wave field estimation. The significant wave height and the wave period are barely approximations of the actual values based on the literature.

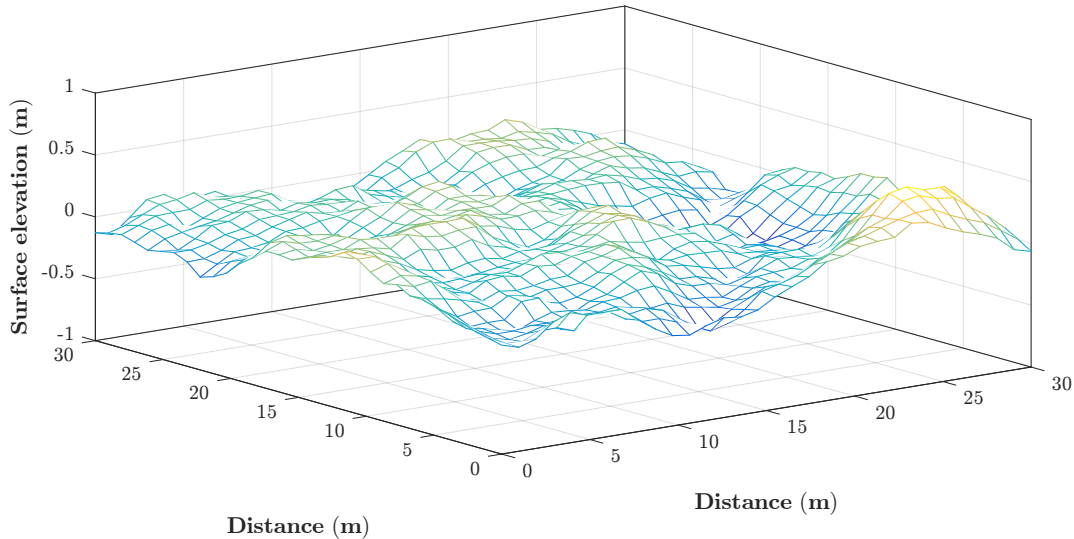| Parameters	Numerical Values		
Wind speed (m/s)	7.5	10	12.5
Phase speed (m/s)	8.93	11.90	14.88
Discretisation time step (seconds)	0.0742	0.0556	0.0445
Significant wave weight (meters)	1.5	2.6	4
Dominant wave period (seconds)	5.71	7.62	9.52

88

Figure 6.6: Initial surface elevation used as initial system states $\mathbf{x_0}$ in the estimation of the sea state.

unrelated to the measurement data in any way. The errors in the prediction were minimum at both locations. However, a slight behavioural difference is noticeable between the two errors.

Unlike the local surface elevation that could be plotted concerning time for the whole duration of the simulations, the surface elevation over the whole region of interest (30×30 meters square) required a surface plot every time instant to show its behaviour accurately. The 3D surface elevations are shown in Figure 6.8 for three different times of the simulations, i.e. at 27.8, 55.6 and 83.4 seconds respectively. These three surface elevation plots showed the consistency of the waves in regards to the behaviour of the expected waves for a significant wave height equal to 2.6 meters for a wind speed U_{10} equal to 10 m/s. There is no discontinuity over the surface plot, supporting the practicality of the methods developed in this chapter. Even though the surface elevation looked realistic, the confidence in these results could only be dictated by the error associated with them. In this regard, the error covariance associated with each of the surface elevations in Figure 6.8 were compiled and the error at each cell of the spatial domain extracted. These errors were plotted in Figure 6.9 as a 3D surface plot.

The errors plots exhibit the direction of the wave propagation in space and time which was $\frac{\pi}{4}$. This is unveiled by the narrow rift along the diagonal of the plots. Beyond this, the errors were relatively constant over the rest of the region. The errors showed an increase from one-time instance to the next one, starting with the initial approximated error at 0.001 meters. On average, the errors increased from 0.2 meters at a time equal to 27.8 seconds to 0.3 meters at time 83.4 seconds. Nevertheless, the results stand as a good starting point into the application of the Kalman Filter in the sea state estimation provided that measurement data is accessible at one or more locations in the region of interest. The overall behaviour of the error, i.e. the value of the errors at different times depends strongly on the initial errors. This is to say that an initial 3D surface elevation with minimum errors will provide a reliable but diminishing surface elevation from the Kalman Filter. Furthermore, the entries in the covariance matrix $\mathbf{Q}$
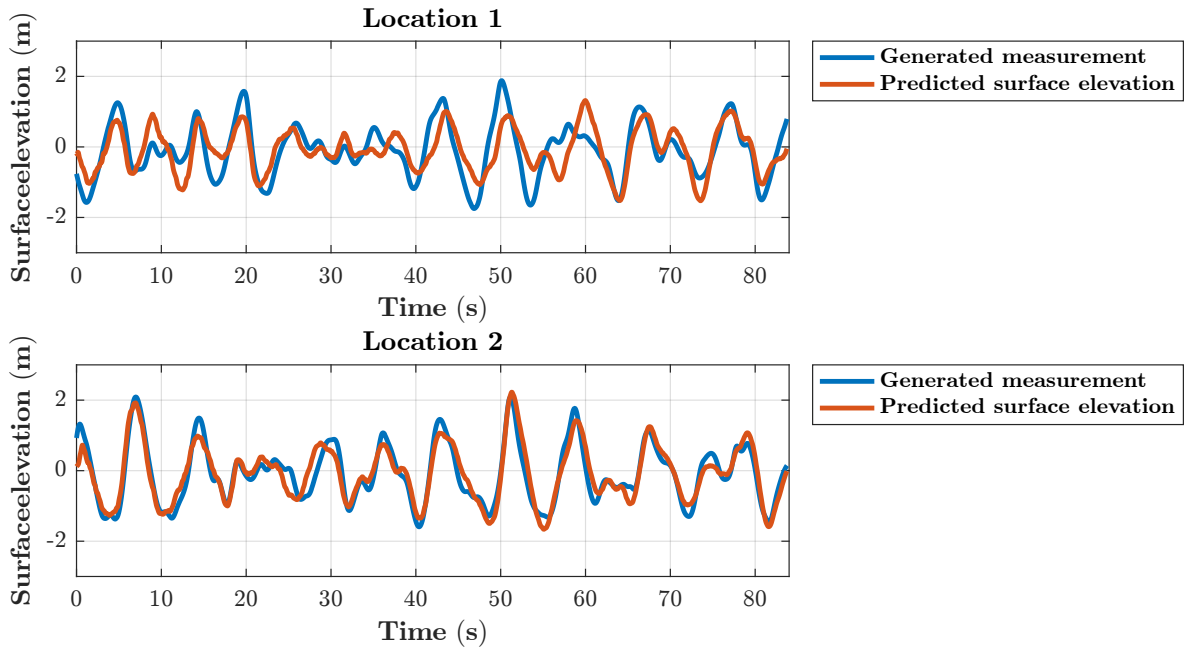
Figure 6.7: Estimated surface elevations and the measured surface elevations at the location of the measurement.

affect the error associated with the sea state estimation. An increase in this matrix reduces the estimation error at the measurement location over time; however, it accrues the errors at the other cells on the grids. A balance needs to be observed and achieved in selecting **Q** for the Kalman filter to perform optimally.

6.5 Discussions

The state estimation method proposed in this chapter is experimental. Given its results, we can consider that this method is not ready for field deployment yet. It requires further intensive works to reach its mains objective, which is to promote the local communication system proposed in the earlier chapters. This section highlights the limitations encountered in the development of this sea state estimation method. The limitations encountered are explained to guide further the investigation in the method. The limitations are:

Deficient understanding of the relationship between the phase speeds c_x and c_y in the x-direction and y-direction in the wave equation: This limitation affected the propagation of the waves across the regional grid. The cosine and the sine of the primary wave direction were used to calculate c_x and c_y from the main phase speed c_p given in Table C.1. With this approach of linking c_x and c_y to c_p, the waves and the measurement data only propagate in one direction when the main direction is 0 or an integer multiple of $\frac{\pi}{2}$ rad.

Poor Observability of the discrete system model: This restriction affected the translation of the measured output of the system to the internal states. The condition number of the
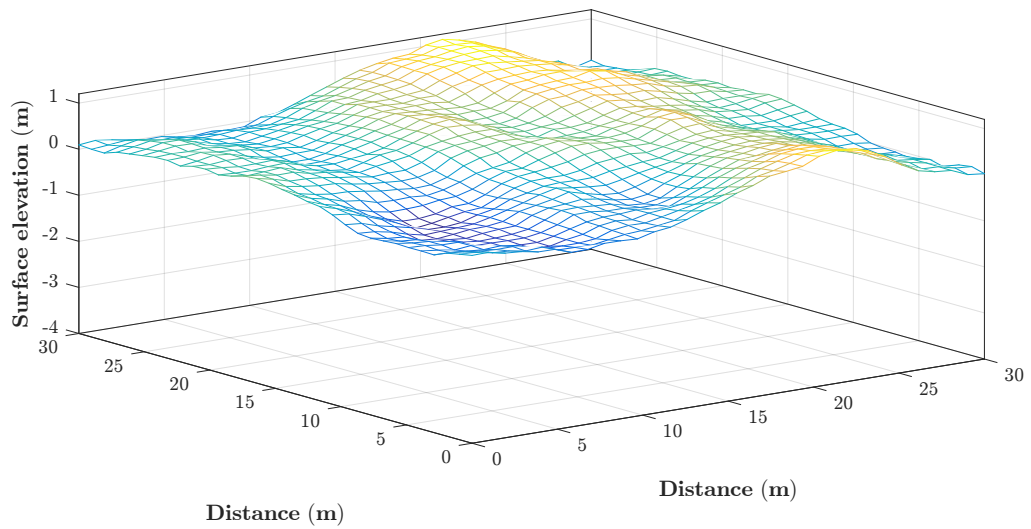
(a) Surface elevation at time = 27.8 seconds
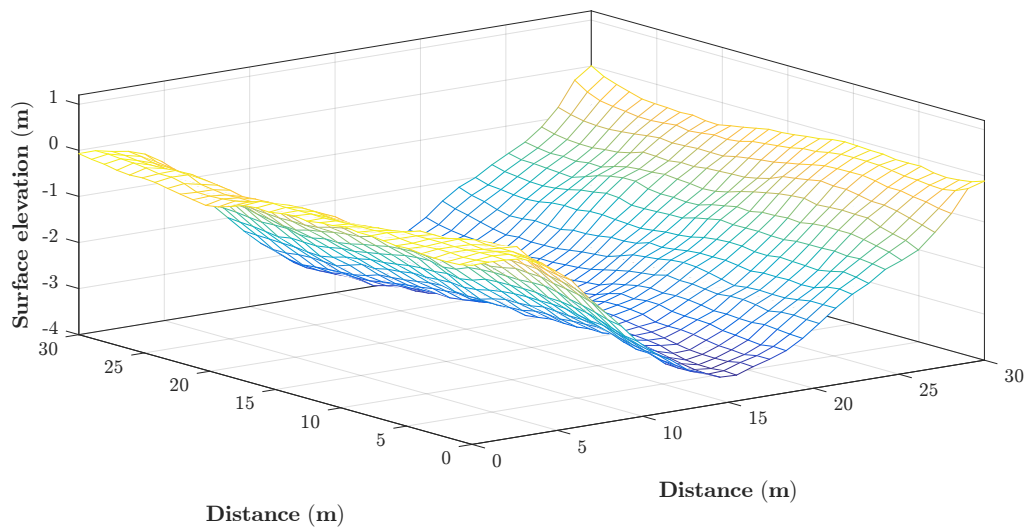
(b) Surface elevation at time = 55.6 seconds
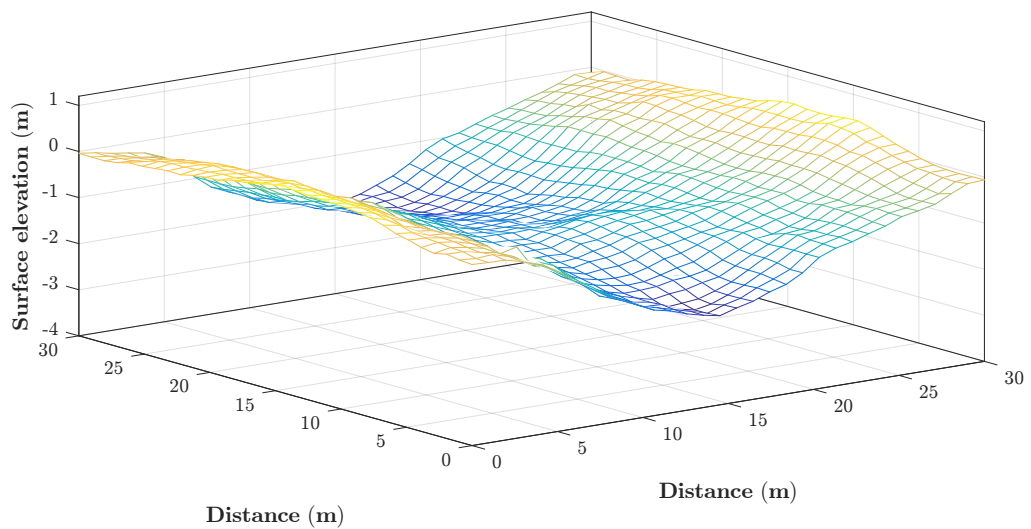
(c) Surface elevation at time = 83.4 seconds

Figure 6.8: Estimated wave field (surface elevation) from the available (generated) measurement data for a wind speed U_{10} equal to 10 m/s.

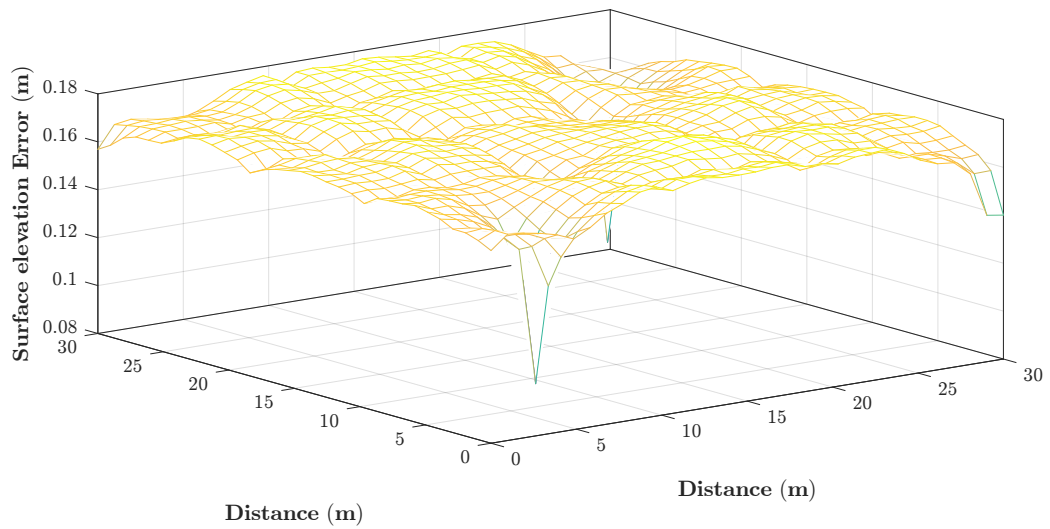(a) Surface elevation error at time = 27.8 seconds

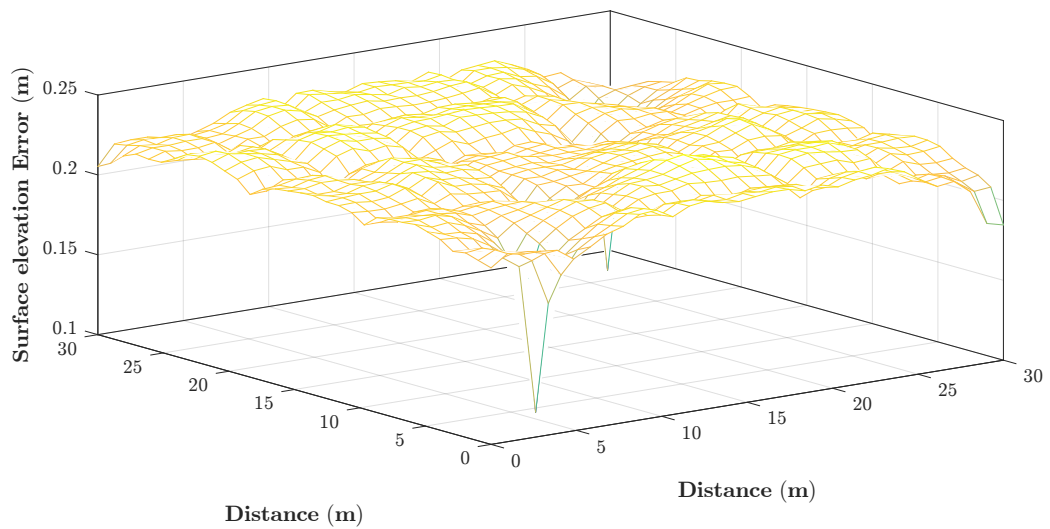(b) Surface elevation error at time = 55.6 seconds

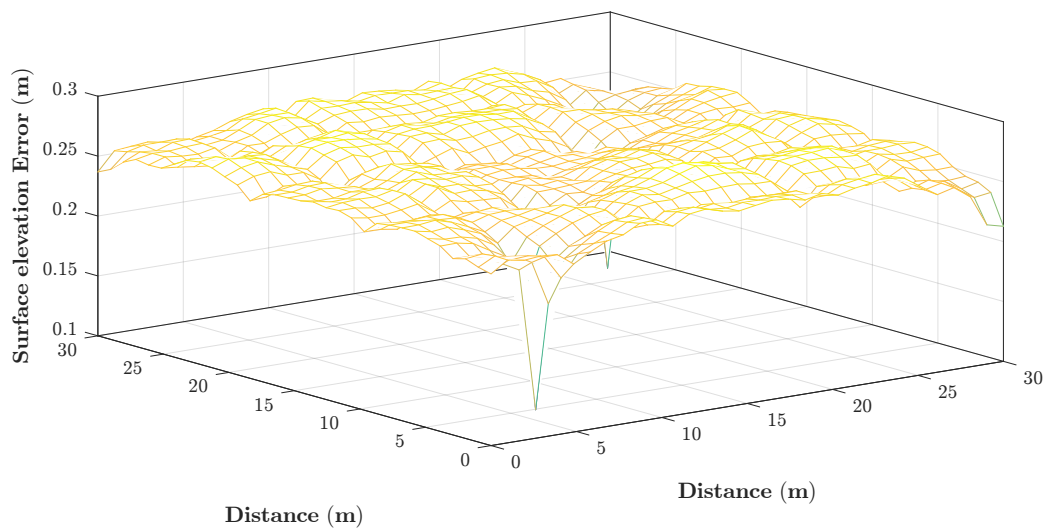

(c) Surface elevation error at time = 83.4 seconds

Figure 6.9: Error of Estimated wave field (surface elevation) from the available (generated) measurement data for a wind speed U_{10} equal to 10 m/s.

system is infinity for the conditions given in Table 6.1.

Resonance of the discrete system model: This one concerned the behaviour of the numerical errors engendered by the filter, and it originated from the lossless characteristics of the wave equation. It means that the system was unable to eliminate the errors and that the errors grow with time.

Lack of experimental practical wave data: This limitation was partly overcome by the use of WAFO to generate the measurement data. WAFO has its limitations.

The inability of WAFO to support spatial step of more than 1 m: This meant that Δx and Δy can only be set to 1 m or less, compelling the length and the width of the area of estimation to the number of cells N_x and N_y. This constraint significantly reduces the effectiveness of WAFO routines for this application because of ocean surface changing slowly in the order of 10 seconds in real life. Nevertheless, Δx and Δy being kept at 1 m or less fixed, in turn, the time step Δt to 55 millimeters per the condition in (6.12).

Insufficient understanding of the air-water interaction during the wave generated by the wind: The air-water interaction dictates the value of the standard deviation of the state noise $\mathbf{w_n}$. Its insufficient understanding due to the inadequacy of resources denoted a trial-and-error type of quantification of the value of the standard deviation of $\mathbf{w_n}$ and ultimately the covariance $\mathbf{Q}$. An appropriate value of $\mathbf{Q}$ should manifest the (wind) energy correctly assimilated from the source function at each cell as a surface elevation.

6.6 Conclusion

In this chapter, an initial approach for estimation of the surface elevation (also known as sea state) was described. The estimation was accomplished through the Kalman Filter algorithm which requires a dynamic system model for the sea state and measurement data. The chapter started with the system model. The system model and its state transition matrix were obtained from the temporal and spatial discretisation of the homogeneous wave equation. This equation was given in (6.5). Then, the initial condition for the three-dimensional surface elevation was developed and generated based on the dimensional power (variance) spectrum. Lastly, the measurement data were generated from the WAFO toolbox. WAFO is a MATLAB based toolbox developed for simulations of wave field and the analysis of fatigues and loads. It was used here in the research due to the lack of real-life measurement data.

Developed in MATLAB, the results from the Kalman Filter routine were encouraging in the sense that the produced wave fields were realistic waves with non-existent discontinuity and with a minimum error at the measurement locations. The method developed in this chapter constituted a starting point to eventually predict or research ahead in real time the

behaviour of the surface waves in the surrounding of the location of a surface marine vehicle and consequently navigate this vehicle for local communication and other applications.

Chapter 7

Conclusion and Recommendations

This chapter summarises the main research questions of the research and its principal findings. After that, the chapter puts forward, for consideration, a few recommendations for future work.

7.1 Conclusions

The research aimed to evaluate the Low Power Wide Area Network (LPWAN) technologies and propose a low power communication system for the local collaboration between two surface marine vehicles. The Wave Glider platform, which is a hybrid, uncrewed surface marine vehicle was considered as a study case in the development of the local communication system. Currently, the Wave Glider platform uses the Iridium satellite communication network to relay data to the shore. This method of communication has proven to be an important factor in the already high cost of operation of the platform. It was established that the mere existence of an alternative low power communication system would minimise the operating cost of the platform considerably and also enable the collaboration between two or more Wave Glider platforms.

The evaluation of the LPWAN technologies revealed that the LoRa technology was the optimal option for the application in the marine environment. The reasons behind the preferences of the LoRa Radio technology are elaborated on, in Chapter 3. Two LoRa systems were therefore designed, implemented and tested both in-land and over the surface of the sea. The systems were designed with a carrier frequency of 868 MHz. The results of the tests demonstrated that the LoRa system was a suitable technology for the applications of local communication on the surface of the ocean. A reliable radio channel was instituted successfully across the ocean over a distance of 5 kilometers.

The investigation on the radio communication near the surface of the ocean water indicated that the seawater might have a notable effect on the radio propagation at the operating frequency of the LoRa systems. This effect was evaluated through simulations and real-life experiments. The FEKO Suite was used for the simulations, and one of the LoRa systems that designed was used in the experiment. These were the focus of Chapter 4. Both the simulations and the experiment's results divulged that the seawater behaves like a lossy conductor and reflects the signal at 868 MHz. These two responses of the seawater resulted in an amplification

of the signal power, thereby improving the received signal levels. It was also found that the total antenna height improved the received power levels.

Another factor to consider in local communication near the surface of the ocean was the presence of the surface waves. These surface waves can act as a blockage severing momentarily the radio link between the transceivers and causing packets to drop. Due to the known statistical properties of the surface waves, this issue was approached from a probability perspective in Chapter 5 where an expression was developed to estimate the probability of the LoS, i.e. the probability that the surface wave will not block the transmission of the packet. The probability was dependent on the wind speed, the total antenna height and finally the distance separating the two nodes in a point-to-point communication system. Simulations showed that the probability is directly proportional to the total antenna height and indirectly proportional to both the wind speed and the distance between the two nodes. Regrettably, the results of the experiment were not conclusive in the context of the probability of the LoS.

The second last part of the research explored an approach to improve the probability of the LoS dynamically. It was observed that by ensuring that the surface marine vehicles transmit after synchronising their times at the peak of the local waves would improve the probability of the LoS remarkably as it would translate to higher antennas. However, the surface marine vehicles lack the awareness of the surrounding wave field. In Chapter 6, the Kalman Filter was proposed as an estimation routine to estimate the surface elevation for a rectangular spatial domain, in general, and around the positions of the vehicle in particular, using the lossless wave equation to model the system. The measurement data were generated from a MATLAB toolbox named WAFO [85, 86]. Computational requirements limited the simulations of the estimation routine. However, the results obtained for a small domain demonstrated the ability of this approach to eventually add value to the local communication by help to improve the probability of the LoS.

7.2 Recommendations for Further Work

From the preceding conclusions, the following recommendations are made for the next steps in the research regarding the local communication system:

- Organised and perform another experiment over the ocean around the time of the day when the unwanted influence of the movement of the boats could be mitigated and collect intelligible data that can be utilised to evaluate the probability of the LoS numerically and compare it with the analytical results obtain about the probability of the LoS.

- Organise an experiment in the open sea to establish the framework for an actual configuration of the local inter-vessel communication.

- Generate (or collect) real sea surface elevation data in a controlled environment and extend the sea state estimation to practical ocean surface waves and a larger spatial domain.

- Design a LoRa communication system constituting a transceiver and antenna with optimised code that could be used on any unmanned surface marine vehicle for local and low power communication near the surface of the ocean.

- Revisit the sea state estimation method and improve on it while considering the limitation of the current approach.

7.3 Final Remarks

This dissertation presented contributions to the collaborative control of Wave Glider platforms. This study represents the starting point of the investigation and applications of Low Power Wide Area Networks technologies in the marine environment for local communication between collaborating small surface vessels.

References

[1] "Wave glider rendering," https://gigaom.com/2011/06/07/ wave-powered-robots-to-monitor-the-oceans/wave-glider-rendering/, (Accessed on 05/14/2017).

[2] "How it works, wave glider unmanned surface vehicle liquid robotics," https://www.liquid-robotics.com/platform/how-it-works/, (Accessed on 05/23/2017).

[3] "Wg_datasheet-1.0_web.pdf," http://www.oceandata.co.kr/GroupWare/Home/ product/brochure/liquid_robotics/WG_DataSheet-1.0_web.pdf, (Accessed on 05/31/2017).

[4] "Wave glider," http://auvac.org/platforms/view/250, (Accessed on 05/31/2017).

[5] R. A. Olson, "Communications architecture of the liquid robotics wave glider," *IFAC Proceedings Volumes*, vol. 45, no. 5, pp. 255–259, 2012.

[6] U. D. Nielsen, R. Galeazzi, and A. H. Brodtkorb, "Evaluation of shipboard wave estimation techniques through model-scale experiments," in *OCEANS 2016-Shanghai*. IEEE, 2016, pp. 1–8.

[7] A. Caiti, V. Calabrò, S. Grammatico, A. Munafò, and M. Stifani, "Lagrangian modeling of the underwater wave glider," in *OCEANS 2011 IEEE - Spain*, June 2011, pp. 1–6.

[8] "Lorawan101.pdf," https: //www.lora-alliance.org/portals/0/documents/whitepapers/LoRaWAN101.pdf, (Accessed on 06/06/2017).

[9] L. Vangelista, A. Zanella, and M. Zorzi, "Long-range iot technologies: The dawn of lora™," in *Future Access Enablers of Ubiquitous and Intelligent Infrastructures*. Springer, 2015, pp. 51–58.

[10] "Sx1276-7-8.book," https://www.semtech.com/uploads/documents/DS_SX1276-7-8-9_W_APP_V5.pdf, (Accessed on 05/22/2018).

[11] "B-l072z-lrwan1 - stm32l0 discovery kit lora, sigfox, low-power wireless - stmicroelectronics," http://www.st.com/en/evaluation-tools/b-l072z-lrwan1.html, (Accessed on 06/10/2018).

[12] "Numerical methods in feko," https://www.altairhyperworks.com/ResourceLibrary.aspx?category=Technical%20Papers&altair_products=FEKO, (Accessed on 08/22/2018).

[13] G. Chen, "Introduction to random signals and applied kalman filtering," *International Journal of Adaptive Control and Signal Processing*, vol. 6, no. 5, pp. 516–518, 1992.

[14] T. Elfouhaily, B. Chapron, K. Katsaros, and D. Vandemark, "A unified directional spectrum for long and short wind-driven waves," *Journal of Geophysical Research: Oceans*, vol. 102, no. C7, pp. 15 781–15 796, 1997.

[15] N. D. Kraus, "Wave glider dynamic modeling, parameter identification and simulation," Ph.D. dissertation, Honolulu:[University of Hawaii at Manoa, May 2012, 2012.

[16] "Insight_breakdown_of_lpwan_technologies.pdf," http://web.luxresearchinc.com/hubfs/Insight_Breakdown_of_LPWAN_Technologies.pdf?t=1461874447328, (Accessed on 06/05/2017).

[17] "A climate window in the southern ocean," https://news.mit.edu/2012/southern-ocean-climate-0228, (Accessed on 08/18/2018).

[18] "The southern ocean in a changing climate," http://acecrc.org.au/project/southern-ocean-in-a-changing-climate/, (Accessed on 08/18/2018).

[19] "Case study: Climate change research in the southern ocean," https://www.info.liquid-robotics.com/csir-climate-case-study, (Accessed on 08/18/2018).

[20] "Environmental assessment liquid robotics," https://www.liquid-robotics.com/markets/environmental-assessment/, (undefined 19/8/2018 23:25).

[21] "The wave glider: How it works," https://www.liquid-robotics.com/wave-glider/how-it-works/, (Accessed on 08/19/2018).

[22] R. Hine, S. Willcox, G. Hine, and T. Richardson, "The wave glider: A wave-powered autonomous marine vehicle," in *OCEANS 2009, MTS/IEEE Biloxi-Marine Technology for Our Future: Global and Local Challenges*. IEEE, 2009, pp. 1–6.

[23] J. Manley and S. Willcox, "The wave glider: A new concept for deploying ocean instrumentation," *IEEE instrumentation & measurement magazine*, vol. 13, no. 6, 2010.

[24] ——, "The wave glider: A persistent platform for ocean science," in *OCEANS 2010 IEEE-Sydney*. IEEE, 2010, pp. 1–5.

[25] P. Ngo, W. Al-Sabban, J. Thomas, W. Anderson, J. Das, and R. N. Smith, "An analysis of regression models for predicting the speed of a wave glider autonomous surface vehicle," in *Proceedings of Australasian Conference on Robotics and Automation. Australian*, 2013, pp. 1–9.

[26] R. N. Smith, J. Das, G. Hine, W. Anderson, and G. S. Sukhatme, "Predicting wave glider speed from environmental measurements," in *OCEANS 2011*. IEEE, 2011, pp. 1–8.

[27] U. D. Nielsen, "A concise account of techniques available for shipboard sea state estimation," *Ocean Engineering*, vol. 129, pp. 352–362, 2017.

[28] R. Pascoal and C. G. Soares, "Kalman filtering of vessel motions for ocean wave directional spectrum estimation," *Ocean Engineering*, vol. 36, no. 6-7, pp. 477–488, 2009.

[29] U. D. Nielsen, M. Bjerregård, R. Galeazzi, and T. I. Fossen, "New concepts for shipboard sea state estimation," in *OCEANS'15 MTS/IEEE Washington*. IEEE, 2015, pp. 1–10.

[30] N. Montazeri, U. D. Nielsen, and J. J. Jensen, "Estimation of wind sea and swell using shipboard measurements–a refined parametric modelling approach," *Applied Ocean Research*, vol. 54, pp. 73–86, 2016.

[31] N. Kraus and B. Bingham, "Estimation of wave glider dynamics for precise positioning," in *OCEANS 2011*. IEEE, 2011, pp. 1–9.

[32] G. Rampersadh, "Sea-state interaction based dynamic model of the liquid robotics' wave glider," Master's thesis, University of Cape Town, 2018.

[33] "datawell_brochure_iridium_sbd_b-40-03.pdf," http://www.datawell.nl/Portals/0/Documents/Brochures/datawell_brochure_iridium_sbd_b-40-03.pdf, (Accessed on 08/20/2018).

[34] "Iridium short burst data service plans," https://satellitephonestore.com/catalog/sale/details/iridium-short-burst-data-service-plans-2780, (Accessed on 08/20/2018).

[35] "Iridium short burst data airtime," http://www.satphonestore.com/tech-browsing/iridium-nav/iridium-sbd/airtime.html, (Accessed on 08/20/2018).

[36] "Plans for iridium short burst data (sbd) - satphoneamerica.com," https://www.satphoneamerica.com/satellite-services/iridium/plans-iridium-short-burst-data-sbd/, (Accessed on 08/20/2018).

[37] "Iridium short burst data (sbd) transceiver," https://www.sutron.com/product/iridium-short-burst-data-sbd-transceiver/, (Accessed on 08/20/2018).

[38] "Lpwan the benefits of lpwan technology vs other iot connectivity options iot for all," https://www.iotforall.com/lpwan-benefits-vs-iot-connectivity-options/, 08 2017, (undefined 22/1/2019 15:18).

[39] "What is lpwan (low-power wide area network)? - definition from whatis.com," http://internetofthingsagenda.techtarget.com/definition/ LPWAN-low-power-wide-area-network, (Accessed on 06/05/2017).

[40] K. Mekki, E. Bajic, F. Chaxel, and F. Meyer, "A comparative study of lpwan technologies for large-scale iot deployment," *ICT express*, vol. 5, no. 1, pp. 1–7, 2019.

[41] "Comparison of lpwan technologies - which is best for me?" https://iot-for-all.com/comparison-of-lpwan-technologies/, (Accessed on 06/05/2017).

[42] R. Sanchez-Iborra, I. G Liaño, C. Simoes, E. Couñago, and A. Skarmeta, "Tracking and monitoring system based on lora technology for lightweight boats," *Electronics*, vol. 8, no. 1, p. 15, 2019.

[43] P. Gotthard and T. Jankech, "Low-cost car park localization using rssi in supervised lora mesh networks," in *2018 15th Workshop on Positioning, Navigation and Communications (WPNC)*. IEEE, 2018, pp. 1–6.

[44] F. Wang, X. Lan, M. Tang, S. Li, G. Hou, X. Wang, Y. Zhou, and H. Liu, "Monitoring system of substation boundary noise based on lora communication technology," in *IOP Conference Series: Earth and Environmental Science*, vol. 199, no. 3. IOP Publishing, 2018, p. 032084.

[45] "What is lora?" https://www.semtech.com/lora/what-is-lora, (Accessed on 08/20/2018).

[46] C. G. Someda, *Electromagnetic waves*, 2nd ed., Boca Raton, FL, 2006.

[47] "Stm32 lora® software expansion for stm32cube," http://www.st.com/content/ccc/resource/technical/document/user_manual/ group0/31/96/2f/3b/df/c1/40/2e/DM00300436/files/DM00300436.pdf/jcr: content/translations/en.DM00300436.pdf, (Accessed on 08/29/2017).

[48] "Microsoft word iridium data services white paper 10 final draftdoc," http://www.stratosglobal.com/~/media/documents/irid/public/ irid_whitepaper_satellitedataservices.pdf, 05 2012, (undefined 22/1/2019 19:51).

[49] "Wisuncomparingiotnetworkspdf," https: //www.wi-sun.org/wp-content/uploads/Wi-SUN-Comparing-IoT-Networks.pdf, (undefined 22/1/2019 20:8).

[50] F. Adelantado, X. Vilajosana, P. Tuset-Peiro, B. Martinez, and J. Melia, "Understanding the limits of lorawan," *arXiv preprint arXiv:1607.08011*, 2016.

[51] Y. Liao, L. Wang, Y. Li, Y. Li, and Q. Jiang, "The intelligent control system and experiments for an unmanned wave glider," *PloS one*, vol. 11, no. 12, p. e0168792, 2016.

[52] "Rf1276-868_datasheet_9cba8bce-c829-4b6a-805c-a3e34622799b.pdf," https://cdn.shopify.com/s/files/1/2219/1447/files/ RF1276-868_Datasheet_9cba8bce-c829-4b6a-805c-a3e34622799b.pdf? 6405426193169986854, (Accessed on 05/27/2018).

[53] "Rf1276868 long distance lora transceiver otto wireless solutions," https://otto-wireless-solutions.myshopify.com/collections/lora-devices/products/ long-distance-lora-transceiver, (undefined 22/1/2019 23:17).

[54] S. Filiposka, I. Mishkovski, and B. T. Trajkoska, "Terrain details effect on connectivity in ad hoc wireless networks," *Communications and Network*, vol. 5, no. 02, p. 30, 2013.

[55] L. Piazzi and H. L. Bertoni, "Effect of terrain on path loss in urban environments for wireless applications," *IEEE Transactions on Antennas and Propagation*, vol. 46, no. 8, pp. 1138–1147, 1998.

[56] "Electromagnetic simulation software altair feko," https://altairhyperworks.com/product/FEKO, 02 2016, (undefined 23/1/2019 11:59).

[57] S. Ramo, J. R. Whinnery, and T. Van Duzer, *Fields and waves in communication electronics*. John Wiley & Sons, 2008.

[58] R. H. Tyler, T. P. Boyer, T. Minami, M. M. Zweng, and J. R. Reagan, "Electrical conductivity of the global ocean," *Earth, Planets and Space*, vol. 69, no. 1, p. 156, 2017.

[59] M. N. Hill, *Physical oceanography*. Harvard University Press, 2005, vol. 1.

[60] "Bl072zlrwan1 stm32l0 discovery kit lora sigfox lowpower wireless stmicroelectronics," https://www.st.com/en/evaluation-tools/b-l072z-lrwan1.html, 02 2017, (undefined 6/7/2018 23:2).

[61] J. Z. Schanker and J. Z. Schanker, *Meteor burst communications*. Artech House Boston, 1990.

[62] L. Milstein, D. Schilling, R. Pickholtz, J. Sellman, S. Davidovici, A. Pavelchek, A. Schneider, and G. Eichmann, "Performance of meteor-burst communication channels," *IEEE Journal on selected areas in communications*, vol. 5, no. 2, pp. 146–154, 1987.

[63] W. J. Pierson Jr and L. Moskowitz, "A proposed spectral form for fully developed wind seas based on the similarity theory of sa kitaigorodskii," *Journal of geophysical research*, vol. 69, no. 24, pp. 5181–5190, 1964.

[64] K. Hasselmann, T. Barnett, E. Bouws, H. Carlson, D. Cartwright, K. Enke, J. Ewing, H. Gienapp, D. Hasselmann, P. Kruseman *et al.*, "Measurements of wind-wave growth and swell decay during the joint north sea wave project (jonswap)," *Ergänzungsheft 8-12*, 1973.

[65] M. S. Ryszard, *Ocean Surface Waves: Their Physics And Prediction*. World Scientific, 1996, vol. 11.

[66] J. Pastor and Y. Liu, "Wave climate resource analysis based on a revised gamma spectrum for wave energy conversion technology," *Sustainability*, vol. 8, no. 12, p. 1321, 2016.

[67] R. H. Stewart, *Introduction to physical oceanography*. Robert H. Stewart, 2008.

[68] L. H. Holthuijsen, *Waves in oceanic and coastal waters*. Cambridge university press, 2010.

[69] M. A. Donelan, J. Hamilton, and W. Hui, "Directional spectra of wind-generated ocean waves," *Phil. Trans. R. Soc. Lond. A*, vol. 315, no. 1534, pp. 509–562, 1985.

[70] M. S. Longuet-Higgins, D. Cartwright, and N. Smith, "Observations of the directional spectrum of sea waves using the motions of a floating buoy," *Ocean wave spectra*, 1963.

[71] W. Cieślikiewicz, "Determination of the surface elevation probability distribution of wind waves using maximum entropy principle," in *Water Wave Kinematics*. Springer, 1990, pp. 345–348.

[72] T. Vinje, "The statistical distribution of wave heights in a random seaway," *Applied Ocean Research*, vol. 11, no. 3, pp. 143–152, 1989.

[73] X. Liu, J. Xu, and H. Tang, "Analysis of frequency-dependent line-of-sight probability in 3d environment," *IEEE Communications Letters*, 2018.

[74] T. Bai, R. Vaze, and R. W. Heath, "Analysis of blockage effects on urban cellular networks," *IEEE Transactions on Wireless Communications*, vol. 13, no. 9, pp. 5070–5083, 2014.

[75] A.-H. Soubra and E. Bastidas-Arteaga, "Functions of random variables," in *ALERT Doctoral School 2014 - Stochastic Analysis and Inverse Modelling*. Michael A. Hicks, Sep. 2014, pp. 43–52. [Online]. Available: http://hal.in2p3.fr/in2p3-01082914

[76] G. Tauchen and R. Hussey, "Quadrature-based methods for obtaining approximate solutions to nonlinear asset pricing models," *Econometrica: Journal of the Econometric Society*, pp. 371–396, 1991.

[77] "1303.0013v1.pdf," http://vixra.org/pdf/1303.0013v1.pdf, (Accessed on 08/17/2018).

[78] A. Stroud and D. Secrest, *Gaussian quadrature formulas*, ser. Prentice-Hall series in automatic computation. Prentice-Hall, 1966. [Online]. Available: https://books.google.co.za/books?id=X7M-AAAAIAAJ

[79] ""foundations of wave phenomena: Complete version" by charles g. torre," https://digitalcommons.usu.edu/foundation_wave/1/, (Accessed on 04/15/2019).

[80] L. Rezzolla, "Numerical methods for the solution of partial differential equations," *Lecture Notes for the COMPSTAR School on Computational Astrophysics*, pp. 8–13, 2011.

[81] T. G. Gwatiringa, "Sea state estimation from inertial platform data for real-time ocean wave prediction," Master's thesis, University of Cape Town, 2018.

[82] R. E. Kalman, "A new approach to linear filtering and prediction problems," *Journal of basic Engineering*, vol. 82, no. 1, pp. 35–45, 1960.

[83] "Wafo. wave analysis for fatigue and oceanography," http://www.maths.lth.se/matstat/wafo/about, (Accessed on 12/04/2018).

[84] S. Aberg and G. Lindgren, "Height distribution of stochastic lagrange ocean waves," *Probabilistic Engineering Mechanics*, vol. 23, no. 4, pp. 359–363, 2008.

[85] "Wafol," http://www.maths.lth.se/matstat/wafo/WafoLagrange_tutorial_2017.pdf, 12 2017, (undefined 13/12/2018 20:18).

[86] "Wafo," http://www.maths.lth.se/matstat/wafo/Wafo_tutorial_2017.pdf, (undefined 13/12/2018 20:20).

[87] "Surfacewavestutorial.pdf," https://www.mathworks.com/matlabcentral/answers/uploaded_files/74101/SurfaceWavesTutorial.pdf, (Accessed on 10/11/2018).

Appendix A

Protocol of the Experiment over the ocean

A.1 Objective

The objective of this experiment is to test the reliability of the LoRa platform in the marine environment over a larger distance, take the measurement that would serve as a practical reference for the probability of the LoS and the effect of the seawater on the power behaviour at the reception of the packets.

A.2 Apparatus

- 2×1 laptops correctly setup with the logging softwares;

- 2×1 STM32 LoRa Discovery Board;

- 2×1 RF1276-868 LoRa module

- 2×1 OA-868-01 Outdoor Antenna;

- 2×1 USB cable.

- 2×1 USB-to-UART cable.

A.3 Procedures

During the experiment, we will vary the antenna height from zero to two meters and log the number of successful transmissions, and the number of packets dropped. We will also log the received power of every packet received.

To start, we need to connect the system. The STM32 LoRa Discovery Board must be connected to the designated USB port on the laptop on one part, and to the antenna on the other part as illustrated below:

Next put the laptop on and start running the python script. The script can be found in the desktop folder named Node 0 or Node 1 depending on which STM32 LoRa Discovery Board in hand, or the folder named LoggerV2 for the RF1276-868 LoRa module at the slave node. The two STM32 LoRa Discovery Boards are numbered 0 and 1 (see the back of the board). The same number apply for the RF1276-868 LoRa modules.
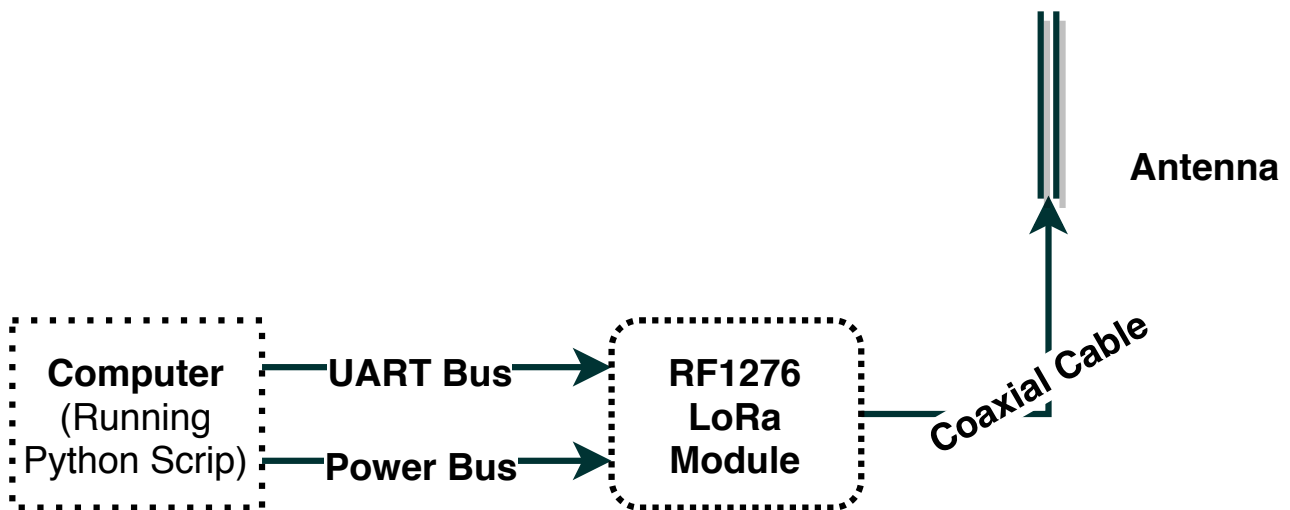
Figure A.1: Illustration of the system Connection. The UART Bus and the Power Bus are combine into the USB cable to connect the laptop and the STM32 LoRa Discovery Boards or the RF1276-868 LoRa modules.

A.3.1 Instructions for the Tests using the STM32 LoRa Discovery Boards

1- Place the antenna at the zero water level;

2- Make sure the python script in the respective folders (Node 0 or Node 1) is running on the laptop;

3- Reset both STM32 LoRa Discovery Boards by pushing the black pushbuttons at both ends;

4- Start transmission at Node 0 by pushing the blue pushbutton;

5- Continue transmission for a predetermined period;

6- Stop transmission at Node 0 by pushing the blue pushbutton;

7- Increase the antenna height by 0.5 meters (or 0.25 meters depending on the behaviour of the waves) at the two locations and start from instruction 2.

A.3.2 Instructions for the Tests using the RF1276-868 LoRa Modules

The steps are different for each node. For the master Node (Node 0), the instructions are:

1- Place the antenna at the zero water level;

2- Wait for the Slave Node to be set up correctly;

3- Power on the power-bank and start transmitting once the other end is ready;

4- Continue transmission for 10 minutes;

5- Stop transmission by powering down the power bank;

6- Increase the antenna height by 0.5 meters (or 0.25 meters depending on the behaviour of the waves) and start from instruction 2.

For node 1, i.e. the slave node where the logging is happening, the instructions are:

1- Place the antenna at the zero water level;

2- Restart running the python script LoggerV2 on the laptop at the Slave node location and confirm that the USB-to-UART cable is connected correctly between the laptop and the LoRa module;

3- Note the time;

4- Signal the Node 0 that you are ready and wait for the start of the transmission. Once started the transmission window will take 10 minutes;

5- Wait for the end of the transmission window;

6- Increase the antenna height by 0.5 meters (or 0.25 meters depending on the behaviour of the waves) and start from instruction 2.

A.3.3 Notes

The LED's can indicate if and when a packet is transmitted or received for the TM32 LoRa Discovery Boards.

Node 0: All LED's flushing indicate reset state (or absence of transmission or reception).
"Only Blue LED ON" indicates packet Transmission.
"Only Red LED ON" indicates Packet reception.

Node 1: All LED's flushing indicate reset state (or Reception window Timeout).
"Only Green LED ON" indicates packet reception.
" Red LED Flush" indicates acknowledgement transmitted.

For the RF1276-868 LoRa modules, the red LED indicates transmission of data while the blue LED indicates the reception of data.

Appendix B

research Codes

All the different codes developed or modified for this dissertation are uploaded to Github. The link to the repository is the following: https://github.com/Kos-c-vi/MSc-research.

The Github repository is organised into Folder with very descriptive and self-explanatory names. The LoRa C researchS folder is divided into two folder for the reception node (Slave) and the transmission node (master). Below are the steps leading to the actual C research folder for the transmission node:

$LoRa\,C\,research -- > TRANSMISSION\_NODE -- > STM32CubeExpansion\_LRWAN\_V1.1.1 -- > researchs -- > Multi -- > Applications -- > LoRa -- > PingPong$

Similar step can be followed for the reception node:

$LoRa\,C\,research -- > RECEPTION\_NODE -- > STM32CubeExpansion\_LRWAN\_V1.1.1 -- > researchs -- > Multi -- > Applications -- > LoRa -- > PingPong$

Appendix C

Sea State Estimation: Power Spectrum and Surface elevations

C.1 Elfouhaily et al's Directional Spectrum

The directional spectrum is in the form of [14]:

$$S(k,\theta) = k^{-4} \left[B_l(k) + B_h(k) \right] D(k,\theta) \tag{C.1}$$

$B_l(k)$ is the long-wave curvature spectrum at low frequencies, $B_h(k)$ is the short-wave curvature spectrum at high frequencies, k in the wave wavenumber and θ is the wave direction relative to the up wind direction. The curvature spectrum is given in the format of $k^{-3}S$. This explained the presence of k^{-3} in (C.1). The two curvature spectra are:

$$\begin{aligned}
B_l(k) &= \tfrac{1}{2}\alpha_p \tfrac{c_p}{c} L_{PM} J_p \exp\left[-\tfrac{\Omega}{\sqrt{10}} \left(\sqrt{\tfrac{k}{k_p}} - 1 \right) \right] \\
B_h(k) &= \tfrac{1}{2}\alpha_m \tfrac{c_m}{c} \exp\left[-\tfrac{1}{4} \left(\sqrt{\tfrac{k}{k_m}} - 1 \right)^2 \right]
\end{aligned} \tag{C.2}$$

$D(k,\theta)$ is the directional spreading function that convert the one-dimensional spectrum into a two-dimensional directional spectrum. $D(k,\theta)$ is given by:

$$D(k,\theta) = \frac{1}{2\pi} \left[1 + \tanh\left(a_0 + a_p \left[\frac{c}{c_p} \right]^{2.5} + a_m \left[\frac{c_m}{c} \right]^{2.5} \right) \cos 2\theta \right] \tag{C.3}$$

The different parameters in equations C.2 and C.3 are tabulated in Table C.1 with their expressions (or values) and descriptions. The wave age is set by the dimensionless parameter Ω which is proportional to the ratio $\frac{U_{10}}{c}$ as indicated bellow [87]:

- $\Omega = 0.84$ corresponded to a fully developed sea;

- $\Omega = 1$ corresponded to a mature sea;

- $\Omega = 2$ to 5 corresponded to a young to a very young sea.

The maximum value of the wave age parameter is set to 5 due to the physical constraints that relate the wave-air interaction [14].

Table C.1: Tabulation of the parameters in equations (C.2) and (C.3) with their expressions and descriptions[14]

Parameters	Expressions	Descriptions
a_0	$\frac{\ln 2}{4} = 0.1733$	Constant parameter
a_p	4	Constant parameter
a_m	$0.13\frac{u^*}{c_m}$	Constant parameter
c_m	$\sqrt{\frac{2g}{k_m}} = 0.23 \ m/s$	The minimum phase speed at the wavenumber k_m
u^*	$0.00144U_{10} \ m/s$	The Friction velocity
c	$\sqrt{\frac{g}{k}(1 + (\frac{k}{k_m})^2)}$	The phase speed the wave
c_p	$\sqrt{\frac{g}{k_p}}$	The phase speed at the spectral peak
k_m	$370.0 \ \text{rad}/m$	The maximum spatial cut-off frequency
k_p	$\frac{g}{U_{10}}\Omega^2$	The spatial frequency (wavenumber) at the maximum of the spectrum
Ω	Variable	The wave age (function of $\frac{U_{10}}{c}$)
α_m	$0.01(1 + \ln \frac{n^*}{c_m})$ if $n^* < c_m$ or $0.01(1 + 3\ln \frac{n^*}{c_m})$ if $n^* > c_m$	Generalised Phillips-Kitaigorodskii equilibrium range parameter for short-waves
α_p	$0.006\Omega^{0.55}$	Generalised Phillips-Kitaigorodskii equilibrium range parameter for long-waves
L_{PM}	$\exp\left[-\frac{5}{4}\left(\frac{k_p}{k}\right)^2\right]$	Pierson–Moskowitz (PM) shape spectrum
J_p	γ^δ	Peak enhancement introduced by the JONSWAP spectrum
σ	$0.08(1 + 4\Omega^{-3})$	-
γ	1.7 if $0.84 < \Omega < 1$ or $1.7 + \log \Omega$ if $1 < \Omega < 5$	-
δ	$\exp\left[-\frac{\left(\frac{k_p}{k}-1\right)^2}{2\sigma^2}\right]$	-

C.2 Surface Elevations

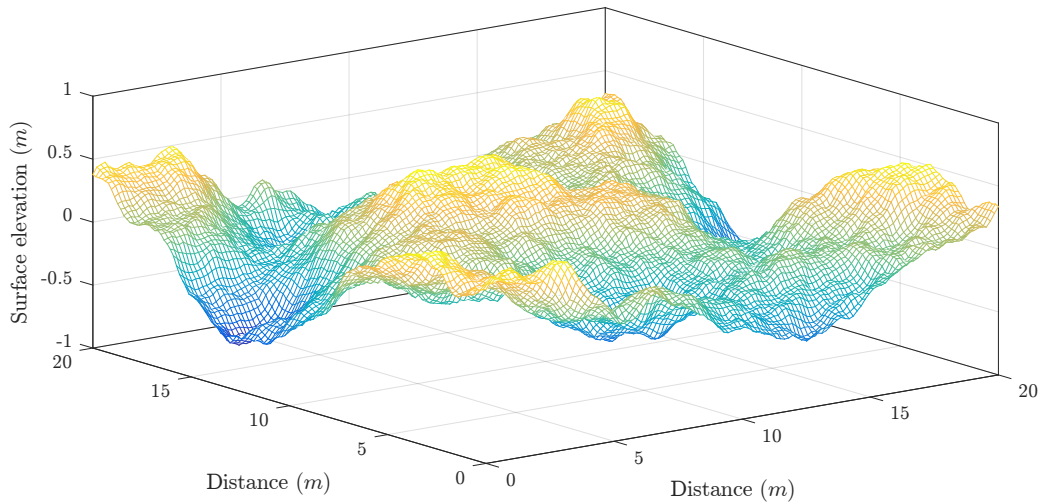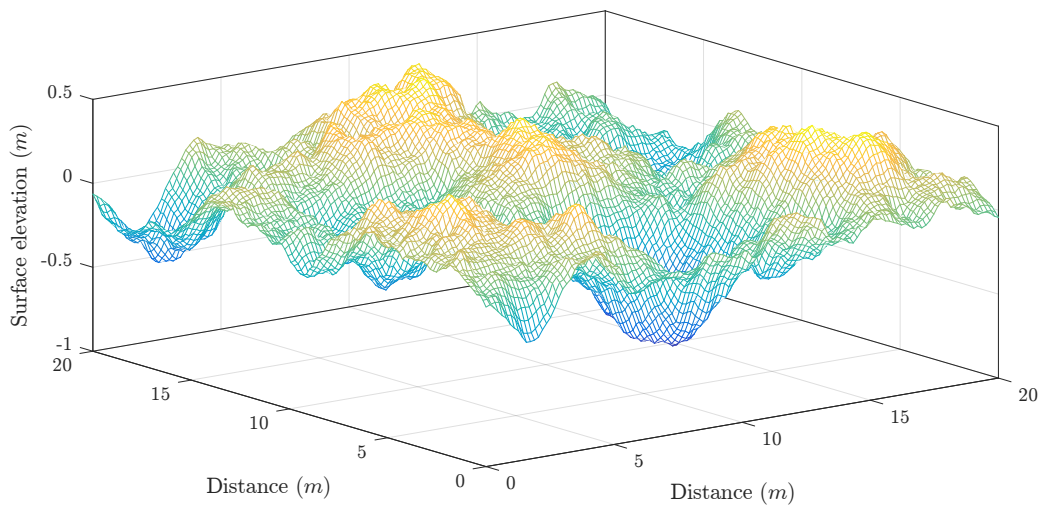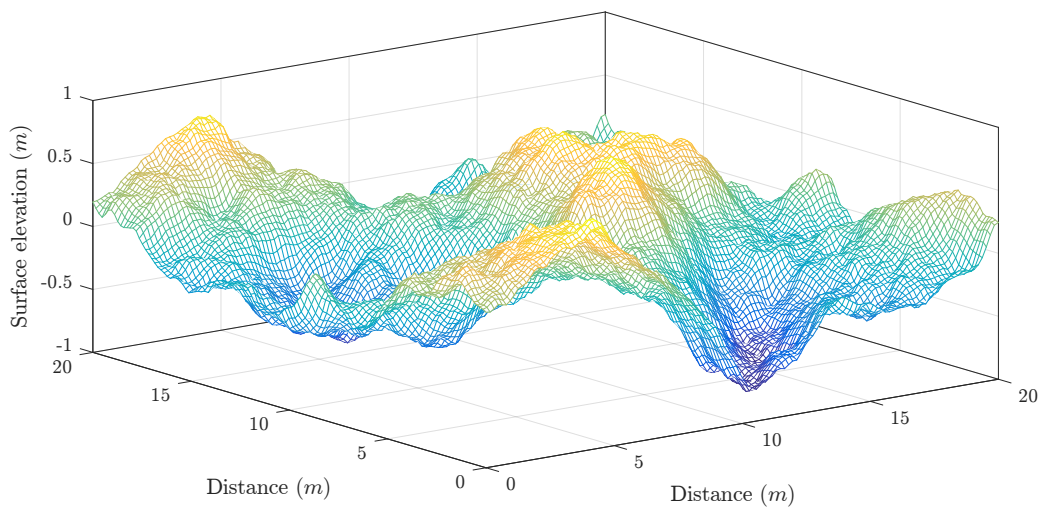Below are the figures of the preliminary results in Chapter 6.

(a) Wind direction $\theta = 0$

(b) Wind direction $\theta = \frac{\pi}{4}$

(c) Wind direction $\theta = \frac{\pi}{2}$

Figure C.1: Generated wave field for a fully developed sea for a wind speed U_{10} to 10 m/s extract the from the directional spectrum proposed in [14]
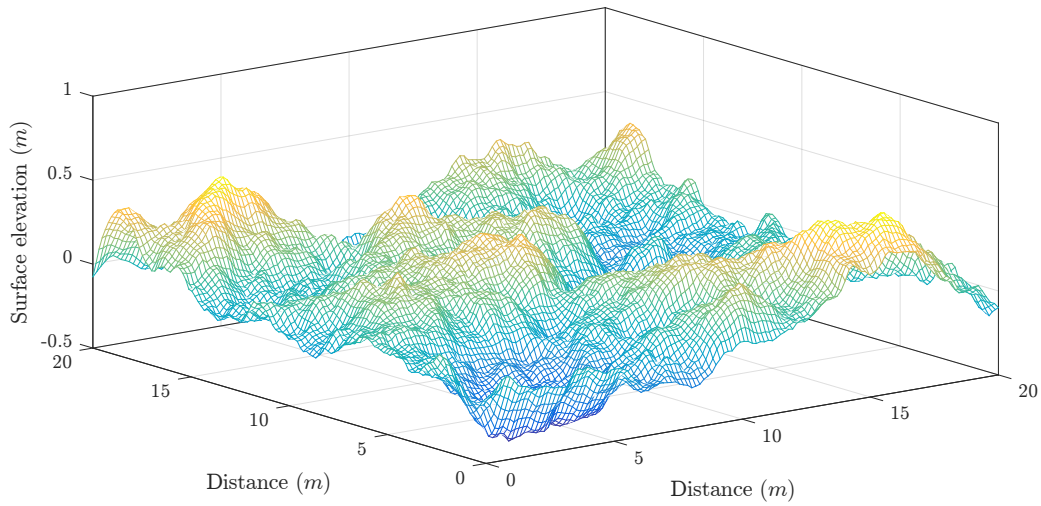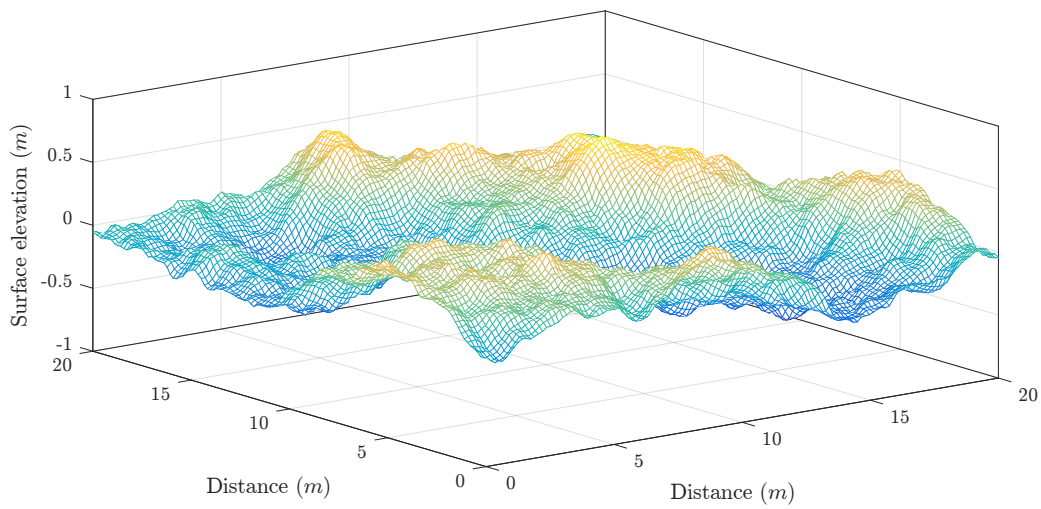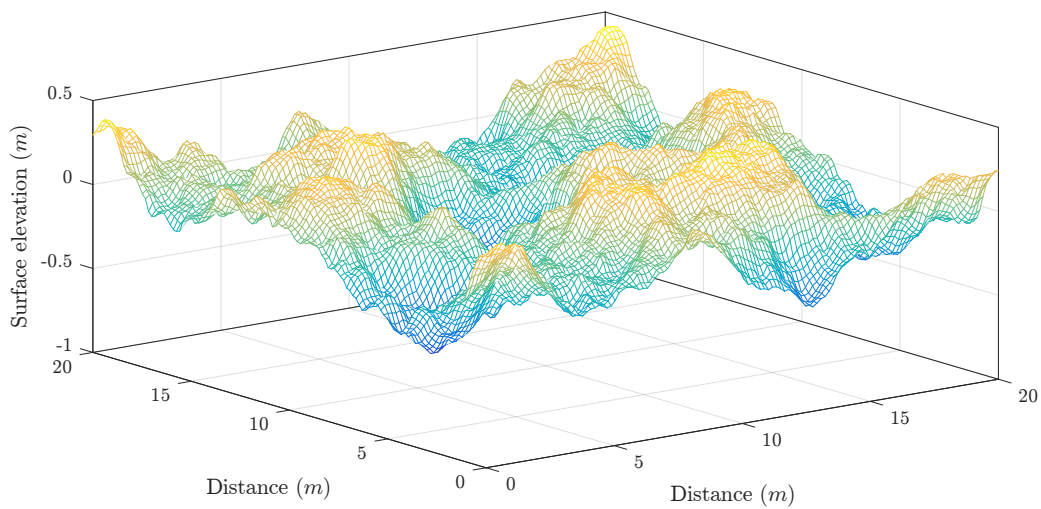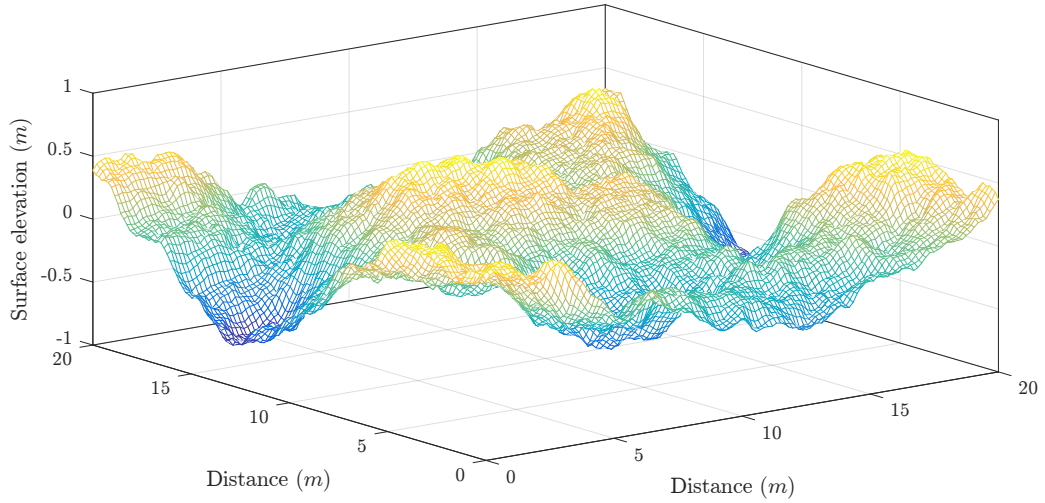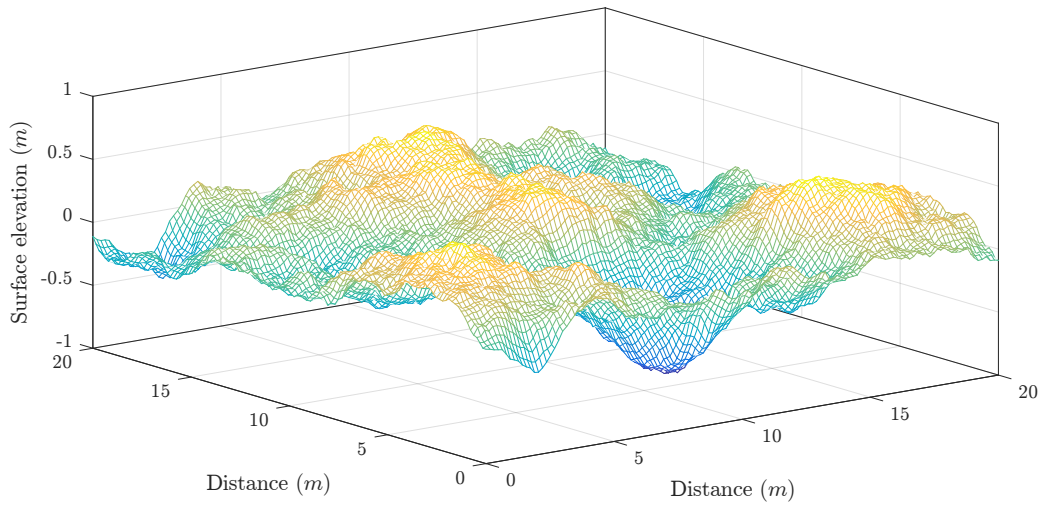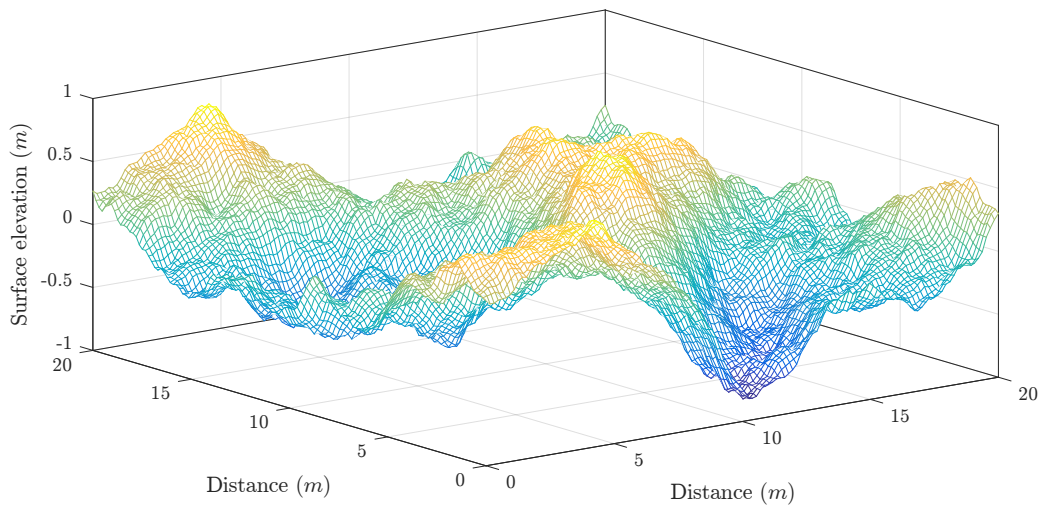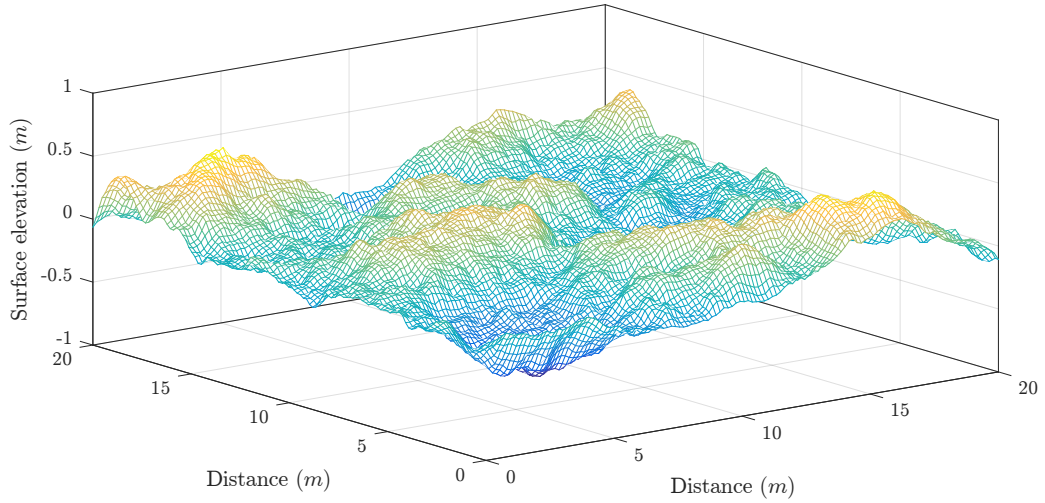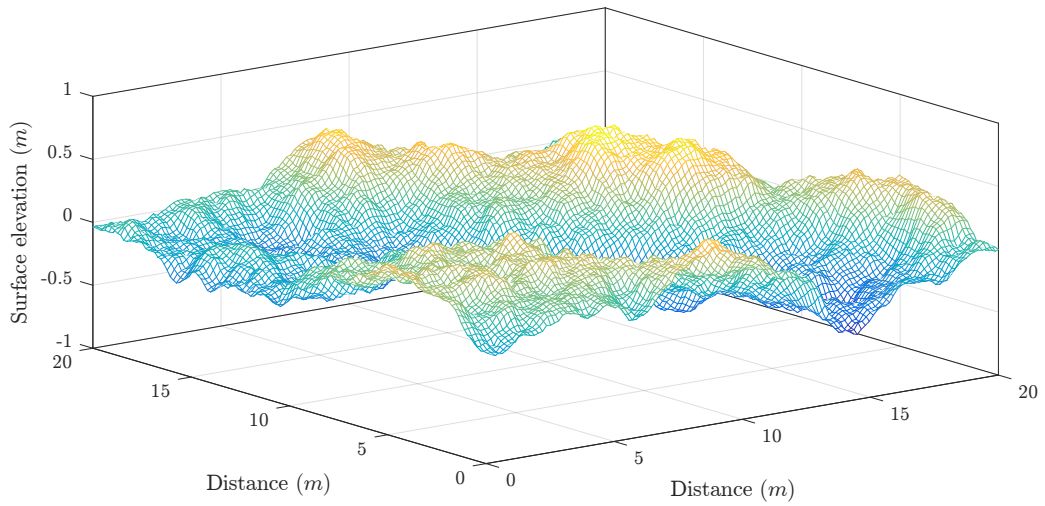
112

(a) Wind direction $\theta = 0$

(b) Wind direction $\theta = \frac{\pi}{4}$

(c) Wind direction $\theta = \frac{\pi}{2}$

Figure C.2: Generated wave field for a fully developed sea for a wind speed U_{10} to 7 m/s extract the from the directional spectrum proposed in [14]

113

(a) Wind direction $\theta = 0$

(b) Wind direction $\theta = \frac{\pi}{4}$

(c) Wind direction $\theta = \frac{\pi}{2}$

Figure C.3: Outcome of the state equation for a wind speed U_{10} to to 10 m/s
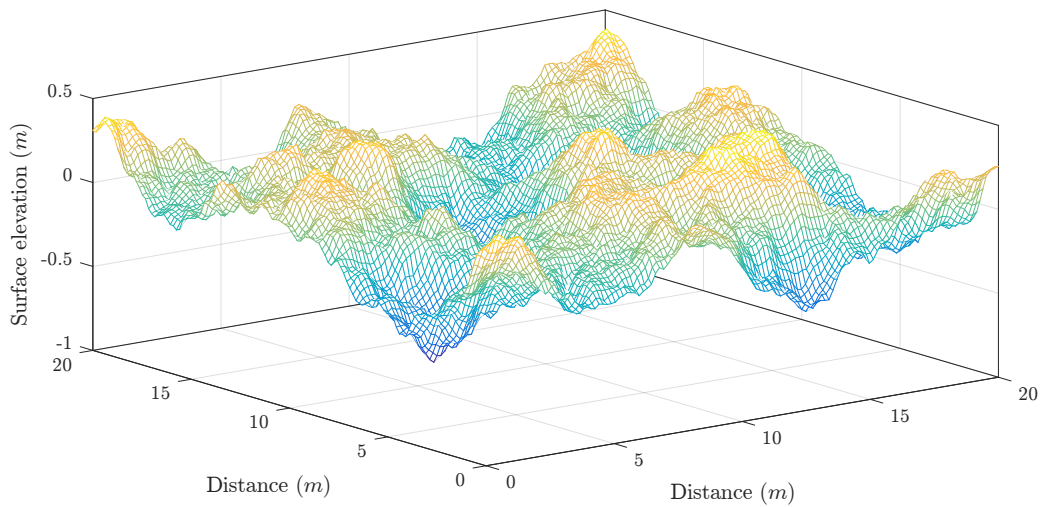
(a) Wind direction $\theta = 0$

(b) Wind direction $\theta = \frac{\pi}{4}$

(c) Wind direction $\theta = \frac{\pi}{2}$

Figure C.4: Outcome of the state equation for a wind speed U_{10} to 7 m/s

Appendix D

Ethic Form

APPLICATION FORM

Please Note:
Any person planning to undertake research in the Faculty of Engineering and the Built Environment (EBE) at the University of Cape Town is required to complete this form **before** collecting or analysing data.The objective of submitting this application *prior* to embarking on research is to ensure that the highest ethical standards in research, conducted under the auspices of the EBE Faculty, are met. Please ensure that you have read, and understood the **EBE Ethics in Research Handbook**(available from the UCT EBE, Research Ethics website) prior to completing this application form: http://www.ebe.uct.ac.za/usr/ebe/research/ethics.pdf

APPLICANT'S DETAILS		
Name of principal researcher, student or external applicant		Kossivi Fangbemi
Department		Electrical Engineering
Preferred email address of applicant:		fngkos001@myuct.ac.za
If a Student	Your Degree: e.g., MSc, PhD, etc.,	MSc
	Name of Supervisor (if supervised):	Prof E. Boje
If this is a researchcontract, indicate the source of funding/sponsorship		Prof E. Boje
Project Title		**Collaborative Control of Wave Glider Platforms**

I hereby undertake to carry out my research in such a way that:
- there is no apparent legal objection to the nature or the method of research; and
- the research will not compromise staff or students or the other responsibilities of the University;
- the stated objective will be achieved, and the findings will have a high degree of validity;
- limitations and alternative interpretations will be considered;
- the findings could be subject to peer review and publicly available; and
- I will comply with the conventions of copyright and avoid any practice that would constitute plagiarism.

SIGNED BY	Full name	Signature	Date
Principal Researcher/ Student/External applicant	Kossivi Fangbemi		**10 May 2017**

APPLICATION APPROVED BY	Full name	Signature	Date
Supervisor (where applicable)	Prof Edward Boje	signature removed	**10 May 2017**
HOD (or delegated nominee) Final authority for all applicants who have answered NO to all questions in Section1; and for all Undergraduateresearch (Including Honours).		Signature Removed	**10 May 2017**
Chair : Faculty EIR Committee For applicants other than undergraduate students who have answered YES to any of the above questions.		Signature Removed	**10 May 2017**

Page 1 of 1